

GRANULAR FLOW AND HEAT TRANSFER IN A
SCREW CONVEYOR HEATER: A DISCRETE
ELEMENT MODELING STUDY



HAFIIZ OSMAN

B.ENG. (HONS., NUS)

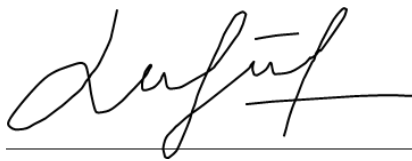
A THESIS SUBMITTED
FOR THE DEGREE OF MASTER OF ENGINEERING
DEPARTMENT OF MECHANICAL ENGINEERING
NATIONAL UNIVERSITY OF SINGAPORE

2012

DECLARATION

I hereby declare that the thesis is my original work and it has been written by me in its entirety. I have duly acknowledged all the sources of information which have been used in this thesis.

This thesis has also not been submitted for any degree in any university previously.

A handwritten signature in black ink, appearing to read 'Hafiiz Osman', is written over a horizontal line.

Hafiiz Osman

25 October 2012

Acknowledgement

First and foremost, I would like to express my sincere gratitude and appreciation to my supervisor, Prof. Arun S. Mujumdar, for his supervision and feedback pertaining to this research. His invaluable assistance of constructive comments and suggestions throughout this research has contributed to the successful completion of this work. Indeed, it is an honour to be a student of a multi-talented personality who is not only a great scientist and engineer, but also an artist and a friend. I would also like to express my profound gratitude to my colleague and mentor, Dr Sachin V. Jangam, for his active participation, lively discussions, patient guidance, and valuable feedback during the course of this research. Special thanks to the members of Transport Processes Research group, both past and present, who have contributed to the vast library of knowledge, and making it available freely via Prof. Mujumdar's personal website and his global network of scientists. Not forgetting staff from Minerals, Metals, and Materials (M3TC) who have rendered their assistance knowingly or unknowingly.

Last but not least, my deepest gratitude to my beloved parents, Osman and Norliah, for their everlasting love and motivation; my wonderful wife Juliana, whose understanding and support is unmatched; and finally my son Fawzan, whose arrival renders the pursuance of this higher degree much more meaningful. Above everything else, all praises be to The Almighty for the strength and blessings, without which all of this will not be possible.

Contents

Acknowledgement	ii
Abstract	vi
List of Tables	vii
List of Figures	viii
Abbreviations	xi
List of Symbols	xii
1 Introduction	1
1.1 Motivation for current work	1
1.1.1 Need for cost effective and energy efficient technique for drying LRC	1
1.1.2 Advances in discrete element modeling of particulate processes .	4
1.2 Assessment of related work	7
1.2.1 Application of DEM in the study of granular flow	7
1.2.2 Application of DEM in the study of granular heat transfer	10
1.2.3 Study of granular flow and heat transfer in screw conveyors	14
1.3 Objectives	23
1.4 Outline of thesis	23
2 Theoretical Background	25
2.1 Molecular dynamics and DEM theory	25
2.1.1 Equations of motion	26
2.1.2 Hertz-Mindlin contact model	27
2.2 Heat transfer in granular beds	32
2.2.1 Wall-to-surface heat transfer	33
2.2.2 Heat penetration in granular beds	34
2.2.3 Overall heat transfer coefficient	37
2.3 DEM framework	38
2.3.1 Contact detection algorithm	39
2.3.2 Particle motion	41
2.3.3 Temperature update	42

2.3.4	Simulation time-step	43
3	Calibration and Modeling	45
3.1	Calibration as a necessary step in DEM	45
3.2	Material selection	46
3.3	Calibration of bulk flow	48
3.4	Calibration of heat transfer coefficients	49
3.4.1	Application of the penetration model	49
3.4.2	Wall-to-particle heat transfer	50
3.4.3	Particle-particle heat transfer	54
3.5	Modeling of screw conveyor heater	58
3.5.1	Model parameters and numerics	58
3.5.2	Granular flow and heat transfer simulation	61
3.5.3	Parametric study	61
3.6	Data analysis	65
3.6.1	Volume and surface area of screw conveyor domain	65
3.6.2	Degree of fullness	66
3.6.3	Determination of residence time distribution (RTD)	67
3.6.4	Heat transfer coefficient	68
4	Granular Flow Characteristics	70
4.1	Introduction	70
4.2	Hold-up	70
4.3	Degree of fullness as a validation parameter	74
4.4	Residence time	77
4.5	Hold-back and segregation	89
5	Heat Transfer Characteristics	93
5.1	Introduction	93
5.2	Evolution of T_{bed} and τ	94
5.3	Temperature distribution in a screw conveyor heater	99
5.3.1	Effect of solid flow rate	94
5.3.2	Effect of screw speed	100
5.3.3	Effect of inclination angle	101

5.3.4	Effect of pitch-to-diameter ratio	102
5.4	Discharge temperature	104
5.5	Calculation of overall heat transfer coefficient	107
5.5.1	Effective heat transfer area	107
5.5.2	Overall heat transfer area	110
6	Summary and Conclusions	113
	Bibliography	115
	Appendix A	125
	Appendix B	127

Abstract

The current work is driven by the need to dry low-rank coals (LRC) in a cost-effective, safe and energy efficient process. Although a number of technologies exist to dry LRC satisfactorily, none can yet claim the capability to continuously process a large amount of coal safely and economically. The screw conveyor heater/dryer is a promising technology that can potentially achieve the said requirements. Currently there is no published work reported on simultaneous modeling of flow and heat transfer of granular beds in a screw conveyor configuration using Discrete Element Method (DEM). As a pioneering work in this subject area, the thesis uses DEM to investigate the influence of operating and geometrical parameters on the hydrodynamic and thermal performance of a screw conveyor heater. The execution of ‘virtual experiments’ via DEM enable system-scale predictions using particle-scale simulation data, while reducing prototyping and testing costs associated with the development of the heater. For the basic screw study, parameters studied include: screw speed (7-19 rpm), mass flow rate (15-300 kg h⁻¹), angle of inclination (0-15 °), and screw pitch-to-diameter ratio (0.25-1.0). This work aims to provide useful insights for future improvements to the designs of screw conveyor heat exchangers.

List of Tables

1.1	Academic and commercial DEM codes.	5
1.2	Experimental studies of granular bed heat transfer.	6
1.3	Flow and heat transfer studies of particulate systems using DEM.	13
1.4	Study of granular flow and heat transfer in screw conveyors.	18
3.1	Differences between particles in practical systems and simulated systems.	46
3.2	Properties of granular bed material.	47
3.3	Calibrated properties for glass bed and copper wall.	49
3.4	Parameters for heat transfer calibration.	50
3.5	Parameters for calculation of h_{ws} using Schlunder's correlation.	51
3.6	Parameters for screw conveyor heater.	60
3.7	Case specifications for parametric study of screw conveyor heater.	62
4.1	Summary of granular flow characteristics for various cases.	91
5.1	Summary of T_{bed} and τ for various cases.	97
5.2	Summary of heat transfer characteristics for various cases.	111

List of Figures

2.1	Motion of discrete particle.	26
2.2	Contact between two discrete particles.	28
2.3	Series heat transfer resistances between wall and bulk.	33
2.4	DEM numerical flow at every time-step.	39
2.5	Contact detection using bins (active cells are highlighted).	40
3.1	Conical pile obtained from (a) experiment, and (b) DEM.	48
3.2	h_{ws} vs. d for packed bed of glass spheres at atmospheric pressure and vacuum.	52
3.3	Evolution of bed temperature for contact-controlled regime where $h_{pp} = 10^5 \text{ W m}^{-2} \text{ K}^{-1}$, and h_{wp} are varied: (a) 100, (b) 200, and (c) $1000 \text{ W m}^{-2} \text{ K}^{-1}$	53
3.4	Heating curve for packed bed heating in contact-controlled regime.	53
3.5	Correlation between h_{ws} (PM) and h_{wp} (DEM).	54
3.6	Evolution of bed temperature for penetration-controlled regime where $h_{wp} = 10^5 \text{ W m}^{-2} \text{ K}^{-1}$, and h_{pp} are varied: (a) 10, (b) 50, and (c) $100 \text{ W m}^{-2} \text{ K}^{-1}$	55
3.7	Evolution of h for packed bed heating in penetration-controlled regime.	56
3.8	Correlation between h_{pp} (DEM) and k_b (PM).	56
3.9	Validation of calibration exercise.	57
3.10	Screw conveyor dryer system.	58
3.11	Computational domain of DEM simulations.	59
3.12	Screw configurations for pitch-to-diameter ratio study: $P/D =$ (a) 1.00, (b) 0.75, (c) 0.50, and (d) 0.25.	64
3.13	Theoretical relationships between screw conveyor parameters: (a) degree of fullness vs. screw speed for different solid flow rates; (b) solid flow rate vs. screw speed for different pitch-to-diameter ratios.	64
4.1	Binning the screw conveyor domain for flow analysis.	71
4.2	Mass of solids in each section of the screw conveyor domain for base case ($M_G = 150 \text{ kg h}^{-1}$, $N = 11 \text{ rpm}$, $P/D = 1.0$).	72

4.3	Average mass of solids in one section of the screw conveyor domain for various cases: (a) solid flow rates ($N = 11$ rpm, $P/D = 1.0$), (b) screw speed ($M_G = 150$ kg h ⁻¹ , $P/D = 1.0$), (c) angle of inclination ($M_G = 150$ kg h ⁻¹ , $N = 11$ rpm), and (d) pitch-to-diameter ratio ($M_G = 150$ kg h ⁻¹ , $N = 11$ rpm).	73
4.4	Theoretical vs. DEM prediction of β for different (a) M_G and (b) N . ($\theta = 0^\circ$, $P/D = 1.0$).	75
4.5	Degree of fullness β with respect to (a) θ and (b) P/D	75
4.6	Particle build-up: (a) $M_G = 90$ kg h ⁻¹ , $N = 30$ rpm; (b) $M_G = 120$ kg h ⁻¹ , $N = 40$ rpm; (c) $M_G = 150$ kg h ⁻¹ , $N = 50$ rpm; ($\beta = 0.3$, $P/D = 0.25$).	76
4.7	Residence time distributions for various M_G . ($M_G = 75$ and 175 kg h ⁻¹ are omitted due to space constraint).	81
4.8	Distribution of particle residence times for various M_G . Views from left to right: side view, longitudinal slice view, third quadrant cross-section view.	82
4.9	Residence time distributions for various N	83
4.10	Distribution of particle residence times for various N . Views from left to right: side view, longitudinal slice view, third quadrant cross-section view.	84
4.11	Residence time distributions curves for various θ	85
4.12	Distribution of particle residence times for various θ : (a) 0, (b) 5, (c) 10, and (d) 15 degrees.	86
4.13	Residence time distributions curves for various P/D	87
4.14	Distribution of particle residence times for various P/D . Views from left to right: side view, longitudinal slice view, third quadrant cross-section view.	88
4.15	Holdback and segregation of particles in a screw conveyor heat exchanger for various cases.	90
4.16	Visualization of axial mixing of particle bed in screw conveyor heat exchanger (Base case: $M_G = 150$ kg h ⁻¹ , $N = 11$ rpm, $P/D = 1.0$).	92
5.1	Binning the screw conveyor domain for heat transfer analysis.	94
5.2	T_{bed} along the length of screw conveyor heater for various M_G ($N = 11$ rpm, $\theta = 0^\circ$, $P/D = 1$).	95

5.3	τ along the length of screw conveyor heater for various M_G ($N = 11$ rpm, $\theta = 0^\circ$, $P/D = 1$).....	96
5.4	T_{bed} vs τ for various cases.....	98
5.5	Distribution of particle temperature for various M_G . Views from left to right: side view, longitudinal slice view, third quadrant cross-section view.....	99
5.6	Distribution of particle temperature for various N . Views from left to right: side view, longitudinal slice view, third quadrant cross-section view.....	100
5.7	Distribution of particle temperature for various θ . Views from left to right: side view, longitudinal slice view, third quadrant cross-section view.....	102
5.8	. Distribution of particle temperature for various P/D . Views from left to right: side view, longitudinal slice view, third quadrant cross-section view.....	103
5.9	Discharge temperature distribution for various cases: (a) solid flow rates ($N = 11$ rpm, $P/D = 1.0$), (b) screw speed ($M_G = 150 \text{ kg h}^{-1}$, $P/D = 1.0$), (c) angle of inclination ($M_G = 150 \text{ kg h}^{-1}$, $N = 11$ rpm), and (d) pitch-to-diameter ratio ($M_G = 150 \text{ kg h}^{-1}$, $N = 11$ rpm).....	104
5.10	Discharge temperature distribution mapping to cool core (CC) particles and heated surface (HS) particles.....	105
5.11	Temperature averages for various cases: (a) solid flow rates ($N = 11$ rpm, $P/D = 1.0$), (b) screw speed ($M_G = 150 \text{ kg h}^{-1}$, $P/D = 1.0$), (c) angle of inclination ($M_G = 150 \text{ kg h}^{-1}$, $N = 11$ rpm), and (d) pitch-to-diameter ratio ($M_G = 150 \text{ kg h}^{-1}$, $N = 11$ rpm). Legend: \square discharge average ($T_{\text{b,f}}$), \bullet heated surface average (T_{HS}), \blacklozenge cool core average (T_{CC}).....	106
5.12	Total effective heat transfer area for various cases: (a) solid flow rates ($N = 11$ rpm, $P/D = 1.0$), (b) screw speed ($M_G = 150 \text{ kg h}^{-1}$, $P/D = 1.0$), (c) angle of inclination ($M_G = 150 \text{ kg h}^{-1}$, $N = 11$ rpm), and (d) pitch-to-diameter ratio ($M_G = 150 \text{ kg h}^{-1}$, $N = 11$ rpm).....	108
5.13	Effective heat transfer area of screw and trough for different pitch-to-diameter ratios ($M_G = 150 \text{ kg h}^{-1}$, $N = 11$ rpm).....	109
5.14	Overall heat transfer coefficient h for various cases.....	110

Abbreviations

CAD	Computer-aided design
CC	Cool core region of granular bed
CFD	Computational Fluid Dynamics
DEM	Discrete Element Method
FEM	Finite Element Method
HS	Heated surfaces region of granular bed
LMTD	Log Mean Temperature Difference
RTD	Residence Time Distribution
SCD	Screw conveyor dryer
MRT	Mean residence time

List of Symbols

a	Diameter of contact area	m
A	Area	m^2
c	Specific heat capacity	$J\ kg^{-1}\ K^{-1}$
C	Concentration of tracer particles	$kg\ kg^{-1}$
C_R	Coefficient of restitution	-
d	Particle diameter	m
D	Geometry diameter	
E	Young's Modulus	Pa
$E(t)$	Exit age distribution function	s^{-1}
F	Force	N
F_d	Damping force vector	N
F_n	Normal force vector	N
F_t	Tangential force vector	N
G	Shear Modulus	Pa
H	Hold-back	-
h	Heat transfer coefficient	$W\ m^{-2}\ K^{-1}$
I	Mass moment of inertia of a body	$kg\ m^2$
k	Thermal conductivity	$W\ m^{-1}\ K^{-1}$
l	Modified mean free path of gas molecules	m
L	Length	m
m	Mass	kg
\mathcal{M}	Molar mass of gas	$kg\ mol^{-1}$
M_G	Solid flow rate	$kg\ h^{-1}$
M_H	Solid hold-up in screw conveyor	kg
n_t	Number of complete turns in a screw conveyor segment	-
n_p	Number of particles	-
N	Screw speed	$kg\ mol^{-1}$
p	Pressure	Pa
P	Screw pitch	m

\mathbf{r}	Position vector	-
R	Radius	m
R_G	Gas constant	$\text{J K}^{-1} \text{mol}^{-1}$
S	Segregation	-
t	Simulation time (or time)	s
T	Temperature	K
\mathbf{T}	Torque	N m
\mathbf{v}	Velocity vector	m s^{-1}
v_L	Linear screw speed	m s^{-1}
V	Volume	m^3
\mathbf{x}	Displacement vector	m

Greek Letters

α	Particle surface roughness	m
β	Degree of fullness	-
δ	Particle overlap	m
δ_r	Screw blade minimum radial clearance	m
δ_t	Flight/plate thickness	m
ϵ	Emissivity	-
θ	Angle of inclination	
μ	Mean	
μ_g	Gas viscosity	Pa s
μ_r	Coefficient of rolling friction	-
μ_s	Coefficient of static friction	-
ν	Poisson's ratio	-
ρ	Density	kg m ⁻³
σ	Stefan-Boltzmann constant	W m ⁻² K ⁻⁴
σ_R	Residence time standard deviation	S
τ	Residence time	s
τ_D	Minimum residence time (or dead time)	s
τ_L	Linear residence time	s
ϕ_A	Accommodation coefficient	-
ϕ_F	Volume fraction of particles	-
ϕ_w	Wall coverage factor	-
ψ	Void fraction	-
ω	Angular velocity	rad s ⁻¹
$\dot{\omega}$	Angular acceleration	rad s ⁻²

Subscripts

bed	Granular bed
cr	Critical
dir	Direct solid-solid
eff	Effective
f	Final
g	Gas
ht	Heat transfer
i	Initial
p	Particle
rad	Radiation
ref	Reference
rel	Relative
s	Bed surface adjacent to wall (first particle layer)
sb	First particle layer to bulk
w	Wall
ws	Wall to first particle layer

Chapter 1

Introduction

1.1 Motivation for current work

The current work is mainly driven by the need to dry low-rank coals (LRC) in the most cost-effective and energy efficient method possible. Although a number of technologies already exist to dry LRC satisfactorily, none can yet claim the capability to continuously process a large amount of coal safely and economically. There is however, a promising new technology that can potentially achieve the said requirements, and that will be the focus of this thesis. This work aims to initiate the much needed experimental and numerical analysis pertaining to the technology of interest. Eventually, this work and its follow-up will provide useful insights for future designs of screw conveyor dryers (SCD).

1.1.1 Need for a cost-effective and energy efficient technique for drying LRC

Despite being geographically dispersed and accounting for more than 50% of the world coal reserve, LRC find limited use due to a number of factors. Firstly, LRC have very low heating value due to its high moisture content which renders low energy output and low power generation efficiency (Li, 2004). Evaporation of coal water during the combustion of LRC reduces the net energy output and efficiency of a plant, and increases

stack gas flow which adds to operating cost. This is in contrast to higher grade coals such as sub-bituminous, bituminous, and anthracites which have found significant use in electricity generation, steel production, and cement manufacturing industries. There are also a number of challenges in the handling of LRC. For instance, it is generally more expensive to transport LRC compared to bituminous coal on a per calorie basis due to the significant amount of moisture (Jangam *et al.*, 2011). This can be mitigated by removing some of the coal water prior to shipping. It was reported that moisture reduction from 35% to 25% reduces logistical costs by up to \$7 million per year for a 600 MW plant (Lucarelli, 2008). There is however a tendency for moisture to be reabsorbed in the course of shipment (Karthikeyan, 2008). Thus any efforts have to be carefully studied from both micro and macro perspectives, taking into account as many factors as possible. The propensity of LRC fines for self-ignition also present another logistical challenge, compounding the difficulty in handling and storage of the resource.

On the other hand, LRC is not without its merits. In some aspects, LRC has an advantage over black coal. Advantages include relatively low mining cost due to its presence in thick seams with less overburden than higher rank coals, high percentage of volatile matter, high reactivity, and very low sulfur content (Willson *et al.*, 1997). Another advantage is the relative abundance of LRC, which until recent times, has been largely ignored due to its prohibitive moisture content which ranges from around 25% for subbituminous coal to around 60% for lignite (Merritt, 1987; Saluja, 1987). Only recently has there been a sudden surge of interest in LRC as an alternative fuel (Reuters

and Bloomberg, 2010) which is mainly triggered by and rising of fuel costs and increasing worldwide demand for energy.

There is much reported work on upgrading of LRC by both academia and industry with thermal drying being the dominating theme in the effort (Jangam *et al.*, 2011; Osman *et al.*, 2011) which ultimately aim to transform LRC into a high-value and stable fuel that is easily handled and compatible with existing coal facilities. The success of this drying technology will therefore place LRC on equal footing with bituminous coals in the international steam coal market. Various dryers have been considered for drying coal including rotary dryers (Erisman, 1938; Yamato, 1996), tube dryers ((Bill, 1938; Akira *et al.*, 1988)), fluidized bed dryers (Ladt, 1984; Cha *et al.*, 1992; Dunlop and Kenyon, 2009), etc. However, many of the tested dryers have limitations such as large footprint, low heat and mass transfer rates, poor efficiency, non-continuous operation, high cost, not suitable for heat sensitive materials, etc. The screw conveyor dryer (SCD) overcomes much of these limitations.

The SCD offers relatively high heat transfer area-to-volume ratio (Waje *et al.*, 2006) compared to other dryers by virtue of the screw geometry which act as immersed heat transfer surface. Rotation of the screw leads to higher heat transfer coefficients due to continuous renewal of the heating surface. At the same time, agitation of the granular bed by the screw motion improves the temperature and moisture uniformity of the product. Because heat is supplied to the SCD via a heating jacket, risk of fire from drying highly combustible materials such as LRC is greatly reduced since exposure to air is minimal. The promising capabilities of SCD and its superiority over other coal drying

systems, yet the lack of comprehensive study on the device necessitates the study of granular flow and heat transfer characteristics in a screw conveyor configuration.

1.1.2 Advances in discrete element modeling of particulate processes

Particulate systems are so common in many industrial processes that fundamental understanding of the dynamics of particulate flow and heat transfer is fast becoming an important aspect of industrial research. Despite the apparent effect of equipment configuration and particle properties on the performance of the particulate processors, much of design follow empirical methods due to the high prototyping and test costs attributed to the difficulty in the measurement and control of the system. The complex interactions among particles and the surrounding medium also make it difficult to predict the dynamic behavior of the system. Understanding the underlying mechanisms in terms of these interactions is critical if granular processing and handling technologies were to advance towards greater efficiencies and sustainability.

Since the introduction of Discrete Element Method (DEM) by Cundall and Strack (1979), both academia and industry (particularly the mining industry) have started to develop their own codes. Today, at least 20 DEM codes are available with varying degrees of capabilities (see Table 1.1). The advent of DEM and the subsequent development of thermal DEM models have also facilitated the design process of particulate systems based on sound understanding of the granular flow dynamics. DEM enables engineers to study the effects of equipment design, operating parameters, and particle properties on equipment performance via ‘virtual experiments’. The latter enable

system-scale predictions using particle-scale simulation data, which are very difficult and expensive to obtain experimentally.

Table 1.1. Academic and commercial DEM codes.

Software	Owner	Licensing
BALL & TRUBAL	P. Cundall	-
Bulk Flow Analyst	Applied DEM	Licensed
Chute Maven	Hustrulid Technologies	Licensed
DEMPack	CIMNE	Licensed
EDEM	DEM Solutions	Licensed
ELFEN	Rockfield Software	Licensed
ESyS-Particle	-	Open-source
GROMOS	ETH Zurich	Licensed
LIGGGHTS/CFD-DEM	-	Open-source
LMGC90	CNRS	Open-source
MIMES	Sandia/MIT	-
Newton	AC-Tek	Licensed
PASSAGE/DEM	Techanalysis	Licensed
Pasimodo	University of Stuttgart	Collaboration only
PFC2D/PFC3D	ITASCA	Licensed
ROCKY	Conveyor Dynamics	Licensed
SimPARTIX	Fraunhofer IWM	Consultation
STAR-CCM+	CD-adapco	Licensed
Yade	-	Open-source

Although DEM was originally developed for understanding discrete mechanical interactions between particles, there have been increasing sentiments among DEM users to incorporate heat transfer capability into the basic contact mechanics model. To date, much of the effort in DEM modeling have focused on the dynamic flow behavior of

various particles in different practical geometries. This field however, is beginning to saturate judging from the number of related literature (see Table 1.3). Therefore, extending the capabilities of DEM via the development of thermal DEM is a step in the right direction, and also a logical one since granular heat transfer is ubiquitous to many particulate applications which can involve particles such as catalysts, coal, pellets, metal ores, food, minerals, and many other wet and dry solids that may be cooled, heated, or dried during the processing.

Table 1.2. Experimental studies of granular bed heat transfer.

System	References
Fluidized beds	(Vreedenberg, 1958; Zeigler and Agarwal, 1969; Bukareva <i>et al.</i> , 1971; Martin, 1984; Malhotra and Mujumdar, 1987; Borodulya <i>et al.</i> , 1991; Chen, 1999; Smolders and Baeyens, 2001; Zhu <i>et al.</i> , 2008)
Agitated and stirred beds	(Wunschmann and Schlunder, 1974; Schlunder and Mollekopf, 1984; Malhotra and Mujumdar, 1991b; Yang <i>et al.</i> , 2000)
Packed beds	(Ergun, 1952; Schotte, 1960; Sullivan and Sabersky, 1975; Whitaker, 1975; Spelt <i>et al.</i> , 1982; Schlunder, 1984; Polesek-Karczewska, 2003)
Dryers	(Lehmberg <i>et al.</i> , 1977; Toei <i>et al.</i> , 1984; Tsotsas and Schlunder, 1987; Ohmori <i>et al.</i> , 1994; Mabrouk <i>et al.</i> , 2006; Waje <i>et al.</i> , 2006; Balazs <i>et al.</i> , 2007)

The mechanisms of heat transfer between granular solids and boundary surfaces of the processors have been experimentally investigated by a number of researchers (see Table 1.2). Many of these studies have proposed empirical correlations for bed temperature, thermal conductivity, and heat transfer coefficients for a range of operating parameters. However, the validity of such correlations has limited application outside the

experimental range of variables studied (Chaudhuri *et al.*, 2011). DEM incorporated with thermal models are able to capture the dynamic particle-particle and wall-particle heat interactions which are not possible with continuum-based heat transfer models. The usefulness of DEM in industrial R&D has been exemplified by Astec Inc. use of coupled computational fluid dynamics (CFD) and DEM to simulate granular heat transfer in an aggregate drum dryer used in the production of hot mix asphalt (Hobbs, 2009).

1.2 Assessment of related work

1.2.1 Application of DEM in the study of granular flow

Since the introduction of DEM by Cundall and Strack (1979), there has been growing interest in the simulation of industrial particulate systems. Many of the early work using DEM is quite disposed from real systems in that the simulated systems are highly idealized. Early implementations of DEM simplify a 3D problem to 2D or 1D, and deal with relatively few particles in simple vessel geometries. DEM have also been used in the study of fractures and strengths of materials (Amarasiri and Kodikara, 2011; Deng *et al.*, 2011), an area of research that is traditionally approached via finite element continuum mechanical techniques, but was implemented in DEM mainly to explore the capabilities of the technique and also as a means to validate the DEM models by comparing with results from continuum methods (Xiang *et al.*, 2009). The past 30 years have seen tremendous increase in the use of DEM to simulate flow of granular media in various complex geometries. This is partly attributed to the availability of more powerful

computers and more efficient DEM codes that allow the simulation of practical systems within reasonable time.

Particle discharge from hoppers and silos are popular application of industrial DEM, and have been studied by a number of investigators. Langston *et al.* (1994), Zhu and Yu (2004), and Ristow (1997) studied the effect of physical and geometric parameters of particles and hopper on discharge flow pattern and observed that transition from funnel-flow to mass-flow behavior is affected by hopper angle. Cleary and Sawley (2002) investigated the effect of particle shape on the mass flow rate and hopper discharge profiles using 2D DEM. Particle blockiness and aspect ratio were used as parameters in the study which represented the particles as super-quadratics. It was pointed out elsewhere that the use of super-quadratics, polygons, sphere clusters, and shapes other than simple discs and spheres can increase CPU time by up to 12 times (Katterhagen *et al.*, 2009). The extent of granular segregation due to differences in particle size have also been examined (Katterhagen *et al.*, 2007) using DEM. In most of these simulations, bulk quantities such as mass flow rate and mass fraction have been measured and have been shown to agree well with experiments. Visual inspection of experimental discharge profiles using high speed camera is another validation technique that has been used (Montellano-Gonzalez *et al.*, 2011). The discrete nature of the simulations can also reveal features which are very difficult to obtain experimentally such as granular flow velocity fields, distribution of stresses (Ristow and Herrmann, 1995; Masson and Martinez, 2000), and stresses on hopper walls (Langston *et al.*, 1995; Ristow, 1997).

DEM has also been used to study the effects of various parameters on the performance of comminution devices. The effects of fill level, vessel angular speed, and material properties such as density, friction coefficients, and coefficient of restitution, on the torque and power draw in ball, centrifugal, and SAG mills have been investigated using DEM in 2D (Cleary, 2001; Cleary and Sawley, 2002; Kwan *et al.*, 2005) and 3D (Rajamani *et al.*, 2000; Mishra *et al.*, 2002). While these works focused only on the dynamics of granular material in comminution devices, there are others that accounted for particle attrition via fragmentation or chipping models (Potapov and Campbell, 1997; Ning and Ghadiri, 2006). More relevantly, Misra *et al.* (2002) studied agglomerate fragmentation in a rotary dryer using particle residence time and drying time as a parameter which controls the adhesion between particles in the agglomerates. Another approach utilizes stresses and strains to model particle breakage in an agitated dryer (Hare *et al.*, 2011). Both approaches successfully predicted the steady-state size distribution in the respective dryers.

Another common application of DEM models is the study of mixing in various blending systems including rotating drum (Chaudhuri *et al.*, 2006), V-blender (Lemieux *et al.*, 2008), double-cone blender (Chaudhuri *et al.*, 2006; Manickam *et al.*, 2010; Romanski *et al.*, 2011), Bohle tote blender (Arratia *et al.*, 2006), bladed blender (Radl *et al.*, 2010), and helical ribbon blender (Kaneko *et al.*, 2000; Bertrand *et al.*, 2005). Essentially, these works investigated the influence of blender geometry, operating conditions, and material properties on the effectiveness of the blending equipment. A number of investigators quantified content uniformity of the final product using Relative

Standard Deviation (RSD) which is well-established parameter in the pharmaceutical industry. Residence Time Distribution (RTD) data has also been used to characterize processor performance (Dubey *et al.*, 2011).

In general, when analyzing DEM results for industrial application, one may follow the seven general themes of quantitative predictions proposed by Cleary (2004) and summarized as follows (Grima and Wypych, 2011a):

1. Regions of wear and wear rates;
2. Boundary stresses;
3. Abrasion rates;
4. Impact velocity distribution, collision frequency, and energy absorption;
5. Mass flow rates and discharge patterns;
6. Mixing and segregation rates;
7. Power consumption and torques.

1.2.2 Application of DEM in the study of granular heat transfer

Chaudhuri *et al.* (2006) were among the first to use 3D DEM to simultaneously simulate flow and heating of granular material in rotating vessels. Their study focused on the mixing and heating performance of a calciner and an impregnator, represented by a cylindrical vessel and a double cone vessel respectively. Particle-particle heat transfer was modeled using standard heat balance equations and Hertzian contact mechanics to calculate the surface area of contact between two contacting particles. While the study is one of the first to implement Thermal DEM in 3D, only solid-solid contact heat transfer was considered. Schlunder (1984), Schlunder and Mollekopf (1984), and Wunschmann

and Schlunder (1974), showed that heat transfer contribution from solid-solid conduction is small compared to conduction through gas gap between the two particles. Thus, to satisfy $k_p A \gg k_g R$ (where A is contact area and R is particle radius) for which the assumptions are valid, $k_g = 0$ was imposed (Chaudhuri *et al.*, 2006; Chaudhuri *et al.*, 2011) which effectively simulated granular heat transfer in vacuum conditions. Feng *et al.* (2009) developed an alternative method called Discrete Thermal Element Method (DTEM) whereby each particle is reduced to a thermal pipe-network connecting the particle centre with each contact zone associated with the particle.

CFD and DEM coupling (CFD-DEM) is an emerging research area which has found considerable success in flow problems where traditional CFD methods fail, such as flows involving non-dilute discrete phase. For example, CFD-DEM enable the study of fluid effects in Euler-Lagrangian simulations of fluidized beds (Tsuji *et al.*, 1993; Xu and Yu, 1997; Rhodes *et al.*, 2001), spouted beds (Takeuchi *et al.*, 2004; Zhao *et al.*, 2008; Santos *et al.*, 2009), gas-solid separation in cyclone (Chu *et al.*, 2011), and pneumatic conveying of particles (Sturm *et al.*, 2010; Mezhericher *et al.*, 2011), for example. Additionally, there have been several notable attempts at more complex CFD-DEM procedures such as reaction flow modeling of char combustion in fluidized-bed (Rong and Horio, 1999; Wu and Tian, 2010; Geng and Che, 2011) and bubbling fluidized bed (Zhou *et al.*, 2004) reactors. CFD-DEM has also successfully predicted the evolution of particle radius and calcination, and the distributions of particle residence time, temperature, and calcium oxide mass fraction during chemical conversion of limestone to quicklime in a shaft kiln (Bluhm-Drenhaus *et al.*, 2010).

A pioneering application of coupled CFD-DEM to simulate drying of wet particles in a pneumatic dryer was initiated by Li and Mason (2002). Although their work demonstrated the promising implementation of DEM in drying modeling, the simulation neglected moisture evaporation which is clearly more complex than modeling gas-particle heat transfer alone. To date, there is only a handful of so-called ‘drying simulation’ that uses the DEM technique (Brosh and Levy, 2010; Mezhericher *et al.*, 2010) including the more recent 3D simulation of particle drying in a flighted rotary dryer (Hobbs, 2009). While no one has yet produced a full drying simulation that can show the moisture content distribution in both the discrete and continuous phases, even the most recent work on particulate drying using DEM still neglects the effect of evaporative cooling. There is indeed much work to be done in this area. Table 1.3 provides a non-exhaustive list of the application of DEM in the study of granular flow and heat transfer studies in different particulate systems.

Most of the prior works involving DEM have a common weakness in that the results and conclusions are largely not very useful for industrial use. For example, there are numerous studies focusing on the analysis of particle velocity in particulate processors whereas such microscopic analysis is probably useful only in academia. To the author’s knowledge, there is very few works that incorporate thermal DEM in their dynamic study. Clearly, thermal DEM is the way forward in the use of DEM for industrial purposes since most practical particulate processors can involve complex coupled processes such as reactions, combustions, and drying.

Table 1.3. Flow and heat transfer studies of particulate systems using DEM.

System	Method	Focus	Reference
Rotary mixer	3D DEM	Flow and heat transfer	(Chaudhuri <i>et al.</i> , 2006)
Double-cone blender	3D DEM	Flow and heat transfer	(Chaudhuri <i>et al.</i> , 2006)
Hopper	2D DEM	Flow study	(Cleary and Sawley, 2002)
	2D CFD-DEM	Flow and heat transfer study	(Kruggel-Emden <i>et al.</i> , 2006)
	3D DEM	Flow study	(Katterhagen <i>et al.</i> , 2007)
Wire mesh screen	3D DEM	Flow study	(Delaney <i>et al.</i> , 2009)
Packed bed	2D DEM/DTEM	Heat transfer study	(Feng <i>et al.</i> , 2009)
Vertical shaft kiln	CFD-DEM	Flow and heat transfer	(Bluhm-Drenhaus <i>et al.</i> , 2010)
Silo	3D DEM	Flow study	(Montellano-Gonzalez <i>et al.</i> , 2011)
Belt conveyor	3D DEM	Flow study	(Grima and Wypych, 2011b)
Swing-arm and translating tube slump testers	3D DEM	Flow study	(Grima and Wypych, 2011a)
Agitated bed dryer	3D DEM	Flow and attrition	(Hare <i>et al.</i> , 2011)
Paddle mixer	3D DEM	Flow study	(Hassanpour <i>et al.</i> , 2011)
Fluidized bed	2D/3D CFD-DEM	Flow and heat transfer	(Shimizu, 2006)

Indeed, the use of CFD-DEM and general-purpose DEM to simulate large practical systems require powerful computers and long CPU time. It was reported that it

took around 15 days to simulate the complete combustion (600 s of simulation time) in a fluidized bed reactor with 8000 graphite particles (3 mm diameter) using a 2.66 GHz Intel Core 2 Duo CPU (Geng and Che, 2011). Due to the computational requirement of the technique, many of the reported DEM simulations are 2D or scaled-down versions of the practical systems. It is hoped that with rapid advancements in memory, and high-speed processor technology, coupled with high-performance parallel computing, the hardware bottleneck will diminish to allow for more realistic simulations of larger systems.

1.2.3 Study of granular flow and heat transfer screw conveyors

Experimental studies of screw conveyors have mostly focused on the influence of operating conditions (Stevens, 1966; Carleton *et al.*, 1969; Zareiforoush *et al.*, 2010b) and material properties (Rehkugler, 1958; Dai and Grace, 2011) on the performance characteristics of the device. The influence of screw geometry has also been investigated, covering special screw configurations including tapered-shaft, cut-flight, stepped-flight, variable pitch, tapered-flight, double-flight, and other combinations (Stevens, 1966; Burkhardt, 1967; Tsai and Lin, 1994; Chang and Steele, 1997; Yu and Arnold, 1997; Sinnott *et al.*, 2011b). A number of articles have reported the effect of inclination (Chang and Steele, 1997) and a few others have investigated the influence of granular vortex motion (Roberts, 1999), fullness, screw geometry, etc., on volumetric capacity, efficiency, and required power of vertical screw conveyors (O'Callaghan, 1962; Rademacher, 1974).

Heat transfer studies involving screw conveyor dryer was first conducted by Sabarez and Noomhorm (1993) through their work on screw conveyor roasting of cashew nuts. However, the scope of this study is very narrow, reporting only on the effect of SCD surface temperature on kernel yield and whiteness. To the author's knowledge, no other studies on screw conveyor heater or dryer was reported until almost a decade later when Benali and Kudra (2001) developed a multistage SCD consisting of seven identical treatment stages in cascade arrangement. Each drying stage consisting of nine parallel troughs fitted with a 4.5 m long screw (152 mm diameter and 110 mm pitch). Such arrangement enable high throughput and better control of the drying process since the screw speed of each stage can be set independently. A number of other SCD developments have been reported in recent years including the double-flight SCD for drying sewage sludge (Kim *et al.*, 2005), direct-contact SCD for processing biomass residues (Al-Kassir *et al.*, 2005), and jacketed SCD with nitrogen gas-filled trough for drying heat-sensitive crystalline solids (Waje *et al.*, 2006). Despite, the industrial significance of SCD, very few lab-scale and pilot-scale SCD have been reported.

There are at least twenty patents related to thermal dehydration of raw feedstock using screw conveyor devices. For example, Comolli (1979) disclosed a process of drying wet lignite using a multistage SCD whereby coal is first subjected to rapid drying at atmospheric pressure, followed by a slow drying at elevated pressure and high humidity condition, before finally entering the cooling stage. Many of the reported SCD design use jacketed trough where heat may be provided by hot water, steam, or flue gases

(McCabe, 1991; Azuma, 2001) but there are also others that implement electric coil heating (Mentz, 1995; Okada, 2004). Various flight configurations were also disclosed to mitigate some problems associated with the screw conveyance of certain feedstock material. For example, Mentz (1995) addressed agglomeration and dust problems during the drying of solid materials in SCD by incorporating cut and folded screw flights. A separate patent document disclosed a hollow twin screw conveyor design for removing volatiles from the feedstock (McCabe, 1991), while another described the use of tapered screw to express surface water out of the material before commencing thermal drying (Costarelli, 1985). A review of drying technologies and patents of LRC application can be found in Osman *et al.* (2011).

The experimental and theoretical studies on the flow and heat transfer of granular media in screw conveyor configurations are useful for a general insight to the characteristics of the processor for a specific material and screw configuration, but may not be applicable outside the range of materials or parameters tested. The need for lab-scale and/or pilot-scale tests for a new screw configuration or new materials increases development costs and man-hour. Using DEM as a prototyping and testing tool via ‘virtual experiments’, the iterations of physical prototypes can be dramatically reduced.

A number of DEM simulations have been carried out to study the granular flow characteristics of screw conveyors. Key parameters such as transfer velocity, critical angle, torque, power with respect to different operating conditions of volumetric and mass flow rate, screw speed, etc. were investigated. DEM prediction of quantifiable

parameters such as mass flow rates of horizontal (Owen and Cleary, 2009b; Owen and Cleary, 2009a; Hu *et al.*, 2010), vertical (Shimizu and Cundall, 2001; McBride and Cleary, 2009; Sinnott *et al.*, 2011b), and inclined (Owen and Cleary, 2009b; Owen and Cleary, 2009a) screw conveyors were found to be in good agreement with experimental values. The effect of particle shape and friction on bulk flow patterns and power draw were also investigated using 2–3 mm particles with shape factors and aspect ratios between 2–4 and 0.55–1 respectively (Owen and Cleary, 2009). Particle flow patterns in different screw configurations (standard, tapered-flight, tapered-shaft, variable-pitch, and tapered-shaft with variable-pitch screw) were also investigated, specifically to study the dependency of hopper draw down. To date, no drying or heat transfer simulation of particle bed in screw conveyor heater or dryer has been carried out using DEM. Table 1.4 summarizes the theoretical, experimental, and simulation studies on granular flow and heat transfer in screw conveyor configurations conducted in the past.

Table 1.4. Study of granular flow and heat transfer in screw conveyors.

Configuration	Method	Details	Reference
Screw extruder	Experimental and theoretical model	Flow and heat transfer study; Developed a model to simulate the flow and heat transfer non-Newtonian fluid through a single screw extruder.	(Gopalkrishna and Jaluria, 1992)
Screw extruder	3D DEM	Flow and heat transfer study; Flood feeding of HDPE particles (3 mm, 945 kg m ⁻³) through a screw feeder with temperature of barrel and screw set at 80 °C. Flow behavior is analyzed in terms of down and cross-channel velocity profiles, particle coordination number, and RTD. Heat transfer was qualitatively studied by temperature contour plots.	(Moysey and Thompson, 2005)
Screw feeder	Experimental	Flow study; Studied the mechanism of blockage in a screw feeder and determine effects of particle size (0.45-9.8 mm), size distribution, shape, moisture content (8-60 %), particle density (330-1200 kg m ⁻³), and compressibility.	(Dai and Grace, 2011)
Horizontal screw conveyor	3D DEM	Flow study; The effect of rotational speed on the solid mass flow rate obtained from simulation correlates well with experimental data. Also studied the effect of particle properties on other performance measures such as particle speed and power draw.	(Owen and Cleary, 2009b; Owen and Cleary, 2009a)

Table 1.4. (continued)

Horizontal screw conveyor	Experimental	Flow study; Studied the effect of screw diametric clearance and screw rotational speed on the throughput and power requirements of screw conveyor during transportation of rough rice grains.	(Zareiforouh <i>et al.</i> , 2010a; Zareiforouh <i>et al.</i> , 2010b)
Horizontal screw conveyor	3D DEM	Flow study; Studied the performance of a screw conveyor by analyzing particle trajectory, angular and axial velocities, overall torque and force, kinetic energy, and energy dissipation; Periodic boundary condition was applied to a single screw pitch.	(Hu <i>et al.</i> , 2010)
SCD (direct heating)	Experimental and theoretical model	Heat transfer study;	(Al-Kassir <i>et al.</i> , 2005)
SCD (indirect heating)	Experimental	Heat and mass transfer study; Studied the performance of a lab-scale furnace-heated SCD for roasting cashew nuts. Quality index based on whole kernel yield and kernel color is comparable or better than those obtained from hot-oil bath roasting method and marketed product.	(Sabarez and Athapol, 1993)

Table 1.4. (continued)

SCD (indirect heating)	Experimental	Flow, heat and mass transfer study; Comprehensive performance evaluation of water-heated screw conveyor dryer (3 m length and 0.072 screw diameter). Overall heat transfer coefficient was reported to be in the range of 46-102 W m ² K with thermal efficiency in the range of 25-62 %. It was also reported that low pressure drying can remove up to 92% moisture.	(Waje <i>et al.</i> , 2006; Waje <i>et al.</i> , 2007a; Waje <i>et al.</i> , 2007b)
SCD (direct and indirect heating)	Experimental	Heat and mass transfer study; Developed a double-flight screw conveyor dryer for drying sewage sludge in flue gas which successfully reduced moisture content from 80% to 10-20%. Energy efficiency of dryer was reported to be in the range of 70-75% at sludge feed rate of 100 kg h ⁻¹ .	(Kim <i>et al.</i> , 2005)
Multistage SCD (indirect heating)	Experimental	Heat and mass transfer study; Developed a multistage SCD consisting of seven identical treatment stages in cascade arrangement, with each stage consisting of nine parallel troughs fitted with a 4.5 m long screw (152 mm diameter and 110 mm pitch). The SCD was used for processing raw pig manure into fertilizers.	(Benali and Kudra, 2001; Benali and Kudra, 2002)

Table 1.4. (continued)

‘OLDS’ elevator	Experimental and 3D DEM	Flow study; The ‘OLDS’ elevator is a vertical screw conveyor with a rotating case and stationary screw. Studied the flow of wheat, sorghum, and fine aggregate, and the effect of key operating parameters (screw speed, bed depth, tip clearance, cutter height, etc.) and material properties on performance of the device.	(McBride and Cleary, 2009)
Vertical screw conveyor	3D DEM	Flow study; Studied the effect of screw speed on transfer angle, transfer velocity, mass flow rate; and the effect of fill level on power draw. Results of simulation study agree well with theory.	(Shimizu and Cundall, 2001)
Inclined double-flight screw conveyor	Experimental	Flow study; Investigated the effect of flight type, inclination angle, intake length, and rotation speed on grain damage, power draw, conveying capacity, and conveying energy efficiency. It was found that double helix screw required less power and provided higher conveying capacity and higher energy efficiency compared to other flight types.	(Chang and Steele, 1997)

Table 1.4. (continued)

Vertical double-flight screw mill	3D DEM	Flow study; Investigated the effect of grinding media shape and slurry viscosity on media flow and energy consumption in a tower mill. Simulation data were analyzed in terms of energy dissipation rate, media velocity components, bed pressure, power draw, collisional energy, and abrasive wear of mill.	(Sinnott <i>et al.</i> , 2011a; Sinnott <i>et al.</i> , 2011b)
Twin-screw dryer	Experimental	Heat and mass transfer study; Developed a double-flight SCD for drying sewage sludge has the capability of removing up to 90% moisture with efficiency of 70-75% at sludge feed rate of 100 kg h ⁻¹ .	(Kim <i>et al.</i> , 2005)
Screw variants	Experimental	Flow study; The experimental rig uses five kinds of screws: (a) taper-shaft, (b) cut-flight, (c) cut-flight and paddles, (e) stepped-flight, and double-flight.	(Tsai and Lin, 1994)
Screw variants	Experimental and Theoretical	Flow study; The experimental rig uses two kinds of screws: (a) taper-shaft and stepped-pitch, and (b) stepped-shaft and stepped-pitch.	(Yu and Arnold, 1997)
Screw variants	3D DEM	Flow study; Investigated the effect of screw configuration on the hopper draw down flow, mass flow rates, and power draw. Six screws were used for the study: (a) standard, (b) taper-flight, (c) variable pitch, (d) variable pitch and taper-shaft, (e) taper-flight and taper-shaft, (f) optimized variable-pitch and taper-shaft.	(Fernandez <i>et al.</i> , 2009)

1.3 Objectives

The main objective of this research work is to understand the mixing dynamics and heat transfer characteristics of particles in a screw conveyor dryer. As a first step towards this objective, this work will simulate particle-particle and vessel-particle heat transfer by conduction and conduction while neglecting cooling effect due to drying. This initial work will also assume constant particle size, and neglect any species transfer effects. Therefore, this work can be considered as a heat transfer problem in addition to the Newtonian laws governing the flow of discrete particles. Results from this initial study will be useful for future innovative screw conveyor heater and dryer designs.

1.4 Outline of thesis

Chapter 1 provides a literature review of articles related to thermal DEM simulations, screw conveyor, and DEM analysis, to set the tone of the work. In the same chapter, the motivation for the work and the scope of the work are also presented. In Chapter 2, the theoretical framework of DEM, heat transfer correlations, and numerical aspects of DEM will be presented. Chapter 3 is dedicated an integral aspect of this work, that is, the determination of parameters affecting flow and heat transfer using calibration techniques. Calibration is necessary as it tunes the simulation parameter so that bulk thermal and flow behavior matches experimental data. The parameters to be calibrated are carefully selected such that calibrated microscopic property will be independent of vessel geometry. This allows the same parameter values to be used for larger simulations and avoid the need for validation of the larger systems which in most cases is not very

feasible. Chapter 4 provides in depth analysis of DEM results in terms of granular flow characteristics of glass particles in a short screw conveyor. Chapter 5 analyses the DEM results in terms of heat transfer characteristics of the screw conveyor heater. Chapter 4 and Chapter 5 aims to provide insights on the flow and heat transfer behavior of granular materials with respect to different operating conditions of screw speed, mass flow rate, angle of inclination, and pitch-to-diameter ratio using glass beads as the bed material. The objective here is to utilize trends obtained from the DEM studies for innovative designs of SCD and pave the way for more complex SCD simulations involving coupled heat and mass transfer in the next phase of our modeling effort. Finally, the entire work is consolidated and concluded in Chapter 6.

Chapter 2

Theoretical Background

2.1 Molecular Dynamics and DEM Theory

In molecular dynamic (MD) simulations of granular matter, the choice of inter-particle contact laws determines the net force and moment on each grain. A number of contact force models are available in literature to approximate the collisional dynamics to various extents. Cundall and Strack (1979) developed the linear spring and dashpot model whereby the magnitude of the normal force between two particles is the sum of spring force and damping force. Other models include: particle adhesion and detachment models of JKR (Johnson *et al.*, 1971) and DMT (Derjaguin *et al.*, 1975), soft-sphere and hard-sphere force schemes (Schafer *et al.*, 1996), inelastic frictional sphere models (Walton, 1993), and several others (Zhou *et al.*, 1999; Potyondy and Cundall, 2004; Ai *et al.*, 2011). There is however, very little evidence to suggest that the choice of the contact model actually affects the flow dynamics in large scale systems for the materials found in most industrial and geophysical flows (Cleary, 2007). In this thesis, we use the Hertz (1882) contact theory to model the normal force components, and the model of Mindlin and Deresiewicz (1953) for tangential force components.

2.1.1 Equations of motion

The translational and rotational motion of each individual particle is governed by the standard equations of Newton and Euler for rigid body dynamics. Newton's Second Law states that the rate of change of linear momentum of a particle with a constant mass is equal to the sum of all external forces acting on the particle. In most practical applications, gravity is also accounted for. In general,

$$\mathbf{F}_i = m_i \frac{d}{dt} \left(\frac{d\mathbf{x}_i}{dt} \right) \quad (2.1)$$

$$\mathbf{T}_i = I_i \frac{d\boldsymbol{\omega}_i}{dt} \quad (2.2)$$

where \mathbf{F}_i is resultant force, m_i is mass of the element, \mathbf{x} is the element centroid displacement in a fixed coordinate frame, \mathbf{T}_i is the resultant moment about the central axes, I_i is the moment of inertia, and $\boldsymbol{\omega}_i$ is angular velocity (see Fig. 2.1).

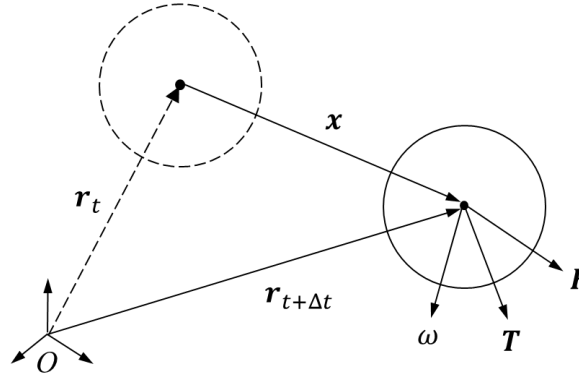


Fig. 2.1. Motion of a discrete particle.

Vectors \mathbf{F}_i and \mathbf{T}_i are sums of all forces $\mathbf{F}_i^{\text{ext}}$ and moments $\mathbf{T}_i^{\text{ext}}$ applied to element i due to external loads, contact interactions \mathbf{F}_{ij} with neighboring particles, and forces \mathbf{F}_i^{d} and moments \mathbf{T}_i^{d} due to external damping (Rojek *et al.*, 2011). In most

scenario, $\mathbf{F}_i^{\text{ext}}$ includes gravitational force, while other external loads such as electrostatic force, force due to fluid momentum, drag, etc., must be taken into account where applicable.

$$\mathbf{F}_i = \sum_{j=1}^N \mathbf{F}_{ij} + \mathbf{F}_i^{\text{ext}} + \mathbf{F}_i^{\text{d}} \quad (2.3)$$

$$\mathbf{T}_i = \sum_{j=1}^N (\mathbf{r}_{pi} \times \mathbf{F}_{ij}) + \mathbf{T}_i^{\text{d}}. \quad (2.4)$$

The above equations give the expressions for \mathbf{F}_i and \mathbf{T}_i , with \mathbf{r}_{pi} representing the vector connecting the center of mass of element i with its contact point with element j . The contact force between two elements \mathbf{F}_{ij} can be decomposed into normal and tangential components

$$\mathbf{F}_{ij} = \mathbf{F}_n + \mathbf{F}_t. \quad (2.5)$$

We use Discrete Element Method (DEM) developed by Cundall and Strack (1979) to solve the Newton equations for an assembly of soft elasto-frictional spheres that interact via Hertz-Mindlin contact forces and Coulomb friction (Makse *et al.*, 2004). This is described in the following section.

2.1.2 Hertz-Mindlin contact model

Granular materials are modeled by representing their geometry as a random assembly of elastic spheres, formulating a contact force-displacement law that relates the contact force acting between two spheres to their relative displacement (Elata and Berryman, 1996). The Hertz-Mindlin contact model assumes that the solids are isotropic

and elastic, and the overlap between two contacting elements is very small compared to the radii of curvature of the respective undeformed bodies. While the original contact force-displacement law of Cundall and Strack (1979) is based on the linear spring and dashpot model, the Hertz-Mindlin model is nonlinear elastic, with path dependence and dissipation due to slip, and omits relative roll and torsion between the two spheres.

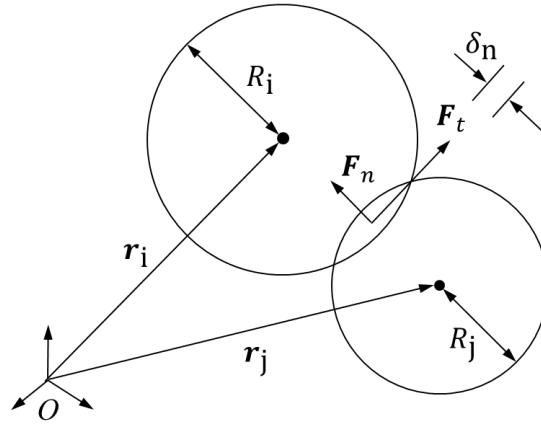


Fig. 2.2. Contact between two discrete particles.

The soft-sphere approach allows two contacting elements to slightly overlap by a quantifiable amount δ_n which is referred to as the normal overlap and expressed as

$$\delta_n = R_i + R_j - |\mathbf{r}_i - \mathbf{r}_j| \quad (2.6)$$

where R_i and R_j are the radii of particle i and j respectively, and \mathbf{r}_i and \mathbf{r}_j are the position vectors of their respective centers of mass (see Fig. 2.1). The overlapping serves as a mechanism for contact detection in DEM. A unit vector \mathbf{r}_n normal to the contact area is defined as

$$\mathbf{r}_n = \frac{\mathbf{r}_j - \mathbf{r}_i}{|\mathbf{r}_j - \mathbf{r}_i|}. \quad (2.7)$$

Two particles in contact with each other exert a force \mathbf{F} at the contact point according to Newton's Law. The normal force-displacement relationship of the Hertz model (Hertz, 1882) is given by

$$\mathbf{F}_n = F_n \mathbf{r}_n \quad (2.8)$$

where the magnitude of normal force F_n is defined as

$$F_n = \frac{4}{3} E^* \sqrt{R^*} \delta_n^{3/2}. \quad (2.9)$$

The equivalent Young's Modulus E^* between two particles is defined in terms of the Poisson ratio ν of each particle in the contact

$$\frac{1}{E^*} = \frac{1 - \nu_i^2}{E_i} + \frac{1 - \nu_j^2}{E_j} \quad (2.10)$$

with the Young's Modulus E expressed as

$$E_i = 2G_i(1 + \nu_i) \quad (2.11)$$

where G is Shear Modulus. The equivalent radius R^* is defined as

$$\frac{1}{R^*} = \frac{1}{R_i} + \frac{1}{R_j}. \quad (2.12)$$

The magnitude of normal damping force F_n^d is defined as (DEM Solutions, 2011)

$$F_n^d = -2 \sqrt{\frac{5}{6}} \gamma v_n^{\text{rel}} \sqrt{S_n m^*} \quad (2.13)$$

where v_n^{rel} is the normal component of relative velocity, and m^* is the equivalent mass of the contacting particles defined as

$$\frac{1}{m^*} = \frac{1}{m_i} + \frac{1}{m_j}. \quad (2.14)$$

The normal stiffness S_n , and parameter γ , which is related to the coefficient of restitution C_R , are expressed as

$$S_n = 2E^* \sqrt{R^* \delta_n} \quad (2.15)$$

and

$$\gamma = \frac{\ln(C_R)}{\sqrt{\ln(C_R) \cdot \ln(C_R) + \pi^2}}. \quad (2.16)$$

Tangential deformation at cohesive contacts is accounted for by the tangential overlap δ_t and can be defined by integrating the tangential relative speed of particle i and j at the contact point. Unlike normal overlap δ_n , tangential overlap δ_t requires integration of particle trajectory over time and cannot be determined from instantaneous particle positions alone (Pournin and Liebling, 2008). Mindlin and Deresiewicz (1953) model for the tangential component of contact force F_t between two overlapping particles is given as a function of tangential overlap vector $\boldsymbol{\delta}_t$ and tangential stiffness S_t :

$$\mathbf{F}_t = -\boldsymbol{\delta}_t S_t \quad (2.17)$$

with

$$S_t = 8G^* \sqrt{R^* \delta_n} \quad (2.18)$$

where the equivalent Shear Modulus G^* is expressed as

$$G^* = \frac{2 - \nu_i}{G_i} + \frac{2 - \nu_j}{G_j}. \quad (2.19)$$

The tangential damping force F_t^d is given by

$$F_t^d = -2 \sqrt{\frac{5}{6}} \gamma v_t^{\text{rel}} \sqrt{S_t m^*} \quad (2.20)$$

where v_t^{rel} is the tangential component of relative velocity. The tangential force is limited by Coulomb friction $\mu_s F_n$ exceeding which, result in sliding of one surface over the other. At any particular time, F_t falls into one of the two regimes defined as

$$\mathbf{F}_t = \begin{cases} \mathbf{F}_t & \text{if } |\mathbf{F}_t| \leq \mu_s F_n \\ \frac{\mathbf{F}_t}{|\mathbf{F}_t|} \mu_s F_n & \text{if } |\mathbf{F}_t| > \mu_s F_n \end{cases} \quad (2.21)$$

The resultant contact force \mathbf{F}_{ij} on particle i due to contact with particle j is the vector addition of the normal and tangential force vectors

$$\mathbf{F}_{ij} = \mathbf{F}_n + \mathbf{F}_t. \quad (2.22)$$

Rolling friction is accounted for by applying torques between contacting surfaces using

$$\mathbf{T}_i = -\mu_r \mathbf{F}_n R_i \boldsymbol{\omega}_i \quad (2.23)$$

where μ_r is the coefficient of rolling friction between two surfaces, R_i is the distance between contact point and center of mass, and ω_i is the unit angular velocity vector of the object at the contact point.

2.2 Heat Transfer in Granular Beds

Heat transfer from heated surfaces to packed or agitated beds is controlled by contact resistance between the surface and first particle layer, followed by thermal penetration resistance in the bulk. For packed beds (static), contact resistance and bulk penetration resistance can be determined from physical properties of the materials involved. For agitated or moving beds, the prediction of bulk penetration resistance require that empirical parameter(s) be determined from experiments (Schlunder, 1984). The most basic granular heat transfer model consists of three basic mechanisms (Ohmori *et al.*, 1994):

- i. Wall-to-surface heat transfer;
- ii. Heat penetration in packed beds;
- iii. Granular convection.

The first mechanism represents heat transfer through the interfacial contact resistance between the heated surface (wall) and the first particle layer adjacent to the wall (surface). The second mechanism is responsible for the penetration of heat from the first particle layer (surface) to the rest of the bed (bulk) through granular contact. The final mechanism accounts for the intensification of heat transfer due to particle motion in moving beds. These mechanisms can be represented by resistances in series as shown in Fig. 2.3.

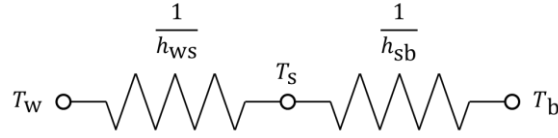


Fig. 2.3. Series heat transfer resistances between wall and bulk.

2.2.1 Wall-to-surface heat transfer

Experimental observation of heat transfer to packed beds showed a sharp temperature drop between the surface of the immersed body and the surface of the adjacent bed, leading to a conclusion that there exists of an interface contact resistance (Seidel, 1965; Kwapinska *et al.*, 2008). The presence of air gap between the immersed surface and the adjacent particle, solid-solid contact, and radiation contributes to the so-called contact resistance. The following expression is recommended for calculating the contact heat transfer coefficient h_{ws} (Schlunder, 1984):

$$h_{ws} = \phi_w h_{wp} + (1 - \phi_w) \frac{2k_g/d}{\sqrt{2} + (2l + 2\alpha)/d} + h_{rad} + h_{dir} \quad (2.24)$$

where the wall coverage factor ϕ_w is approximately 0.8. The heat transfer coefficient between wall and a single particle h_{wp} is a function of gas conductivity k_g , modified mean free path of gas molecules l , and particle surface roughness α :

$$h_{wp} = \frac{4k_g}{d} \left[\left(1 + \frac{2l + 2\alpha}{d} \right) \ln \left(1 + \frac{d}{2l + 2\alpha} \right) - 1 \right] \quad (2.25)$$

$$l = \frac{32\mu_g(2 - \phi_A)}{5p\phi_A} \times \sqrt{\frac{R_G T}{2\pi\mathcal{M}}} \quad (2.26)$$

The accommodation coefficient ϕ_A is determined using the correlation of Martin (1984) expressed as

$$\log\left(\frac{1}{\phi_A} - 1\right) = 0.6 - \frac{1}{2.8}\left(\frac{1000}{T} + 1\right). \quad (2.27)$$

For normal gases at moderate temperatures, ϕ_A is around 0.8-1. Radiation and solid-solid conduction heat transfer are accounted using

$$h_{\text{rad}} = \frac{4\sigma T^3}{\frac{1}{\epsilon_w} + \frac{1}{\epsilon_b} - 1} \quad (2.28)$$

$$h_{\text{dir}} = \frac{2ak_p}{d^2}. \quad (2.29)$$

Heat transfer due to solid-solid contact is negligible at atmospheric pressure and is still very small in vacuum condition unless good conductors (such as metal particles) are used (Schlunder, 1984; Schlunder and Mollekopf, 1984). Equations (2.24) to (2.29) are used to calculate h_{ws} , which was shown to be dependent on material property and is not influenced by the geometry of the containing vessel.

2.2.2 Heat penetration in granular beds

Penetration of heat from the first particle layer to the bulk is described by the classical Penetration Model (PM). Starting with the energy balance for a packed bed

$$mc \frac{dT_b}{dt} = h_{\text{sbt}} A (T_w - T_b), \quad (2.30)$$

and then integrating the above with respect to time and bulk temperature to obtain

$$-\ln \frac{T_w - T_b}{T_w - T_{b0}} = \frac{Ah_{\text{sbt}}}{mc} t. \quad (2.31)$$

Assuming the bed is a semi-infinite solid with effective thermal conductivity k_b , density ρ_b , and heat capacity c_b , Fourier's equation for heat conduction can be solved by imposing a Dirichlet boundary condition to yield the instantaneous bulk heat penetration coefficient h_{sbt} and its corresponding time-average value h_{sb} :

$$h_{sbt} = \sqrt{\frac{k_b \rho_b c_b}{\pi t}} \quad (2.32)$$

$$h_{sb} = 2 \times \sqrt{\frac{k_b \rho_b c_b}{\pi t}}. \quad (2.33)$$

The empirical parameter k_b can be determined by fitting equation (2.33) to the $\sqrt{1/t}$ dependent portion of the h versus t graph derived from packed bed heating curve. k_b can also be estimated from the correlation of Zehner (1973) and Bauer (1977) which applies to monodispersed and polydispersed packed beds of spherical and non-spherical particles of poor and good conductors within a wide temperature and pressure range of $100 < T < 1500$ K and $10^{-3} < p < 100$ bar respectively (Schlunder, 1984). The correlation is

$$\begin{aligned} \frac{k_b}{k_g} = (1 - \sqrt{1 - \psi}) & \left[\frac{\psi}{\psi - 1 + k_g/k_D} + \psi \frac{k_{rad}}{k_g} \right] \\ & + \sqrt{1 - \psi} \left[\phi_k \frac{k_p}{k_g} + (1 - \phi_k) \frac{k'_b}{k_g} \right] \end{aligned} \quad (2.34)$$

$$\begin{aligned}
\frac{k'_b}{k_g} = \frac{2}{K} & \left\{ \frac{B}{K^2} \frac{k_g}{k_D} \frac{k_g}{k_p} \left(\frac{k_p}{k_g} + \frac{k_{\text{rad}}}{k_G} - 1 \right) \right. \\
& \times \ln \frac{\frac{k_g}{k_D} \left(\frac{k_p}{k_g} + \frac{k_{\text{rad}}}{k_g} \right)}{B \left[1 + \left(\frac{k_g}{k_D} - 1 \right) \left(\frac{k_p}{k_g} + \frac{k_{\text{rad}}}{k_g} \right) \right]} \\
& + \frac{B+1}{2B} \left[\frac{k_{\text{rad}}}{k_g} \frac{k_g}{k_D} - B \left(1 + \frac{k_{\text{rad}}}{k_g} \left(\frac{k_g}{k_D} - 1 \right) \right) \right] \\
& \left. - \frac{B-1}{K} \frac{k_g}{k_D} \right\}
\end{aligned} \tag{2.35}$$

$$\begin{aligned}
K = \frac{k_g}{k_D} & \left[1 + \left(\frac{k_{\text{rad}}}{k_g} - B \frac{k_D}{k_g} \right) \frac{k_g}{k_p} \right] \\
& - B \left(\frac{k_g}{k_D} - 1 \right) \left(1 + \frac{k_{\text{rad}}}{k_g} \frac{k_g}{k_p} \right)
\end{aligned} \tag{2.36}$$

$$B = C_{\text{form}} \left(\frac{1-\psi}{\psi} \right)^{10/9} f(\xi) \tag{2.37}$$

$$\frac{k_{\text{rad}}}{k_g} = \frac{4\sigma}{2/\epsilon_p - 1} T^3 \frac{x_R}{k_g} \tag{2.38}$$

$$\frac{k_D}{k_g} = \frac{x_D}{x_D + l} \tag{2.39}$$

where k_p and k_g are the particle and gas thermal conductivity respectively, k_{rad} and k_D are the equivalent conductivity due to radiation and molecular flow respectively, d is particle diameter, ψ is void fraction, ϕ_k is relative flattened particle-surface contact area, C_{form} is particle shape factor, and $f(\xi)$ is particle size distribution function.

$f(\xi) = 1$ for monodispersed spheres and ϕ_k is around 0.008 for ceramic, 0.0013 for steel, and 0.0253 for copper. For monodispersed packed beds,

$$x_R = R_{\text{form}}d \quad (2.40)$$

$$x_D = D_{\text{form}}d \quad (2.41)$$

where R_{form} and D_{form} are shape factors for interstitial energy transport by radiation and molecular flow respectively and $d = \sqrt[3]{6V/\pi}$. For spherical particles, $C_{\text{form}} = 1.25$ and $R_{\text{form}} = D_{\text{form}} = 1$.

2.2.3 Overall heat transfer coefficient

The Penetration Model (PM) allows the overall wall-to-bulk heat transfer coefficient h to be estimated using only mechanisms (i) and (ii) (see Fig. 2.3), with mechanism (iii) accounted for in (ii) via an empirical parameter known as effective bed thermal conductivity k_{bed} . Using equations (2.24) and (2.33), the overall heat transfer coefficient h between the heated wall and the packed bed can be calculated using (Schlunder, 1984; Malhotra and Mujumdar, 1991a; Ohmori *et al.*, 1994):

$$\frac{1}{h} = \frac{1}{h_{\text{ws}}} + \frac{1}{h_{\text{sb}}}. \quad (2.42)$$

From equation (2.42), it is clear that there exist two limiting cases for the overall heat transfer coefficient h , namely, the contact-controlled regime, and the penetration-controlled regime. In the contact-controlled regime, h is limited by the contact resistance between the wall and surface particles provided thermal resistance in the bulk is negligible ($h_{\text{sb}} \rightarrow \infty$). In this limiting case, the bulk temperature T_b rapidly

equalizes with the surface particle temperature T_s so that $T_b = T_s$ at all times. Thus, the contact-controlled regime must obey equation (2.31) with $h = h_{ws}$ and $T_b = T_s$:

$$-\ln \frac{T_w - T_b}{T_w - T_{b0}} = \frac{Ah_{ws}}{mc} t. \quad (2.43)$$

Conversely, the penetration-controlled limiting case is imposed when contact resistance is negligible ($h_{ws} \rightarrow \infty$) such that T_s rapidly attains the wall temperature T_w while bulk temperature T_b evolves according to the transient heat equation with Dirichlet boundary conditions. Thus, the penetration-controlled limiting case must obey equation (2.33) reproduced here for convenience:

$$h = h_{sb} = 2 \times \sqrt{\frac{k_b \rho_b c_b}{\pi t}}. \quad (2.44)$$

The above limiting cases will be used to determine the wall-to-particle heat transfer coefficient h_{wp} and the particle-to-particle heat transfer coefficient h_{pp} in the DEM simulations.

2.3 DEM Framework

A discrete element software package commercially known as EDEM (DEM Solutions) has been used for all simulations in the present work. The core EDEM code is mostly based on the work of Cundall and Strack (1979), incorporating the time-stepping method of Ning (1995), and damping technique of Tsuji *et al.* (1999) and Zhang and Whitten (1996). DEM simulations generally consist of seven steps which are outlined in Fig. 2.4 which begins with generation of particles according to the desired physical

specifications, followed by contact detection which can be achieved by various algorithms outlined in a number of articles (He and Dong, 2007; Mio *et al.*, 2007; Jin *et al.*, 2011). Once the contacts between elements are established, the forces, accelerations, velocities, and positions of each element can then be updated.

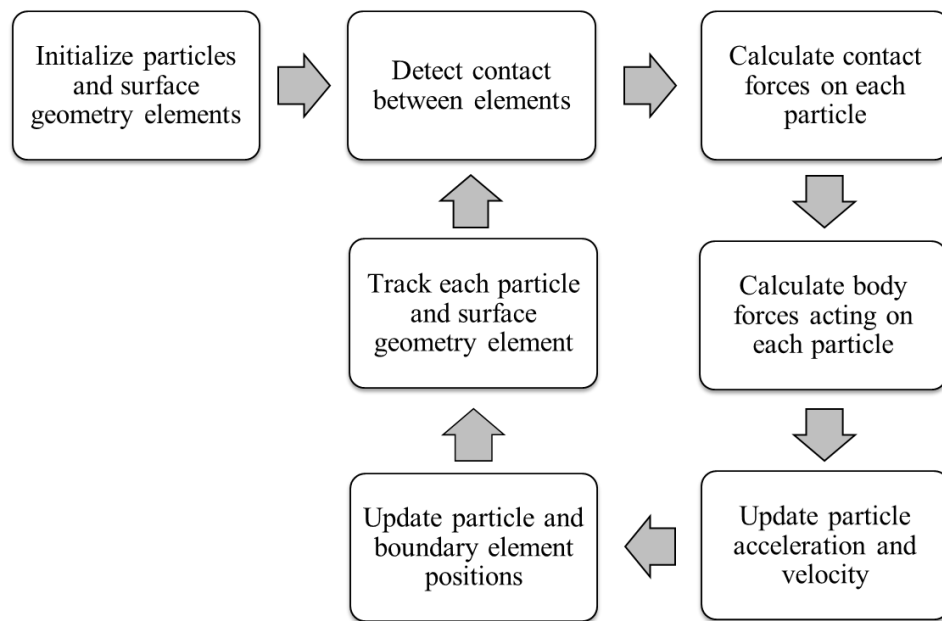


Fig. 2.4. DEM numerical flow at every time-step (DEM Solutions, 2011).

2.3.1 Contact detection algorithm

Contact detection by brute force involves the looping over every particle to check the contact of each particle with other particles in the simulated system of n particles, introducing a $O(n^2)$ complexity which is inefficient and computationally expensive. One way to avoid this global particle-to-particle contact search is to divide the simulation domain into bins or grid cells. Each cell is identified as active or inactive, where active cells contain two or more particles, and inactive cells contain only one particle or none.

Only particles in active cells are checked for contacts, while those in inactive cells are ignored (see Fig. 2.5), reducing the complexity to $O(n)$ and enable the simulation to progress faster (Walizer and Peters, 2011). Note that unlike mesh cells in fluid dynamic and finite element computations, bins in DEM do not serve any numerical purpose other than to facilitate the contact detection algorithm. The size of the bin must be carefully selected to ensure that it is big enough to contain the centers of mass of at least two particles (bin width equal to particle diameter is usually recommended), yet not exceedingly large as to enclose too many particles and complicate the search algorithm (Williams and Connor, 1999; He and Dong, 2007). Although bin size has no effect on the accuracy of the simulation, a small bin size will require more memory. Depending on the memory available, a compromise may be needed to avoid the time-consuming swapping of memory to the hard disk.

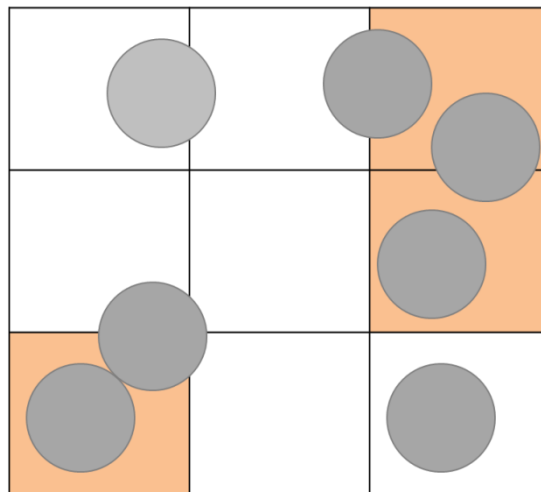


Fig. 2.5. Contact detection using bins (active cells are highlighted).

2.3.2 Particle motion

The DEM calculations alternate between the application of Newton's law of motion and the Hertz-Mindlin force-displacement law at contact points. In this framework, the resultant forces at any time step t are calculated from relative velocities of contacting particles via equation (2.3) for every particle in the assembly. After the forces are updated, new particle accelerations $\mathbf{a}^{t+\Delta t}$ are calculated using Newton's law of motion. New velocities $\mathbf{v}^{t+\Delta t}$ are obtained from numerical integration of $\mathbf{a}^{t+\Delta t}$, and upon further integration, particle displacements are obtained which finally determine the new positions $\mathbf{r}^{t+\Delta t}$ of every particle. With all particle positions and velocities updated, the program then repeats the cycle until the end of the simulation. Stabilization is achieved by applying damping mechanisms on the discrete particles and the system as a whole to dissipate kinetic energy which would otherwise result in indefinite oscillations. The following equations describe the calculations steps of the DEM cycle implementing an explicit numerical scheme:

$$\mathbf{a}^{t+\Delta t} = \frac{\mathbf{F}^t}{m} \quad (2.45)$$

$$\dot{\boldsymbol{\omega}}^{t+\Delta t} = \frac{\mathbf{T}^t}{I}$$

$$\mathbf{v}^{t+\Delta t} = \mathbf{v}^t + \Delta t \cdot \mathbf{a}^{t+\Delta t} \quad (2.46)$$

$$\boldsymbol{\omega}^{t+\Delta t} = \boldsymbol{\omega}^t + \Delta t \cdot \dot{\boldsymbol{\omega}}^{t+\Delta t}$$

$$\mathbf{r}^{t+\Delta t} = \mathbf{r}^t + \Delta t \cdot \mathbf{v}^{t+\Delta t} \quad (2.47)$$

Fig. 2.4 illustrates the calculation cycle. The thermal part of the DEM code is activated when contact between elements is detected and temperature is updated right after contact forces have been calculated (Step 3).

2.3.3 Temperature update

In the thermal part of the DEM code, each particle is a heat reservoir which exchanges heat with neighboring reservoirs via thermal pipes. A thermal pipe between two heat reservoirs is established when the distance between particles centers is less than the sum of their radii (contact detection). Heat transfer across the thermal pipe is controlled by the heat transfer coefficient and a non-physical heat transfer area between two elements.

For two particles i and j in contact, the heat transfer area is defined as

$$A_{pp} = 2\pi \left(\frac{R_i R_j}{R_i + R_j} \right)^2. \quad (2.48)$$

For contact between a particle and a geometry element (wall), we assume that the radius of curvature of the wall is much larger than particle radius, i.e. $R_w \gg R_i$. Hence equation (2.48) is reduced to

$$A_{wp} = 2\pi(R_i)^2. \quad (2.49)$$

It is worth noting that heat transfer area defined in (2.48) and (2.49) is not that same as the contact area from Hertzian contact mechanics which approximates the physical contact area between two surfaces. Rather, A_{pp} and A_{wp} defines the effective heat transfer area to account for gas-solid and solid-solid conduction, and radiation transfers.

The temperature change of particle i in time step Δt due to interaction with particle j is given by

$$\Delta T_i = h_{pp} A_{pp} (T_j - T_i) \frac{\Delta t}{m_i c_i}, \quad (2.50)$$

and the temperature change of particle i in time step Δt due to interaction with wall elements is given by

$$\Delta T_i = h_{wp} A_{wp} (T_w - T_i) \frac{\Delta t}{m_i c_i}, \quad (2.51)$$

where the particle-to-particle heat transfer coefficient h_{pp} and wall-to-particle heat transfer coefficient h_{wp} is related to the wall-to-surface heat transfer coefficient h_{ws} and the packed bed thermal conductivity k_b respectively. Finally, the temperature of particle after one time step Δt is given by

$$T_i^{t+\Delta t} = T_i^t + \Delta T_i. \quad (2.52)$$

In the present work, only particle temperatures are updated. Walls are assumed to be an infinite heat source and are set as an isothermal boundary condition.

2.3.4 Simulation time-step

The amount of time between iterations is chosen to be small such that disturbances cannot propagate from a particle beyond its immediate neighbors (Cundall and Strack, 1979). This condition imposes a restriction that is both geometric and physical; Geometric restriction do not allow two particles to penetrate each other along their central axes during one time step, while physical restriction dictates that momentum

transfer from one body to another in a single time step must not exceed the total momentum exchange during the whole collision process (Tang, 2001).

EDEM implements a fixed time-step which is a fraction of the Rayleigh time t_{Rayleigh} , which is defined as the time taken for Rayleigh waves to propagate through a solid particle. For poly-dispersed particles, the Rayleigh time is based on the smallest particle and is calculated using

$$t_{\text{Rayleigh}} = \frac{\pi R \sqrt{\rho/G}}{0.1631\nu + 0.8766}. \quad (2.53)$$

In the frame of Hertzian contact mechanics, the duration of contact between particles depends on the relative particle velocity, particle mass, particle size, Young's Modulus, and Poisson ratio:

$$t_{\text{Hertz}} = 2.87 \left(\frac{m^*}{v^{\text{rel}} R^* (E^*)^2} \right)^{\frac{1}{5}}. \quad (2.54)$$

While a smaller time-step will increase CPU time, a time-step that is too large will cause excessive virtual overlap during contact which may in turn result in unrealistic particle velocities. Hence, the critical time step Δt_{cr} should be a fraction of t_{Rayleigh} or t_{Hertz} , whichever is smaller, i.e.

$$\Delta t_{\text{cr}} = \kappa \min(t_{\text{Rayleigh}}, t_{\text{Hertz}}) \quad (2.55)$$

where the recommended value of κ is 0.1-0.3 for t_{Rayleigh} or 0.05-0.15 for t_{Hertz} to ensure that the contact is appropriately resolved without excess overlap energy.

Chapter 3

Calibration and Modeling

3.1 Calibration as a necessary step in DEM

Determination of relevant input parameters for DEM is an important step in the simulation of granular flows because bulk behavior is greatly influenced by particle-scale mechanisms. Calibration of DEM parameters is time consuming but critical for the success of the simulation study because a carefully calibrated ‘virtual experiment’ can predict actual dynamic behavior with reasonable degree of accuracy. In most DEM simulations, the representative particles often do not follow actual particle attributes of size and shape. It is possible to model complex shapes in DEM using large numbers of small aggregated spheres or super-quadrics, but at the expense of computational time. It is more economical to represent a particle by a single sphere or an aggregate of a small number of spheres (Grima and Wypych, 2011), coupled with careful calibration of the physical properties of the particle model. This oversimplification is often necessary to reduce computation load. Calibration tunes the simulation parameter so that bulk thermal and flow behavior matches experimental data. Some thought must be put into the selection of calibration parameters so that the calibrated microscopic property is independent of vessel geometry. This allows the same parameter values to be used for larger simulations and avoid the need for validation of the larger systems, which

in most cases is not very feasible. Table 3.1 compares the difference between particles in a practical systems and simulated systems.

Table 3.1. Differences between particles in practical systems and simulated systems.

Practical systems	Simulated systems
Particles have non-uniform properties.	Assume uniform properties to simplify computations.
Particles have complex or irregular shapes.	Usually represented by disks or spheres. Other shapes possible (e.g. super-quadratics, sphere clusters, etc.) but increases computation time.
Particles always exists in large numbers (sand, powder, coal pile, grains, etc.)	Total number of simulated particles are limited by CPU. Computation time is an exponential function of the number of particles simulated.
Particles can have sizes ranging from large pellets, to fine powders	Large particles are easily simulated, but very small particles like powders are usually approximated using larger particles.
Processor vessels are mostly in the meter scales.	Processor vessels are scaled down to a manageable size or symmetry boundary conditions are used to limit the number of particles to be simulated.

3.2 Material selection

This study was motivated by the need to investigate the flow and heat transfer characteristics of coal particles in a screw conveyor heat exchanger. However, the difficulty in obtaining consistent physical and thermal properties of coal granules due its variability (Perry *et al.*, 1984; Smith and Smoot, 1990) calls for a substitution of material. The main consideration for the choice of granular bed material is the availability of relevant heat transfer for use in the calibration of the simulated particle bed.

Wunschmann and Schlunder (1974) conducted several experimental heat transfer studies of packed and stirred bed heating of several materials including glass, polystyrene, and bronze (Table 3.2). Out of these materials, bronze was immediately eliminated from the selection due to its high heat conductivity, which is quite the opposite of coal. Between polystyrene and glass, the former is more representative of coal based on density alone. However, the largest polystyrene particle studied was still too small given the amount of time available for the simulation study. Hence, 3.1 mm glass bead was selected as granular bed material to reduce the number simulated particles and computation time to a more manageable level.

Table 3.2. Properties of granular bed material (Wunschmann and Schlunder, 1974).

Material	d mm	ρ_p kg m ⁻³	ρ_{bed} kg m ⁻³	k_p W m ⁻¹ K ⁻¹	c_p J kg ⁻¹ K ⁻¹
Glass	3.1, 2.1, 1.0, 0.5, 0.25	3000	1800	0.93	633
Polystyrene	1.05, 0.60	1050	630	0.174	1255
Bronze	0.94, 0.50	8600	5150	46.1	377

This of course questions the validity of the study since glass is very different from the original material of interest, which is coal. From this viewpoint, the answer is of course negative. However, if one were to view this study as primarily an evaluation of the performance of the screw conveyor heat exchanger, then the choice of bed material is rendered to secondary importance. Another reason for choosing glass is the availability of heat transfer data for various sizes as shown in Table 3.2. This information allows one to calibrate the glass particles for different sizes so that a study on the effect of particle

size on the performance of the heat exchanger can be conducted. Due to limited time and resources, this parametric effect will not be studied in the current work.

3.3 Calibration of bulk flow

There are various methods to determine the simulated bulk properties of a particular material, all of which involve systematic adjustments of flowability indicators such as coefficient of restitution (CoR), rolling and static frictions, tensile strength, bulk compressibility etc. (Grima and Wypych, 2009). To perform the calibration, a series of bench-scale tests using the material to be simulated is needed. The work of Li *et al.* (2005), which resolves the angle of repose for various materials using conical piling tests, provided the experimental aspect required for our calibration. By repeating the same procedure described by Li *et al.* (2005), but in a ‘virtual’ environment that is DEM, a set of parameter values describing the simulated material and its interactions was obtained (see Table 3.3). Fig. 3.1 illustrates the close resemblance between conical pile obtained from real experiment and DEM.

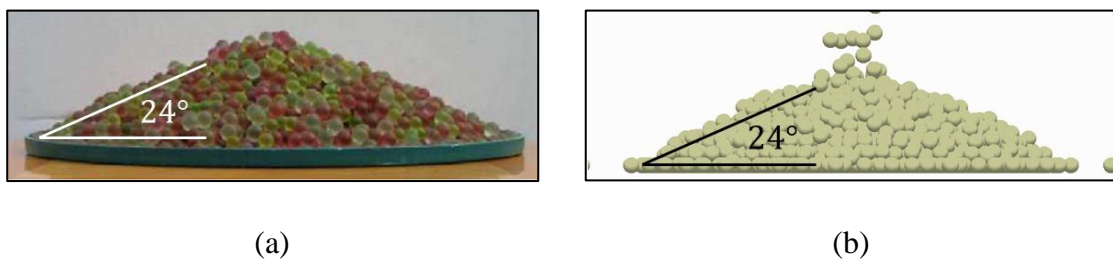


Fig. 3.1. Conical pile obtained from (a) experiment (Li *et al.*, 2005) and (b) DEM.

Table 3.3. Calibrated properties of glass bed and copper wall.

Parameter	Value
Particle (glass)	
Diameter, mm	3.1
Density, kg m ⁻³	3000
Poisson's ratio	0.25
Shear modulus, Pa	2.20×10^6
Wall (copper)	
Density, kg m ⁻³	8900
Poisson's ratio	0.25
Shear modulus, Pa	7.72×10^{10}
Interactions	
P-P Coefficient of restitution	0.80
P-P Coefficient of friction (static)	0.40
P-P Coefficient of friction (rolling)	0.15
P-W Coefficient of restitution	0.60
P-W Coefficient of friction (static)	0.70
P-W Coefficient of friction (rolling)	0.13

3.4 Calibration of heat transfer coefficients

3.4.1 Application of the penetration model

Kwapinska *et al.* (2008) was the first to show that thermal DEM and penetration model (PM) converge to the same asymptotic behaviour in case of heat transfer controlled by a contact resistance at the heated wall. For the heat transfer calibration exercise, heating of a cylindrical packed bed via a circular flat plate was simulated. The simulation domain is an open cylindrical drum with a circular flat plate which is isothermal at 373 K. The simulation was set such that heat transfer between the particles

and curved surface of the drum is neglected. Details of calibration parameters are listed in Table 3.4.

Table 3.4. Parameters for heat transfer calibration.

Parameter	Symbol	Unit	Value
Particle mass	m	kg	0.133
Particle heat capacity	c	J kg ⁻¹ K ⁻¹	633
Plate temperature	T_w	K	373
Initial bulk temperature	T_{b0}	K	298
Bulk density	ρ_{bed}	kg m ⁻³	1468
Heat transfer area	A_{ht}	m ²	1.81×10^{-3}

3.4.2 Wall-to-particle heat transfer

The wall-to-surface heat transfer coefficient h_{ws} for a bed of spherical particles of any size can be calculated using Schlunder's (1984) correlation via Equations (2.24) to (2.29) in both ambient and vacuum conditions. Parameters used in the calculation of h_{ws} using Schlunder's correlation are listed in Table 3.5. The results are plotted in Fig. 3.2 which shows that particle size has very little influence on h_{ws} when in vacuum but has significant effect on h_{ws} at atmospheric pressure. Therefore, parameter values that are obtained from this calibration exercise will only be valid for 3.1 mm glass spheres. Recalibration is required if other sizes or material is used. For packed bed made up of 3.1 mm glass spheres, $h_{ws} = 248 \text{ W m}^{-2} \text{ K}^{-2}$. Having said that, it is now necessary to find a relationship between the continuum parameter h_{ws} and the discrete parameter h_{wp} . To do this, the simulation was set to the contact-controlled regime whereby the overall heat

transfer coefficient is determined by the wall-surface h_{ws} heat transfer coefficient. This is established by applying an arbitrarily high value to particle-particle heat transfer coefficient h_{pp} so that heat transfer from flat plate to packed bed is controlled by the wall-to-particle heat transfer coefficient h_{wp} . This condition was imposed by setting $h_{pp} = 10^5 \text{ W m}^{-2} \text{ K}^{-1}$ and then varying h_{wp} between 100 and 1000 $\text{W m}^{-2} \text{ K}^{-1}$.

Table 3.5. Parameters for calculation of h_{ws} using Schlunder's correlation (1984).

Parameter	Symbol	Unit	Value
Particle conductivity	k_p	$\text{W m}^{-1} \text{ K}^{-1}$	0.93
Gas conductivity	k_g	$\text{W m}^{-1} \text{ K}^{-1}$	0.027
Gas viscosity	μ_g	Pa s	1.9×10^{-5}
Gas molar mass	\mathcal{M}	kg mol^{-1}	2.89×10^{-2}
Accommodation coefficient	ϕ_A	-	0.9
Wall coverage factor	ϕ_w	-	0.85
Wall emissivity	ϵ_w	-	0.9
Bed emissivity	ϵ_B	-	0.9
Dia. contact area/Particle dia.	a/d	-	3.0×10^{-4}
Surface roughness	α	-	0
Pressure	p	Pa	10^5
Gas constant	R_G	$\text{J K}^{-1} \text{ mol}^{-1}$	8.314
Stefan-Boltzmann constant	σ	$\text{W m}^{-2} \text{ K}^{-4}$	5.67×10^{-8}

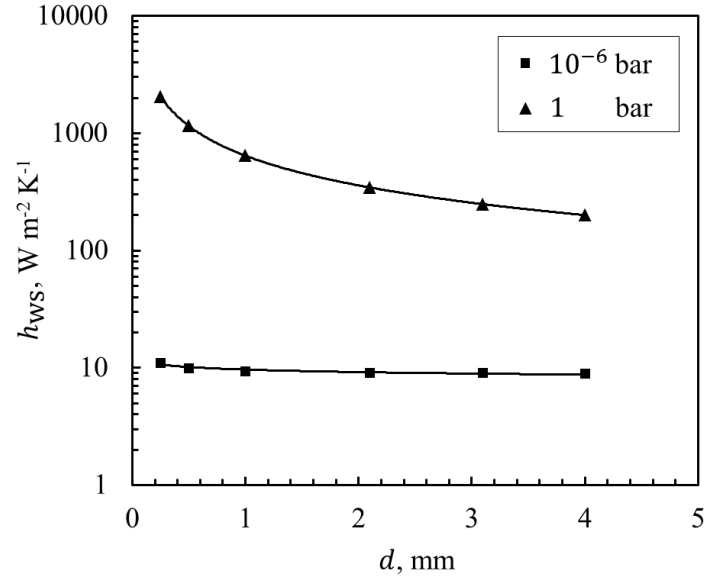


Fig. 3.2. h_{ws} vs. d for packed bed of glass spheres at atmospheric pressure and vacuum.

The contact-controlled regime is clearly illustrated in Fig. 3.3 which shows the absence of temperature gradient in the granular bed. The heating curve for each h_{wp} is plotted (see Fig. 3.4) and fitted by Equation (2.43) to obtain h_{ws} (Kwapinska *et al.*, 2008). A relationship between continuum and discrete parameters was established by plotting a graph of h_{ws} vs h_{wp} (see Fig. 3.5). The relationship was found to be linear and can be expressed as:

$$h_{ws} = 1.234h_{wp} + 16.945 \quad (3.1)$$

Substituting $h_{ws} = 248 W m^{-2} K^{-2}$ into equation (3.1), we obtain $h_{wp} = 187 W m^{-2} K^{-2}$.

h_{wp} is a critical parameter in the DEM simulation as it specifies the amount of heat to be transferred when a simulated particle gets in contact with a heated wall.

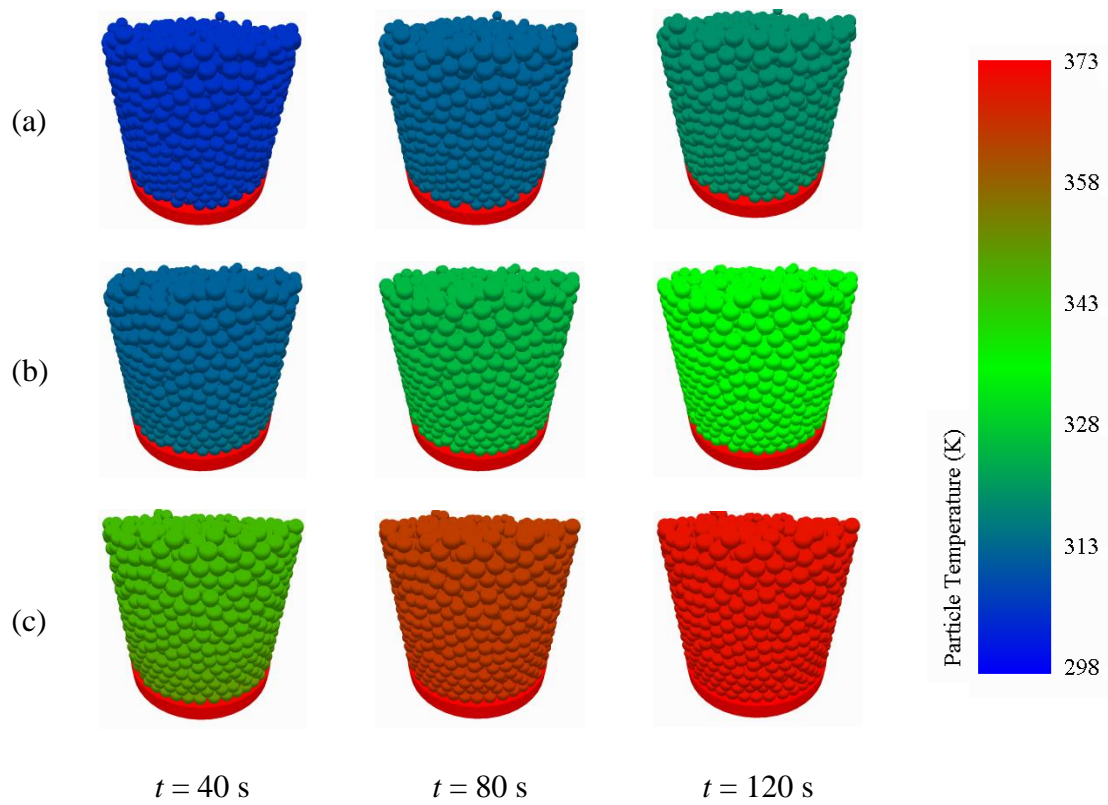


Fig. 3.3. Evolution of bed temperature for contact-controlled regime where $h_{pp} = 10^5 \text{ W m}^{-2} \text{ K}^{-1}$, and h_{wp} are varied: (a) 100, (b) 200, and (c) $1000 \text{ W m}^{-2} \text{ K}^{-1}$.

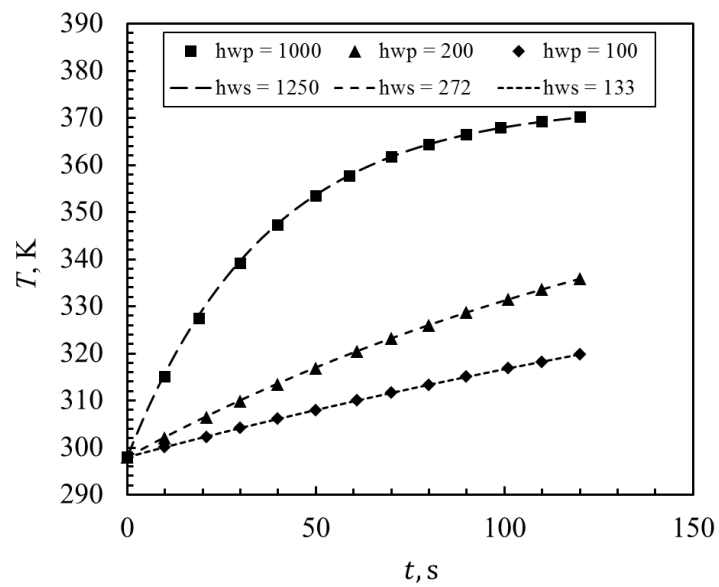


Fig. 3.4. Heating curve for packed bed heating in contact-controlled regime.

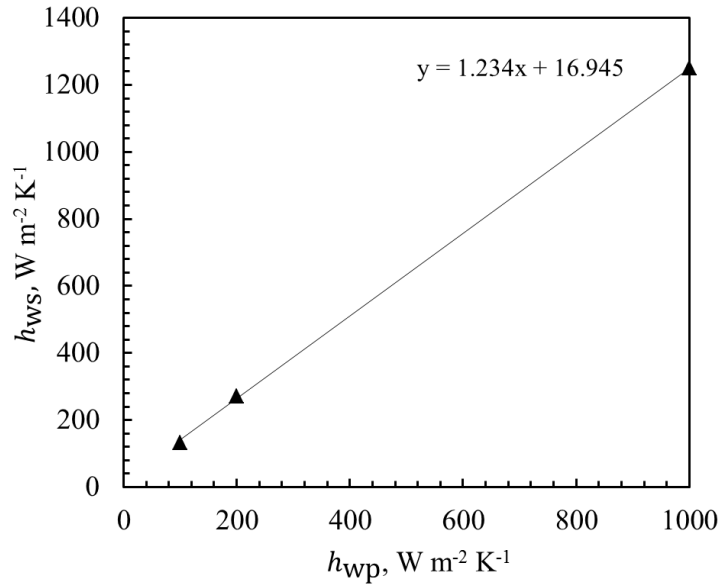


Fig. 3.5. Correlation between h_{ws} (PM) and h_{wp} (DEM).

3.4.3 Particle-to-particle heat transfer

The equivalence between PM and thermal DEM is established by carrying out simulations for penetration-controlled regime. This is done by setting an arbitrary high value for h_{wp} so that the overall heat transfer coefficient is now limited by h_{pp} . It is important to note that while equivalence between continuum model and discrete model for heat transfer between heated surface and first particle layer is established via h_{ws} and h_{wp} , equivalence between PM and discrete models for heat penetration through the bed will be established via bed conductivity k_b and particle-particle heat transfer coefficient h_{pp} . Using the same simulation domain as before and setting $h_{wp} = 10^5 W m^{-2} K^{-1}$, h_{pp} is then varied between 10 and 100 $W m^{-2} K^{-1}$. The simulation was run for 600 seconds for each case and resulting heating curve was converted to h vs t curve. Fig. 3.7 shows the

evolution of bed temperature for penetration-controlled case where steep temperature gradient is observed for low h_{pp} .

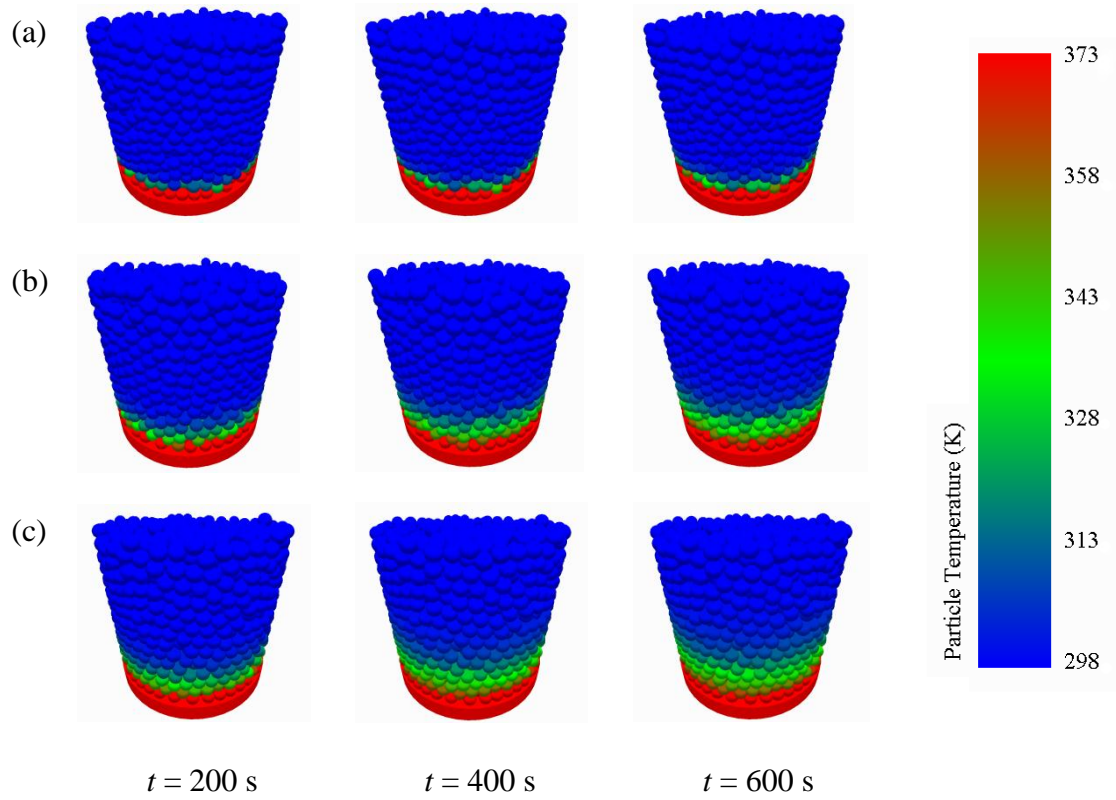


Fig. 3.6. Evolution of bed temperature for penetration-controlled regime where $h_{wp} = 10^5$ $\text{W m}^{-2} \text{K}^{-1}$, and h_{pp} are varied: (a) 10, (b) 50, and (c) 100 $\text{W m}^{-2} \text{K}^{-1}$.

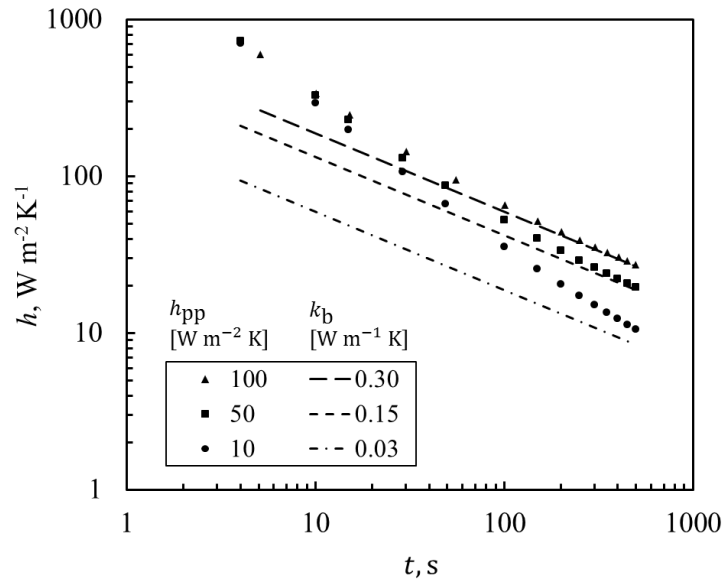


Fig. 3.7. Evolution of h for packed bed heating in penetration-controlled regime.

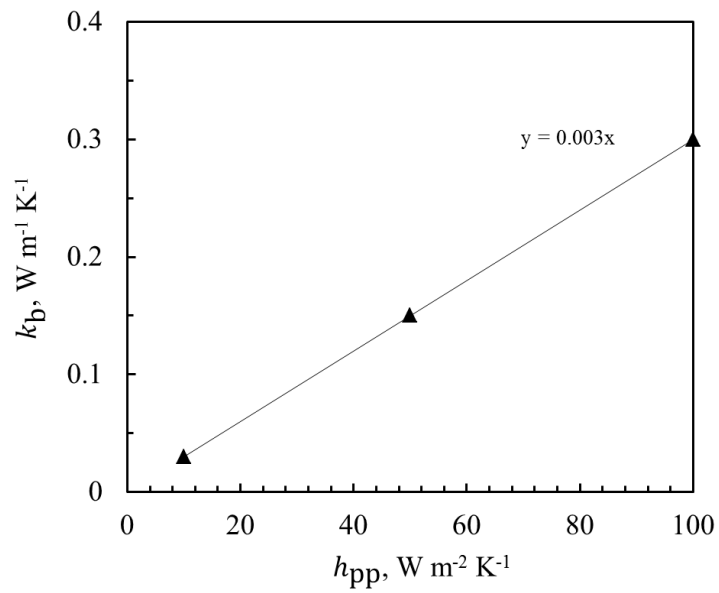


Fig. 3.8. Correlation between h_{pp} (DEM) and k_b (PM).

The equivalence between PM and thermal DEM can be seen in Fig. 3.7 where h from DEM approaches the PM asymptote—which is calculated using equation (2.33)—at long

heating times. A relationship between k_b and h_{pp} was thus established and the correlation was found to be linear (see Fig. 3.8):

$$k_b = 0.003h_{pp} \quad (3.2)$$

For a packed bed of 3.1 mm glass spheres, Wunschmann and Schlunder (1974) showed that $k_b = 0.18 \text{ W m}^{-1} \text{ K}^{-1}$. Substituting this value into equation (3.2), we obtain $h_{pp} = 60 \text{ W m}^{-2} \text{ K}^{-1}$. To validate the calibration exercise, heat transfer curve from the DEM simulation is plotted against experimental results from Wunschmann and Schlunder (1974). As shown in Fig. 3.9, Both DEM and experimental results for packed bed approaches the same asymptote, thus validating and concluding the calibration exercise.

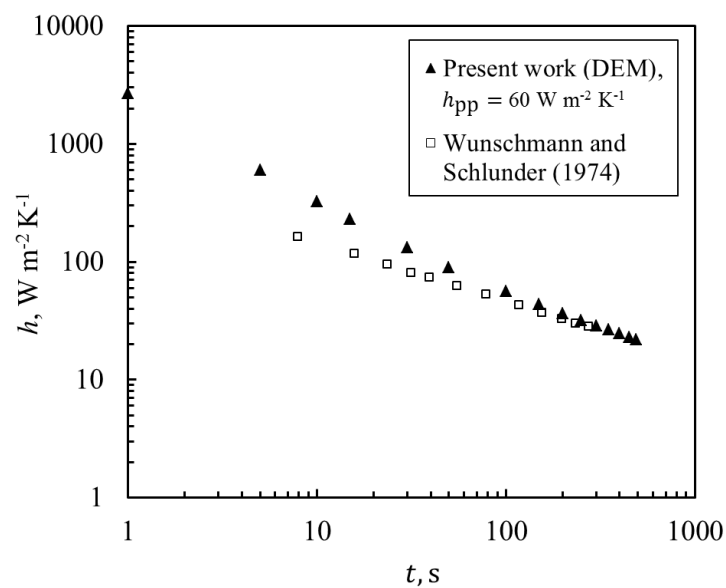


Fig. 3.9. Validation of calibration exercise.

3.5 Modeling of screw conveyor heater

3.5.1 Model parameters and numerics

A screw conveyor with housing diameter of 8.2 cm, screw diameter of 8 cm, and shaft diameter of 2 cm was constructed using a Computer-aided Design (CAD) software (Solidworks, Dassault Systemes) and imported into a discrete element simulation package (EDEM, DEM Solutions) as geometry elements for the granular flow and heat transfer 'virtual experiments'. To allow the parametric computations to be completed within a reasonable time, the simulation domain is limited to a 32 cm long screw conveyor with four full turns for the base-case screw geometry (pitch-to-diameter ratio P/D of 1.0). The narrow clearance of 1 mm between the screw and its housing prevent the build-up of stationary particles in the conveying region.

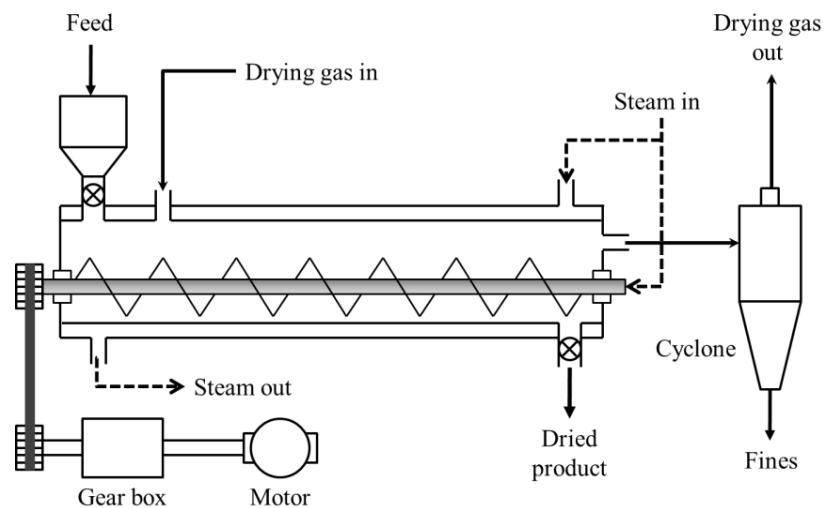


Fig. 3.10. Screw conveyor dryer system.

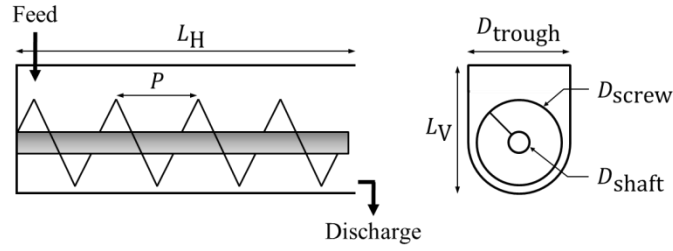


Fig. 3.11. Computational domain of DEM simulations.

The screw conveyor heat exchanger geometry domain comprises of a screw in concentric arrangement with the u-trough. The temperature of the screw (blade and shaft) and the u-trough is constant at $T_w = 373$ K to simulate heat supply by continuous stream of steam in the jacket and screw conduit. Uniformly-sized particles of initial temperature $T_{p,0} = 298$ K enter the heat exchanger in the upstream region at a fixed rate M_G . Heat transfer occurs when there is temperature difference between a particle and another particle or wall surface it is in contact with. Heat transfer due to contact with the endplate is neglected with the assumption that the endplate is always at the same temperature as the immediate bed layer. In view of the highly truncated screw conveyor geometry, the longitudinal dimension of the solid feed area is made as small as possible to ensure that particles enter the domain with minimum dispersion (at $t = 0$ s). Degree of fullness was kept below 0.45 for all cases, conforming to earlier studies (Waje *et al.*, 2006).

The particle density is $\rho_p = 3000$ kg m⁻³. Particle volume fraction ϕ_F was determined via DEM by random-filling a 1 m³ cubic container with glass spheres and then measuring the total particle mass. The bulk density was evaluated as $\rho_b = 1467$ kg m⁻³, corresponding to $\phi_F = 0.49$ which underestimated experimental results by a narrow margin (Song *et al.*, 2008). This is attributed to the slight overlapping between

particles as a consequence of setting shear modulus to a low value. This however, has negligible effect on the overall flow and heat transfer characteristics. The specific heat capacity of the glass particles corresponds to that of glass with $c_p = 633 \text{ J kg}^{-1} \text{ K}^{-1}$ while the screw conveyor geometry adopted the thermal characteristics of (Schlunder, 1984). This thesis follows from Kwapinska (2008) argument that since h_{pp} and h_{wp} are treated as free parameters, specifying the thermal conductivity of the particles and the kind of gas filling the gaps of the bed are not necessary. Here, we use $h_{pp} = 60 \text{ W m}^{-2} \text{ K}^{-1}$ and $h_{wp} = 187 \text{ W m}^{-2} \text{ K}^{-1}$, the derivation of which has been shown in the preceding sections. All simulations were performed with a constant mechanical and thermal time step of $2.0 \times 10^{-6} \text{ s}$ using a commercial discrete element modeling software, namely EDEM by DEM Solutions. Calculations have been conducted on a 64-bit workstation powered by 12-core Intel Xeon X5690 at 3.47 GHz and 72 GB RAM.

Table 3.6. Parameters for screw conveyor heater.

	Units	Value
Conveyor		
D_{screw}	mm	80
D_{shaft}	mm	20
L_{H}	mm	32
P	mm	Refer to Table 3.7
D_{trough}	mm	82
L_{V}	mm	100
Feed window	mm x mm	80 x 20
Density	kg m^{-3}	8900

3.5.2 Granular flow and heat transfer simulation

The quantitative analysis of flow and heat transfer of granular materials in a screw conveyor heat exchanger configuration is reduced to two important particle-level parameters namely residence time and temperature. Residence time data is obtained directly from a particle-level property called ‘residence time’ which is essentially a time-stamp which begins and stops when a particle enters and exits the heat exchanger domain. The residence time data can then be post-processed to give a probability density function (E-curve) or cumulative distribution function (F-curve) after which parameters such as holdback, segregation, mean residence time (MRT), residence time standard deviation, etc. can be calculated to quantify flow and mixing properties of the processor with respect to the material being processed. Similarly, the evolving temperature of a particle is captured at every time-step of the simulation via a user-defined parameter ‘temperature’.

3.5.3 Parametric study

The performance of the screw conveyor was determined in terms of residence time distribution, mean residence time, extent of mixing, granular temperature distribution, and the overall heat transfer coefficient. The performance characteristics of the screw conveyor were investigated as a function of solids flow rate M_G , screw speed N , angle of inclination θ , and pitch-to-diameter ratio P/D . Table 3.7 lists the specifications for each case of the parametric study. The reference case is specified on the second row of the table and is based on a series of trial simulations to carried out to

obtain N for which $M_G = 150 \text{ kg h}^{-1}$ and degree of fullness $\beta = 0.3$ are simultaneously satisfied for standard screw configuration (i.e. $P/D = 1$ and $\theta = 0$). The selected reference value of M_G is a design requirement. It was also shown elsewhere (Waje et al) that $\beta = 0.3$ is appropriate for screw conveyors handling Class II materials which include coal particles. Although the interest is in coal, the particles in the simulations are modeled after glass. In terms of flow through the screw conveyor, it is assumed that its principal characteristics are similar regardless of material used.

Table 3.7. Case specifications for parametric study of screw conveyor heater.

Case	M_G , kg h ⁻¹	N , rpm	θ , degrees	P/D
Base	150	11	0	1.00
A1	15	11	0	1.00
A2	30	11	0	1.00
A3	50	11	0	1.00
A4	75	11	0	1.00
A5	100	11	0	1.00
A6	175	11	0	1.00
A7	200	11	0	1.00
B1	150	7	0	1.00
B2	150	15	0	1.00
B3	150	19	0	1.00
C1	150	11	5	1.00
C2	150	11	10	1.00
C3	150	11	15	1.00
D1	150	15	0	0.75
D2	150	23	0	0.50
D3	150	50	0	0.25

The shaded boxes in Table 3.7 distinguish the parameters being studied from other parameters. Cases A1-A6, B1-B3, and C1-C3 focuses on the influence of solid flow rate, screw speed, and inclination angle of screw respectively while cases D1-D3 investigate the effect of the geometrical parameter P/D (see Fig. 3.12). For cases A, B, and C, parameters that are under investigation are varied while other parameters are kept at reference value whereas for cases D, only solid flow rate and degree of fullness are kept constant. This imposes angular screw speeds which follow (Waje *et al.*, 2006):

$$\frac{M_G}{\rho_b} = \beta \frac{\pi}{4} [(D_{sc} + \delta_r)^2 - D_{sh}^2] (P - \delta_t) (N \times 60) \quad (3.3)$$

The above equation is used to produce Fig. 3.13 which shows the relation between degree of fullness β and screw speed for different solid flow rates, and also the relation between solid flow rate and screw speed for different pitch-to-diameter ratios. It is clear that the study of parameter P/D must correspond with appropriate values of N for a particular M_G to ensure that β remain constant; otherwise the conveyor will be flooded and result in a stalled simulation. Hence, for $M_G = 150 \text{ kg h}^{-1}$ and $\beta = 0.3$, the appropriate screw speeds for $P/D = 1, 0.75, 0.5,$ and 0.25 are $N = 11, 15, 23,$ and 50 and 11 rpm respectively. Fig. 3.13 will be useful later when we validate the DEM results.

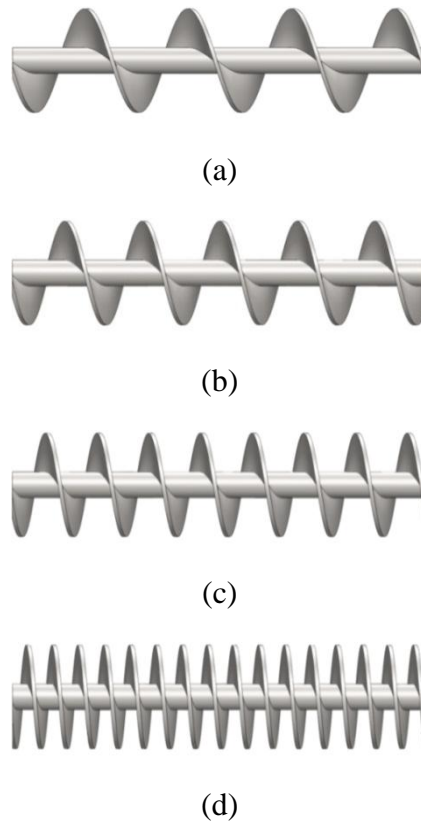


Fig. 3.12. Screw configurations for pitch-to-diameter ratio study: $P/D =$ (a) 1.00, (b) 0.75, (c) 0.50, and (d) 0.25.

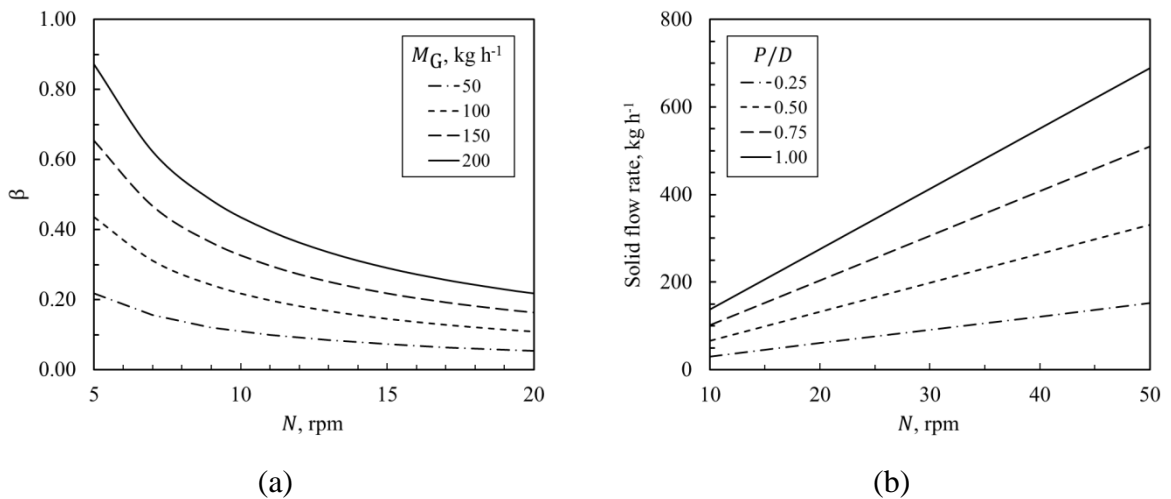


Fig. 3.13. Theoretical relationships between screw conveyor parameters: (a) degree of fullness vs. screw speed for different solid flow rates; (b) solid flow rate vs. screw speed for different pitch-to-diameter ratios.

3.6 Data analysis

3.6.1 Volume and surface area of screw conveyor domain

The screw conveyor geometry is relatively complex but determining certain geometrical parameters specifically surface area and volume is quite straight forward for a basic screw configuration. One can imagine the screw as an assembly of many annular flat plates that are welded from end-to-end and then stretched into a spiral along a central shaft. The degree to which the plates are bent due to stretching determine the screw pitch P , span D_{screw} , and shaft diameter D_{shaft} , which in turn must be some function of the annular plate dimensions $D_{\text{I,plate}}$ and $D_{\text{O,plate}}$ (for inner and outer diameter respectively). The length of the outer blade edge L_{blade} of the screw can be expressed in terms of P and D_{screw} as

$$L_{\text{blade}} = \sqrt{P^2 + (\pi D_{\text{screw}})^2}. \quad (3.4)$$

At the same time, L_{blade} is also equal to the outer circumference of the annular flat plate from which the screw is assembled, i.e.

$$L_{\text{blade}} = \pi D_{\text{O,plate}}. \quad (3.5)$$

Combining equations (3.4) and (3.5), and using the same argument for the inner blade edge, the annular flat plate dimensions can be expressed in terms of screw dimensions as shown in the following equations:

$$D_{0,plate} = \frac{\sqrt{(\pi D_{screw})^2 + P^2}}{\pi} \quad (3.6)$$

$$D_{I,plate} = \frac{\sqrt{(\pi D_{shaft})^2 + P^2}}{\pi}. \quad (3.7)$$

The volume occupied by the screw is then

$$V_{screw} = \frac{\pi N_{turns}}{4} \left[\delta_{plate} (D_{0,plate})^2 - \delta_{plate} (D_{I,plate})^2 + P (D_{shaft})^2 \right] \quad (3.8)$$

where N_{turns} is the number of turns in the screw section of interest, and δ_{plate} is the thickness of the plate. If the screw and u-trough are concentric, and there is minimal clearance between screw blades and u-trough surface, then the u-trough volume for the same screw section is defined as

$$V_{trough} = N_{turns} P \left[\frac{\pi}{8} (D_{screw})^2 + \frac{1}{2} (D_{screw})^2 \right]. \quad (3.9)$$

3.6.2 Degree of fullness

The degree of fullness β is defined as the ratio of volume occupied by the particles in the screw conveyor (M_H/ρ_p) to the effective volume of the screw conveyor.

The effective volume is the volume of the trough less the volume occupied by the screw.

Therefore,

$$\beta = \frac{M_H}{\rho_p \times V_{eff}} \quad (3.10)$$

where

$$V_{\text{eff}} = V_{\text{trough}} - V_{\text{screw}}. \quad (3.11)$$

In this thesis, trough volume V_{trough} is defined as the volume of a circular trough of the same diameter and length as the u-trough. This simplifies complications without compromising the objectives of this study.

3.6.3 Determination of residence time distribution (RTD)

Experimentally, RTD can be determined by injecting inert tracer particles into the feed stream at some time after steady flow has been achieved and then measuring the tracer concentration in the exit stream as a function of time. Pulse and step inputs are the two commonly used methods of injection. In pulse input method, an amount of tracer material is inserted in one shot into the feed stream over a time interval much smaller than the mean residence time of the vessel. The residence time distribution function (also called the exit age distribution) $E(\tau)$ is defined in terms of the effluent concentration-time curve $C(\tau)$ according to:

$$E(\tau) = \frac{C(\tau)}{\int_0^{\infty} C(\tau) dt} \quad (3.12)$$

In the step input method, the concentration of the tracer changes abruptly from 0 to C_0 . The concentration of the tracer in the feed is kept at this level until the concentration in the effluent is indistinguishable from that in the feed, after which the test may then be discontinued. The output concentration-time curve is normalized to give the $F(t)$ curve defined as

$$F(\tau) = \frac{C(\tau)}{C_0} = \int_0^t E(\tau) dt \quad (3.13)$$

This is easily achieved using DEM which enables very precise control over tracer particle introduction at the inlet stream, and highly consistent and accurate measurement of tracer particles concentration at the outlet stream. Determination of the RTD involves injection of a one-second pulse input of ‘tracer’ particles immediately following steady-state condition. The tracer particles are identical to the bulk particles in every aspect except for color, which is superficially applied to differentiate between bulk and tracer. To ensure that the steady-state condition is not disturbed, feeding of bulk particles is momentarily stopped during tracer injection. Feed rate is kept constant throughout the whole procedure. Because the simulation involves a relatively short screw conveyor, the dimension of the particle feed area in the axial direction must be small compared to the overall length of the screw to minimize error. RTD is obtained by sampling for the number of tracer particles appearing at the outlet at time.

3.6.4 Heat transfer coefficient

The screw conveyor heater overall heat transfer coefficient is calculated using the following equation ((Waje *et al.*, 2006)):

$$h = \frac{Q}{A_{ht} T_{LMTD}} , \quad (3.14)$$

where Q is given by

$$Q = \frac{M_G}{3600} c_p (T_{bed,f} - T_{bed,i}) . \quad (3.15)$$

In this study evaporation of moisture has been neglected thus Q accounts for sensible heat only. Assuming isothermal wall temperature at 373 K, T_{LMTD} is defined as

$$T_{\text{LMTD}} = \frac{(373 - T_{\text{bed},i}) - (373 - T_{\text{bed},f})}{\ln[(373 - T_{\text{bed},i})/(373 - T_{\text{bed},f})]} \quad (3.16)$$

Chapter 4

Granular Flow Characteristics

4.1 Introduction

The basic screw conveyor configuration has geometrical parameters (pitch, shaft diameter, screw diameter, etc.) that do not vary along the length of the screw, and is not a hybrid of any other rotating devices or mixers. In this chapter, the effect of screw speed, solid flow rate, inclination angle of screw, screw pitch-diameter ratio (P/D), and solid density, on the performance of the screw conveyor were investigated. The performance characteristics of the screw conveyor heater is studied in terms of residence time distribution, hold-back, segregation, and qualitative observations of mixing dynamics along the screw heat exchanger as well as at the discharge.

4.2 Hold-up

Material hold-up M_H is defined as the steady state mass of solid in the screw conveyor heat exchanger. Experimentally, this is determined by continuously feeding and discharging solids until steady state, after which the feed valve is sealed while the conveyor discharges the most of the solids in the vessel. The total mass of the solids collected at the outlet when no more material is discharged (empty vessel except for materials in dead spaces) is the hold-up. In the DEM simulations, hold-up is

approximated by taking the average of mass in the second and third sections (see Fig. 4.1) of the simulated four-pitch screw, and then multiplying the result by four. It is to be noted that the sections are fixed zones of the screw conveyor domain which do not follow forward motion of the screw blades, and are created for calculation purposes only.

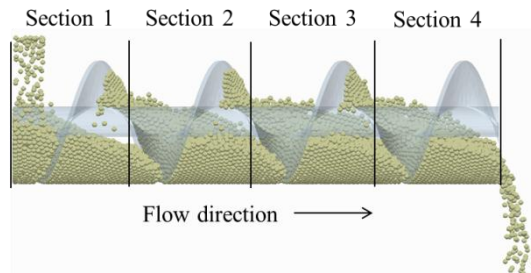


Fig. 4.1. Binning the screw conveyor domain for flow analysis.

The reason for calculating hold-up in this manner is that material mass in the second and third sections encounter the least disturbances compared to the first and last sections which are periodically disturbed by feeding and discharging respectively. For the basic screw conveyor (i.e. those with constant dimensions) with N_t turns of screw blades, sections 2, 3, 4 up to section $n_t - 1$ will have approximately the same mass of solids; whereas mass in the sections at the two ends of the conveyor (section 1 and section n_t) tend to deviate from that of other sections of the screw conveyor domain. This is clearly seen in Fig. 4.2 which shows the mass of solids with respect to time in each section of a $n_t = 4$ screw conveyor for the base case simulation. Periodic fluctuation of mass is evident in Sections 1 and 4, and is characteristic of screw conveyors. Average mass of solids in one section for different solid flow rates, screw speed, angle of inclination, and pitch-to-diameter ratio, are illustrated in Fig. 4.3. It is clear that at screw speed of 11 rpm, the flows becomes steady in less than 50 seconds for

solid flow rates between 15 to 175 kg h⁻¹ but require more time to stabilize at higher flow rates (see Fig. 4.3a). At flow rate of 150 kg h⁻¹, flow stabilizes in less than 30 seconds for screw speeds between 11 to 19 rpm but took more than 160 seconds for screw speed of 7 rpm (see Fig. 4.3b). Stabilization of flow also require more time at greater angles of inclination (see Fig. 4.3c).

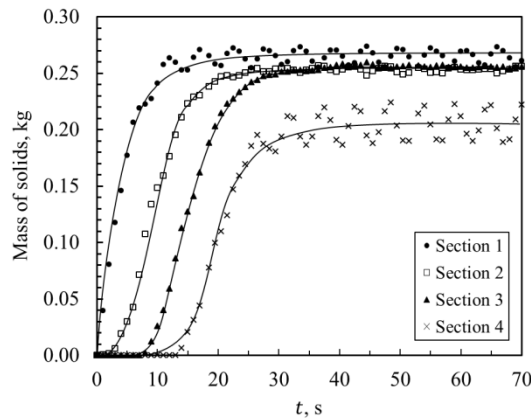


Fig. 4.2. Mass of solids in each section of the screw conveyor domain for base case ($M_G = 150 \text{ kg h}^{-1}$, $N = 11 \text{ rpm}$, $P/D = 1.0$).

Fig. 4.3a and Fig. 4.3b show that solid hold-up is proportional to solid flow rate and inversely proportional to screw speed. The effect of throughput and screw speed on hold-up is intuitive, and requires no further explanation. Inclination increases the occurrence of granular backflow, resulting in the build-up of solids in the low-elevation feed region. Increasing the angle of inclination causes the particles to roll backwards due to of gravity, thereby increasing the hold-up.

Earlier, it was mentioned that the screw conveyor domain for a 4-pitch screw ($P/D = 1.0$) is divided into 4 sections. Similarly, we divide the screw conveyor domain into 5, 8, and 16 sections for $P/D = 0.75$, 0.50, and 0.25 respectively. It is observed that the mass of solids in one section for $P/D = 0.75$ and 0.50 are approximately equal to

mass of solids in one section of $P/D = 1.00$ (Base case) after factoring by the reciprocal of 0.75 and 0.50 respectively. Interestingly, case $P/D = 0.25$ do not follow the same trend. Instead, the solid hold-up for case $P/D = 0.25$ is lower than expected, which is a deviation from theory.

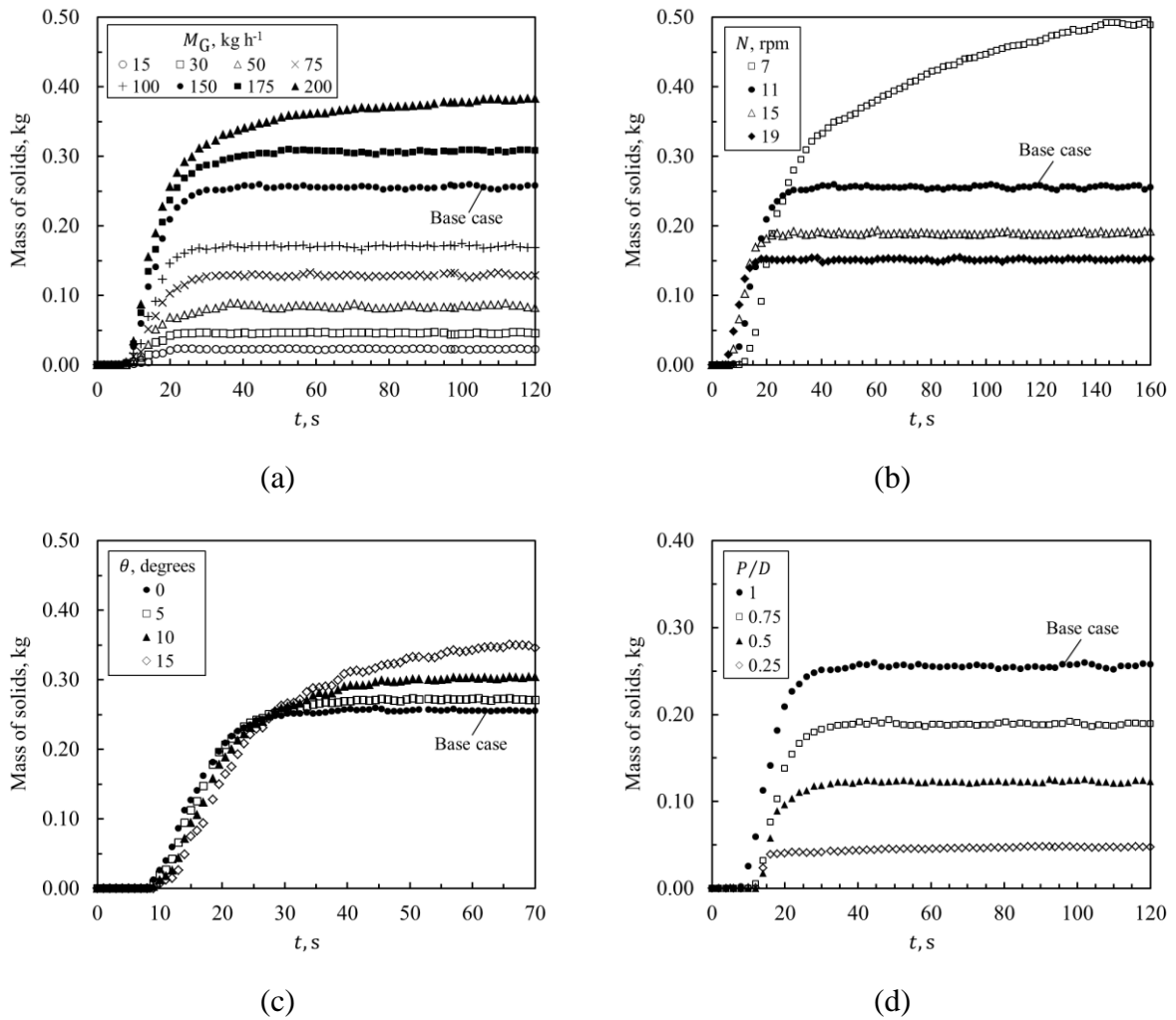


Fig. 4.3. Average mass of solids in one section of the screw conveyor domain for various cases: (a) solid flow rates ($N = 11$ rpm, $P/D = 1.0$), (b) screw speed ($M_G = 150$ kg h⁻¹, $P/D = 1.0$), (c) angle of inclination ($M_G = 150$ kg h⁻¹, $N = 11$ rpm), and (d) pitch-to-diameter ratio ($M_G = 150$ kg h⁻¹, $N = 11$ rpm).

4.3 Degree of Fullness as a validation parameter

A number of methods have been suggested for the validation of DEM results, most of which are qualitative in nature. In this study, degree of fullness obtained from DEM is compared to theory via equation (3.10). This comparison is illustrated in Fig. 4.4 which shows excellent agreement between theory and DEM for $N = 11$ rpm and $15 \leq M_G \leq 150 \text{ kg h}^{-1}$, with increasing deviation from theory at flow rates above 150 kg h^{-1} . Similarly, screw speeds between 11 and 19 rpm are in best agreement with theory for $M_G = 150 \text{ kg h}^{-1}$ but deviate significantly at low N . These results show that a reasonably good prediction of granular flow is limited to degree of fullness β not exceeding 0.4, for any combination of feed rate and screw speed. One reason for this deviation is that the computation of β from equation (3.10) assumes that the trough is circular, whereas we use u-trough for the simulations. From geometric analysis of the u-trough, it can be shown that equation (3.10) can still be applied to the u-trough provided $0 < \beta < 0.5$. For a feed rate of 150 kg h^{-1} , this condition is satisfied in the range of $11 \leq N \leq 19$.

Equation (3.10) is valid only for horizontal screws where gravity has little influence on the axial flow of the particles. Thus, for angle of inclination $\theta > 0^\circ$, β increasingly depart from the horizontal conveyor case (see Fig. 4.5a) due to increased gravity-driven backflow which leads to build-up of particles. As shown in Fig. 4.5b, DEM-derived β is also in excellent agreement with theory for the range of pitch-to-diameter studied with the exception of $P/D = 0.25$. Noting from earlier an observation that β begins to depart from theory occur when $\beta > 0.3$ (see Fig. 4.5a), the result of Fig. 4.5b seem peculiar since $\beta \leq 0.3$ for all cases. It must be that there exists a

‘critical’ screw speed N_{crit} above which DEM result will deviate from theory. It is understood that N_{crit} depend on several factors including (but not limited to) degree of fullness, pitch-to-diameter ratio, and contact properties between particle and vessel geometry.

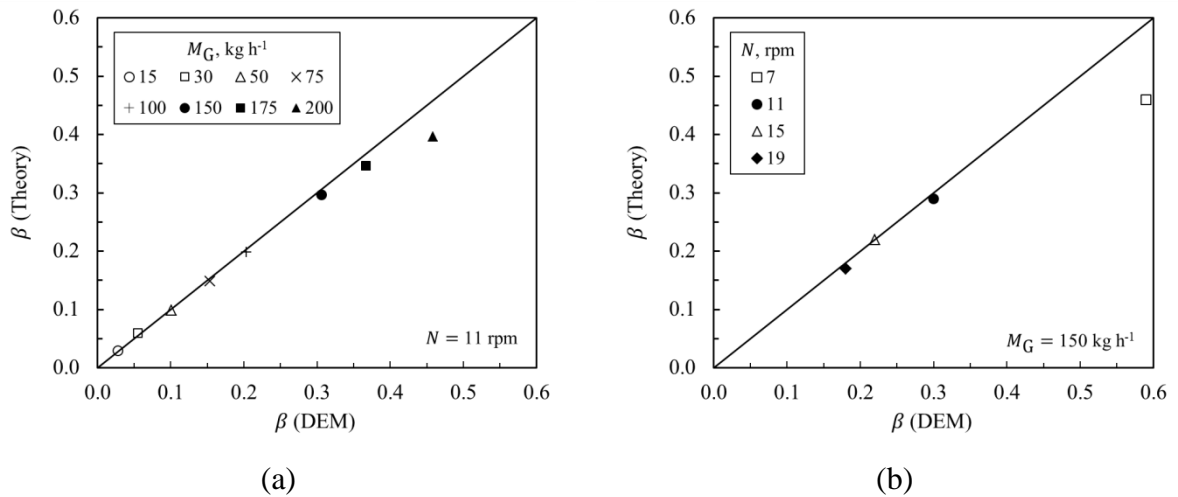


Fig. 4.4. Theoretical vs. DEM prediction of β for different (a) M_G and (b) N . ($\theta = 0^\circ$, $P/D = 1.0$)

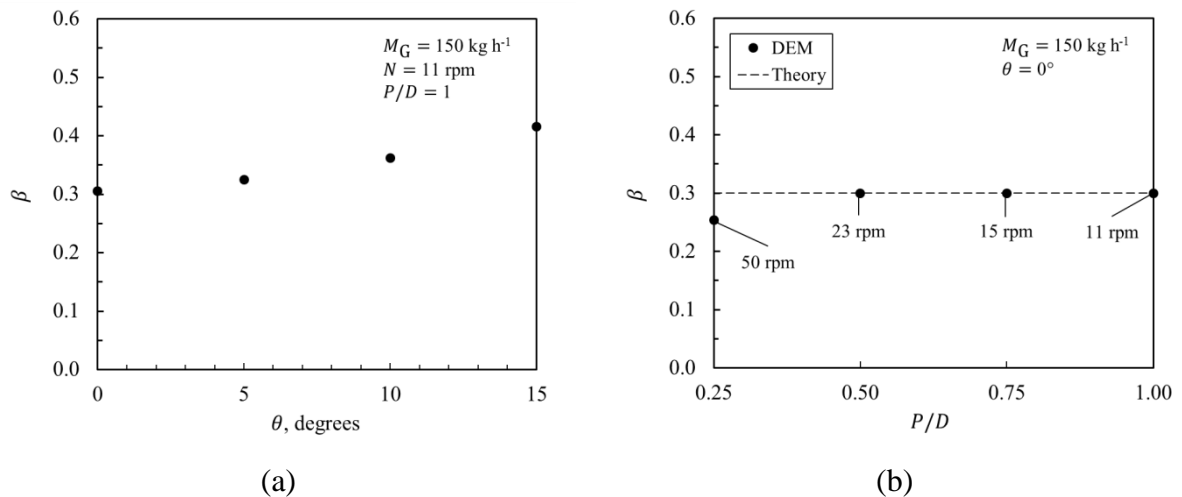


Fig. 4.5. Degree of fullness β with respect to (a) θ and (b) P/D .

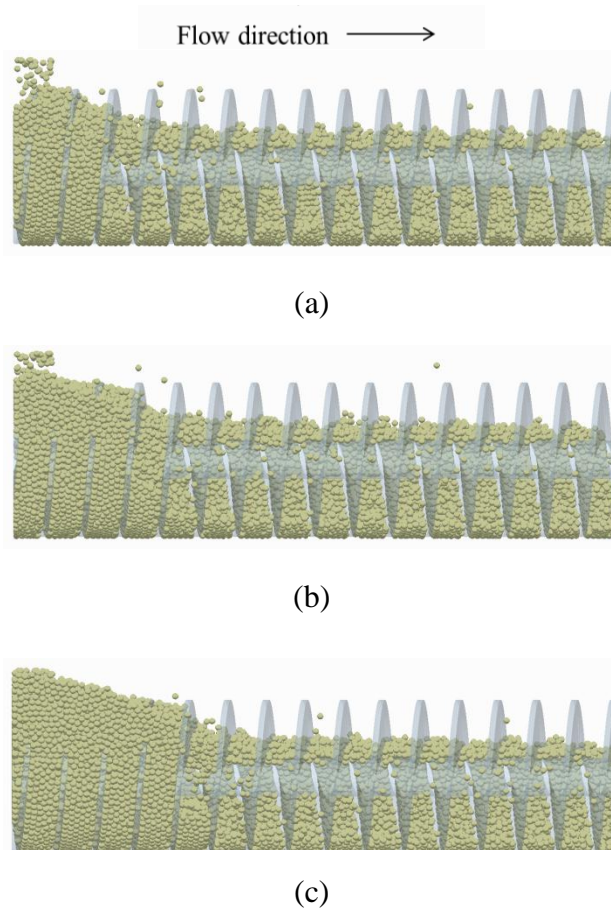


Fig. 4.6. Particle build-up: (a) $M_G = 90 \text{ kg h}^{-1}$, $N = 30 \text{ rpm}$; (b) $M_G = 120 \text{ kg h}^{-1}$, $N = 40 \text{ rpm}$; (c) $M_G = 150 \text{ kg h}^{-1}$, $N = 50 \text{ rpm}$; ($\beta = 0.3$, $P/D = 0.25$).

Additional simulations were carried out to study the effect of N on particle build-up by substituting constant values $\beta = 0.3$ and $P/D = 0.25$ in equation (3.10). It was found that elevated screw speeds indeed increase the tendency for particles to flow backwards (see Fig. 4.6). A low P/D also enhances this reverse flow by providing additional frictional contact with the particles. These results show that too high a flow rate is not suitable for screw conveyor with low P/D since the excessive build-up of particles will jam the conveyor. Furthermore, the extended particle residence time may cause overheating, which is especially hazardous in coal applications. For the particular screw geometry ($P/D = 0.25$), it seems that 90 kg h^{-1} is the maximum flow rate allowable

for safe operation of the screw heater. This additional constrain renders a $P/D = 0.25$ screw conveyor heater highly unattractive compared to its higher P/D counterparts. An application which require a throughput of say 150 kg h^{-1} would require two $P/D = 0.25$ screws versus one $P/D = 0.5$ screw, with the former offering only slight increase in A_{ht}/M_G ratio but significant increase in capital cost compared to the latter. Thus, limitation in throughput coupled with small gain in heat transfer area may not justify the increased material and labor cost of building such screw conveyor.

4.4 Residence time

The residence time τ_R of each particle in the simulation is extracted and presented as probability density functions for the various cases. The effects of solid flow rate, screw speed, angle of inclination, and pitch-to-diameter ratio on the residence time distribution (RTD) are presented in Fig. 4.7, Fig. 4.9, Fig. 4.11, and Fig. 4.13 respectively. Although the RTD was not obtained using conventional experimental methods involving tracer particles, the normalized exit-age distribution function related to the concentration of tracer particles represented by $E(\tau)$, is used by convention. This enables the use of the terms ‘E-curve’ and ‘F-curve’ without causing confusion. The general profile of RTD for all cases is in agreement with those from experiments (Waje *et al.*, 2007). There are two prominent features of the RTD curves namely: the delay, representing the minimum time required moving the solids from the feed to the discharge point; and asymmetry in distribution with generally steep gradients up to the maximum, followed by prolonged tail afterwards. The mean residence time (MRT) and residence

time standard deviation σ_R are given in the graphs for convenience. The vertical lines in Fig. 4.7 to Fig. 4.13 show the position of mean with respect to the RTD.

The RTD closely resembles a normal distribution at low flow rates of 15 and 30 kg h⁻¹ but exhibit skewed profile for flow rates between 50-200 kg h⁻¹. The E-curve ‘tail’ is less prominent at low flow rates indicating the low occurrence of particle back-mixing (see Fig. 4.7). Due to the low degree of fullness ($\beta < 0.1$ for cases A1 and A2; see Fig. 4.4a and Fig. 4.4b), the bulk particles roll forward in the direction of screw front, with only a handful of particles getting elevated above the shaft to participate in the mixing action of the screw. With increasing solid flow rate, a greater number of particles are able to back-mix thus increasing residence time. Fig. 4.8 illustrates the state of the particle bed at steady state (snapshots taken at $t = 123$ s for the various flow rate cases) whereby particles are colored according to residence time. The number of particles having residence time greater than 40 seconds increases with flow rate indicating increased back-mixing. The cross section of the particle bed viewed from the downstream end of the third section (0.24 m from upstream conveyor endplate; see third column of Fig. 4.8) shows that the bulk particles have MRT between 20-25 seconds, which is close to the linear residence time τ_L , defined as the time taken by a particle to traverse the vessel in axial direction; mathematically expressed as:

$$\tau_L = \frac{L}{v_L}, \quad (4.1)$$

where L is the length of the screw conveyor (m) and v_L is the linear screw speed defined as

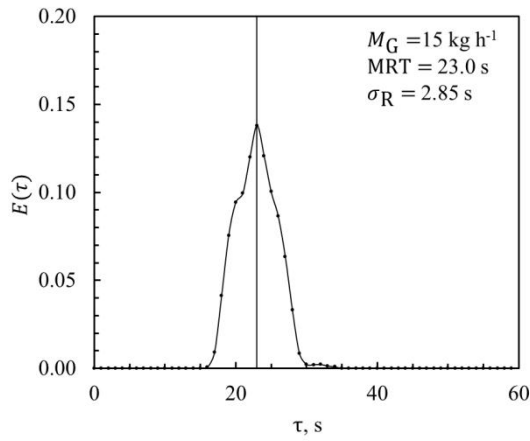
$$v_L = \frac{N \times P}{60} . \quad (4.2)$$

While solid flow rate has little or no effect on the minimum particle residence (also referred to as dead time), increasing the screw speed has the effect of shifting the E-curve towards the left (see Fig. 4.9) and decreasing the MRT to correspond to the increase in axial particle velocity. From the residence time variance σ_R^2 , it is observed that the degree of particle dispersion is attenuated as screw speed is increased from 7 rpm to 19 rpm, provided mass flow rate remain constant. Because degree of fullness is inversely related to screw speed, the mixing effect of the screw is less prominent (since fewer particles are able to roll over the shaft) when screw speed is high. The above observations pertaining to the study of screw speed can be visually confirmed by reference to Fig. 4.10.

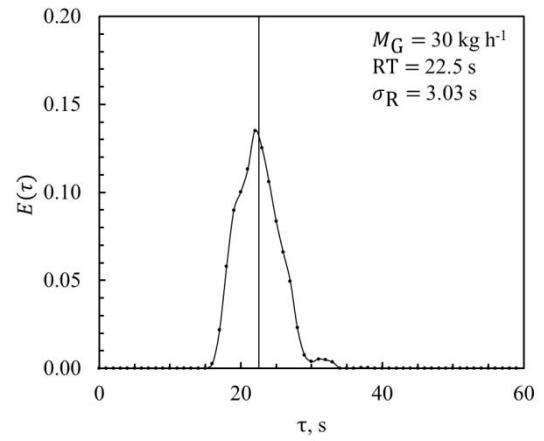
MRT increases from 22.9 seconds to 33.3 seconds when the screw heater is inclined up to 15° from horizontal, with corresponding monotonic increase in σ_R from 5.69 seconds to 9.76 seconds. The forward axial speed of the particles is reduced due to competition with gravity which tends to drive the particles in reverse direction. This effect is more pronounced as the inclination angle θ is increased. At zero inclination scenarios, degree of mixing depended upon the ability of particles to roll over the shaft. At increased θ , there is greater possibility for particles to move in reverse relative to the screw blade by passing over the void region above the screw. Inclination of the screw result in RTD curves becoming increasingly ‘spread’ with corresponding decrease in ‘peak’ residence time (see Fig. 4.11). The distribution of residence time is illustrated in

Fig. 4.12. As can be seen in the figure, the downstream particles emerging from inclined conveyors are relatively more ‘mixed’ compared to horizontal conveyor.

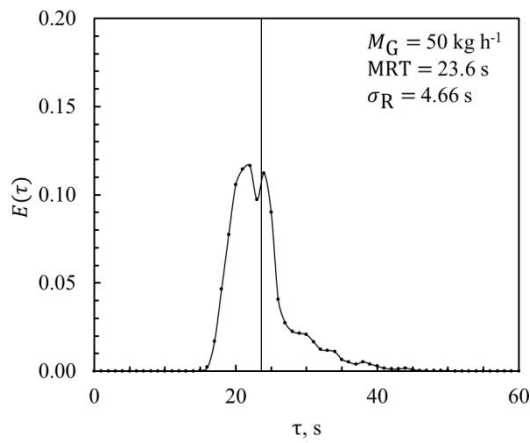
P/D study was set up such that solid flow rate and degree of fullness are constant at 150 kg h^{-1} and 0.3 respectively to ensure that we have a fair comparison. The screw speeds for base case, $P/D = 0.75, 0.5,$ and 0.25 cases are approximately 11 rpm (screw speed for base case) factored by the reciprocal of the corresponding pitch-to-diameter ratios. This ensures that linear screw speed v_L is constant ($NP/60 \sim 1.47 \text{ m s}^{-1}$) for all cases. Results showed that reducing screw pitch from 80 mm to 40 mm ($P/D = 1$ and 0.5 respectively) have limited effect on MRT. Nevertheless the trend is that of decreasing MRT and σ_R with P/D for P/D between 0.5 and 1. In this range, granular flows also tend to approach plug-flow behavior as P/D decrease. This does not apply to $P/D = 0.25$ case however. In Fig. 4.14d, the downstream cross section view show significant reduction in degree of fullness β from the base case. Earlier we mentioned that the screw speeds for the different P/D cases are determined such that β is constant. In reality, β deviate considerably for $P/D = 0.25$ (see Fig. 4.5) the reason for which has been discussed. In practical situation, it is hypothesized that β will increase beyond 0.3 as the build-up region is conveyed forward, while M_G plunge due to increasing congestion. Eventually, this will lead to either one of the two scenarios depending upon the power of the motor driving the screw: (1) $\beta \rightarrow 1$ and $M_G \rightarrow 0 \text{ kg h}^{-1}$ due to motor not being powerful enough push through the load, or (2) $\beta \rightarrow 1$ and $M_G \rightarrow 150 \text{ kg h}^{-1}$ if a motor exceeding design requirements is used.



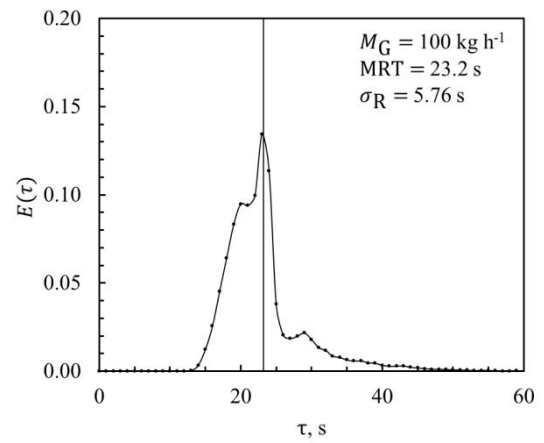
(a)



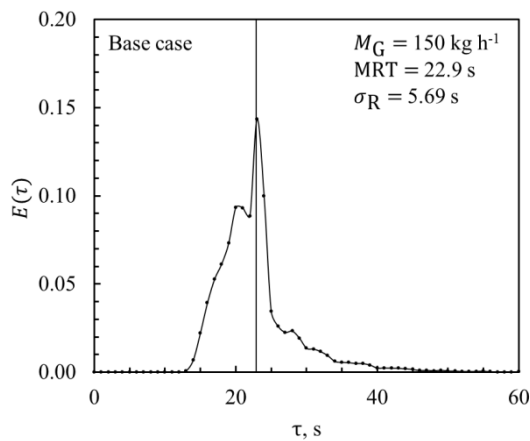
(b)



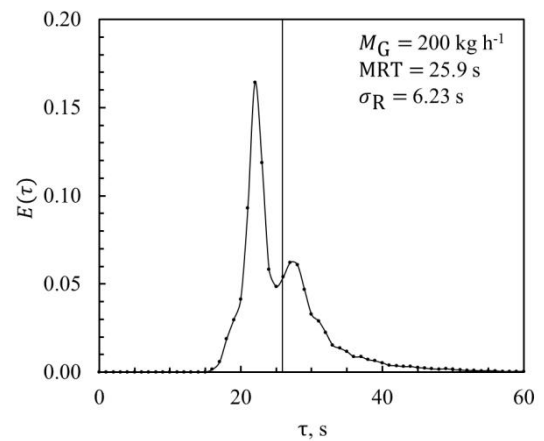
(c)



(d)



(e)



(f)

Fig. 4.7. Residence time distributions for various M_G . ($M_G = 75$ and 175 kg h^{-1} are omitted due to space constraint).

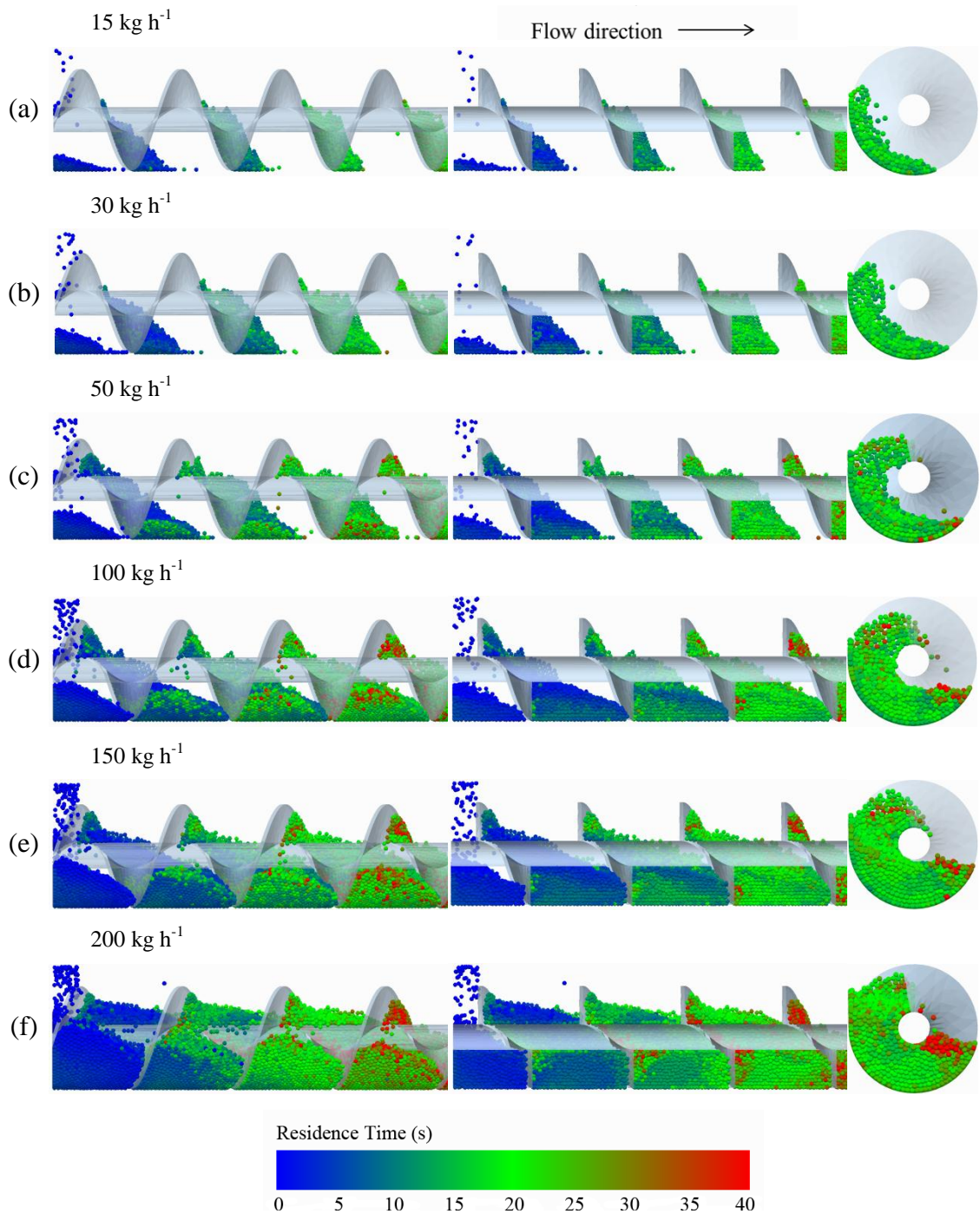


Fig. 4.8. Distribution of particle residence times for various M_G . Views from left to right: side view, longitudinal slice view, third quadrant cross-section view.

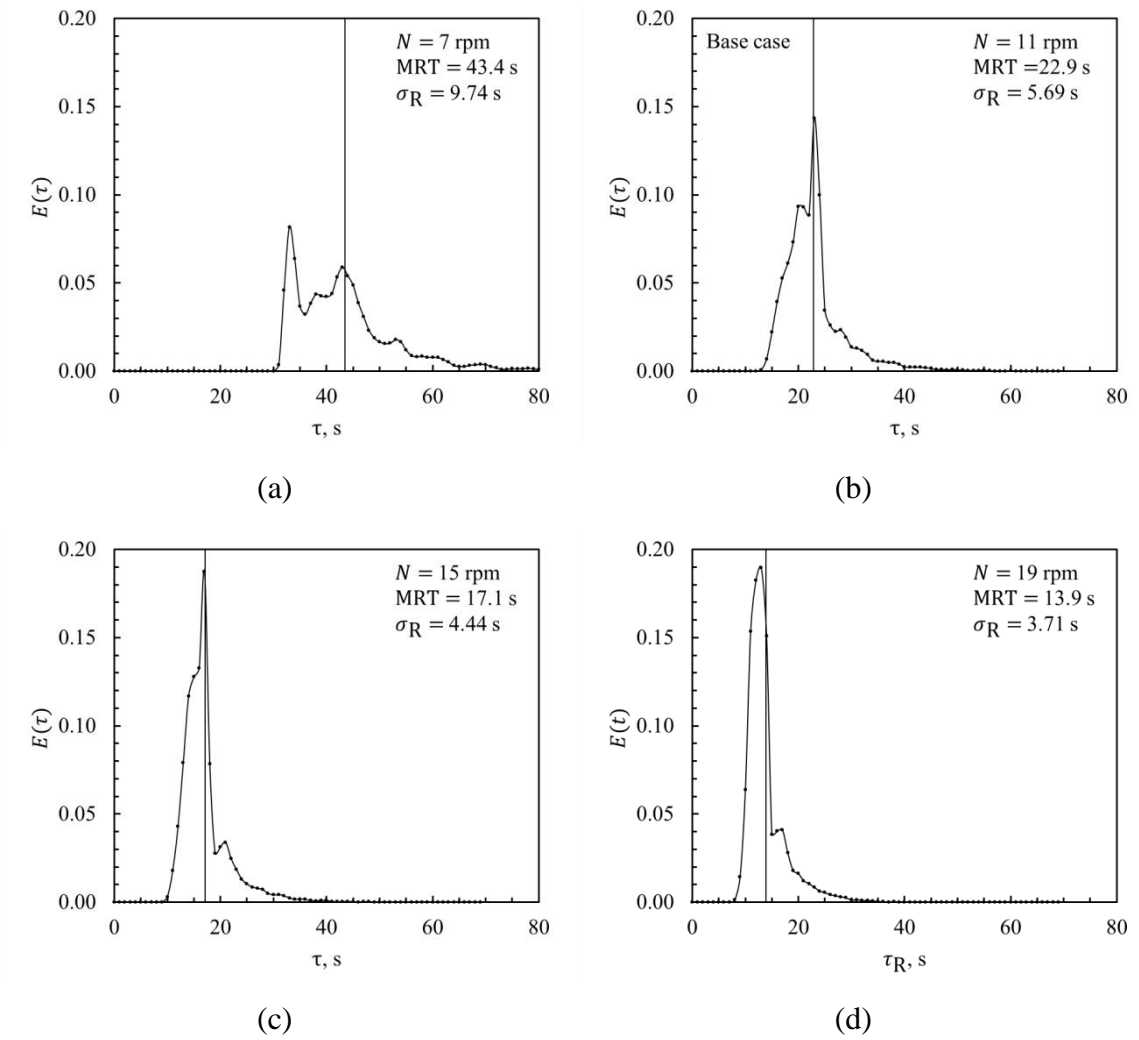


Fig. 4.9. Residence time distributions for various N .

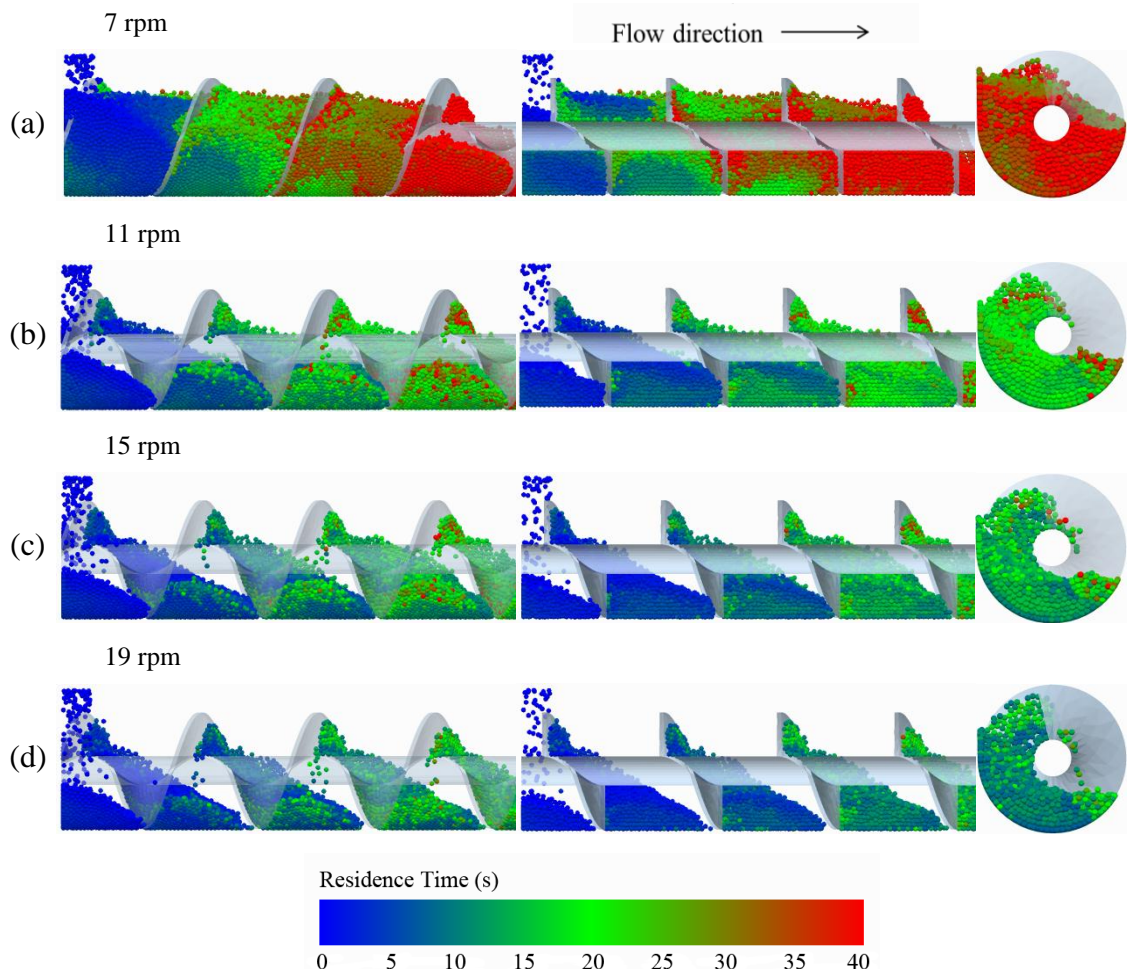


Fig. 4.10. Distribution of particle residence times for various N . Views from left to right: side view, longitudinal slice view, third quadrant cross-section view.

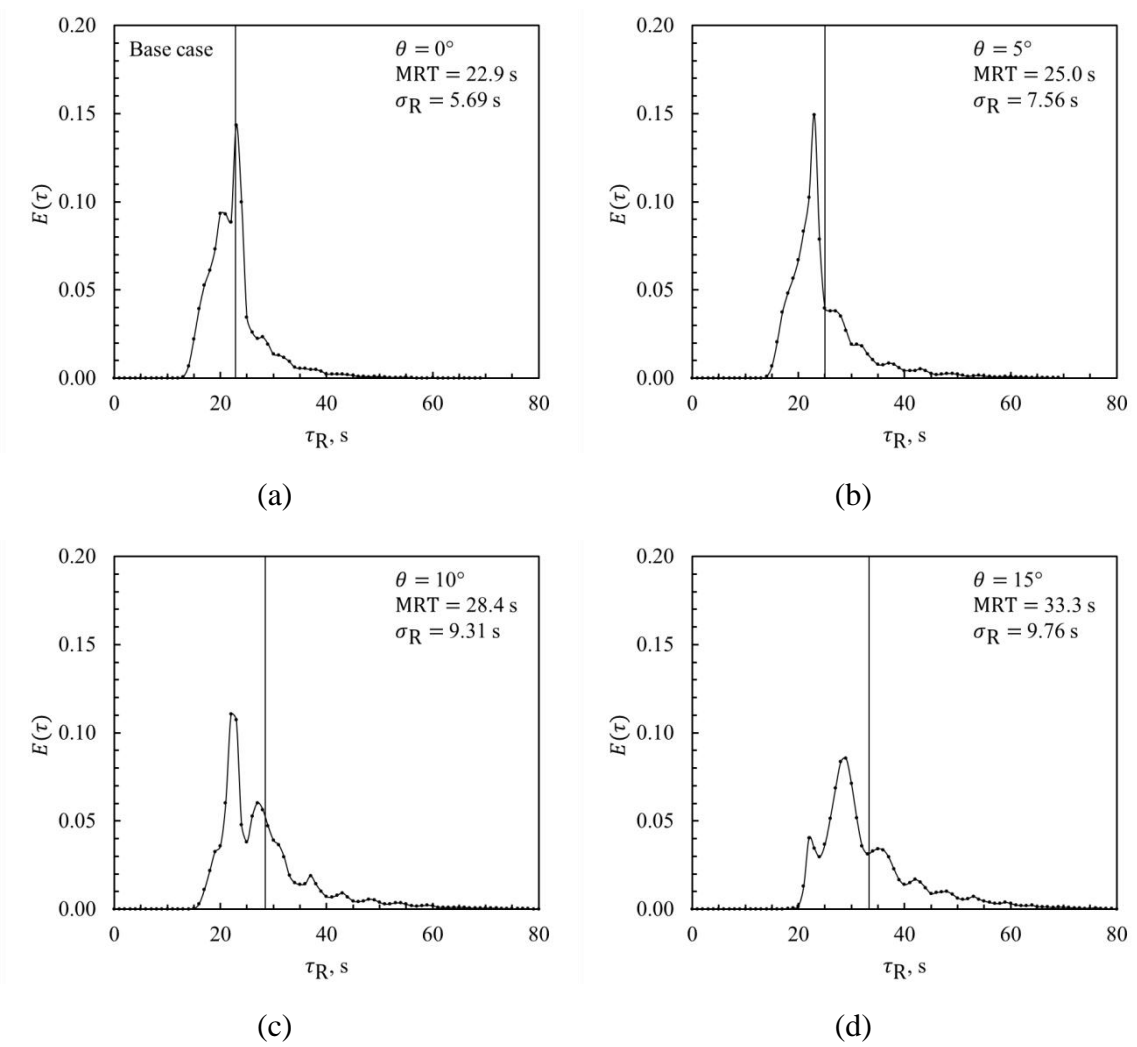


Fig. 4.11. Residence time distributions curves for various θ .

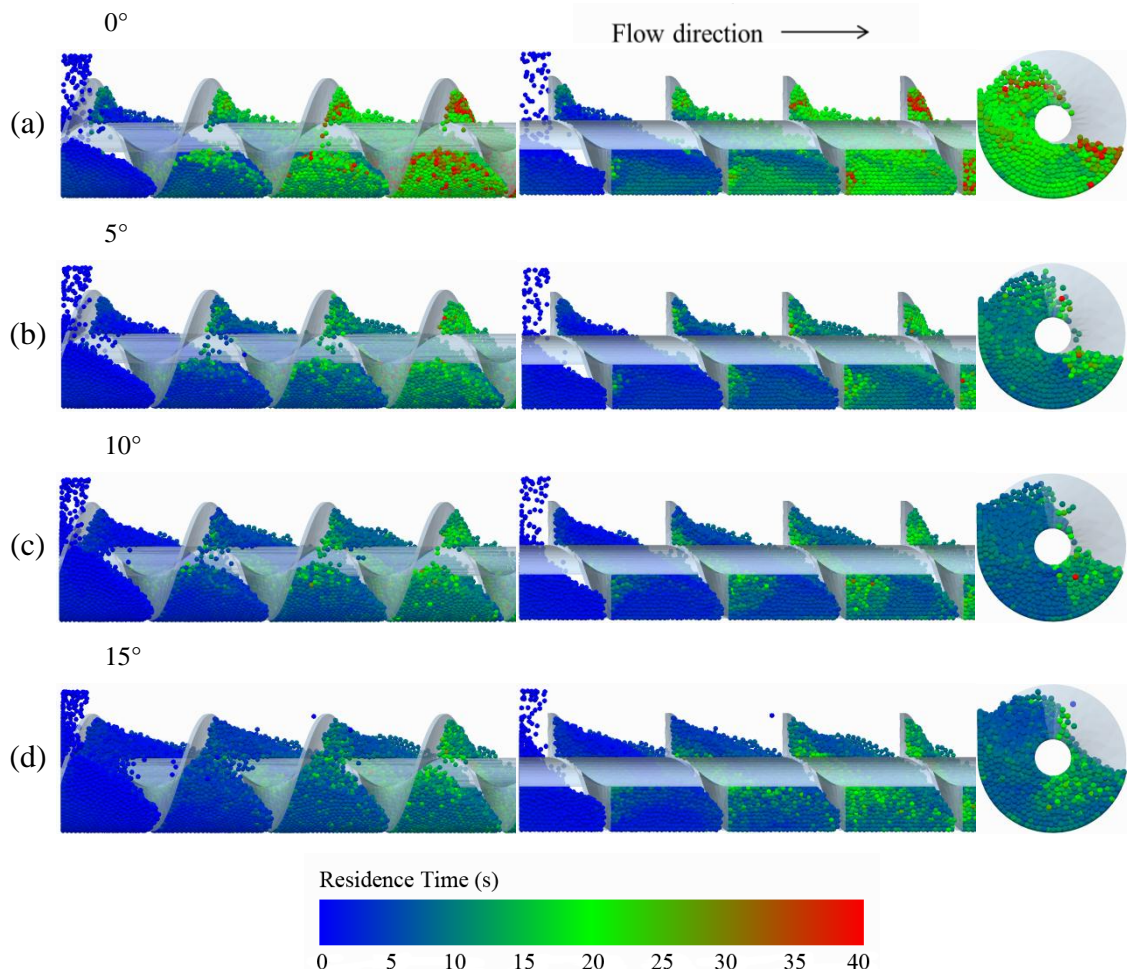


Fig. 4.12. Distribution of particle residence times for various θ : (a) 0, (b) 5, (c) 10, and (d) 15 degrees.

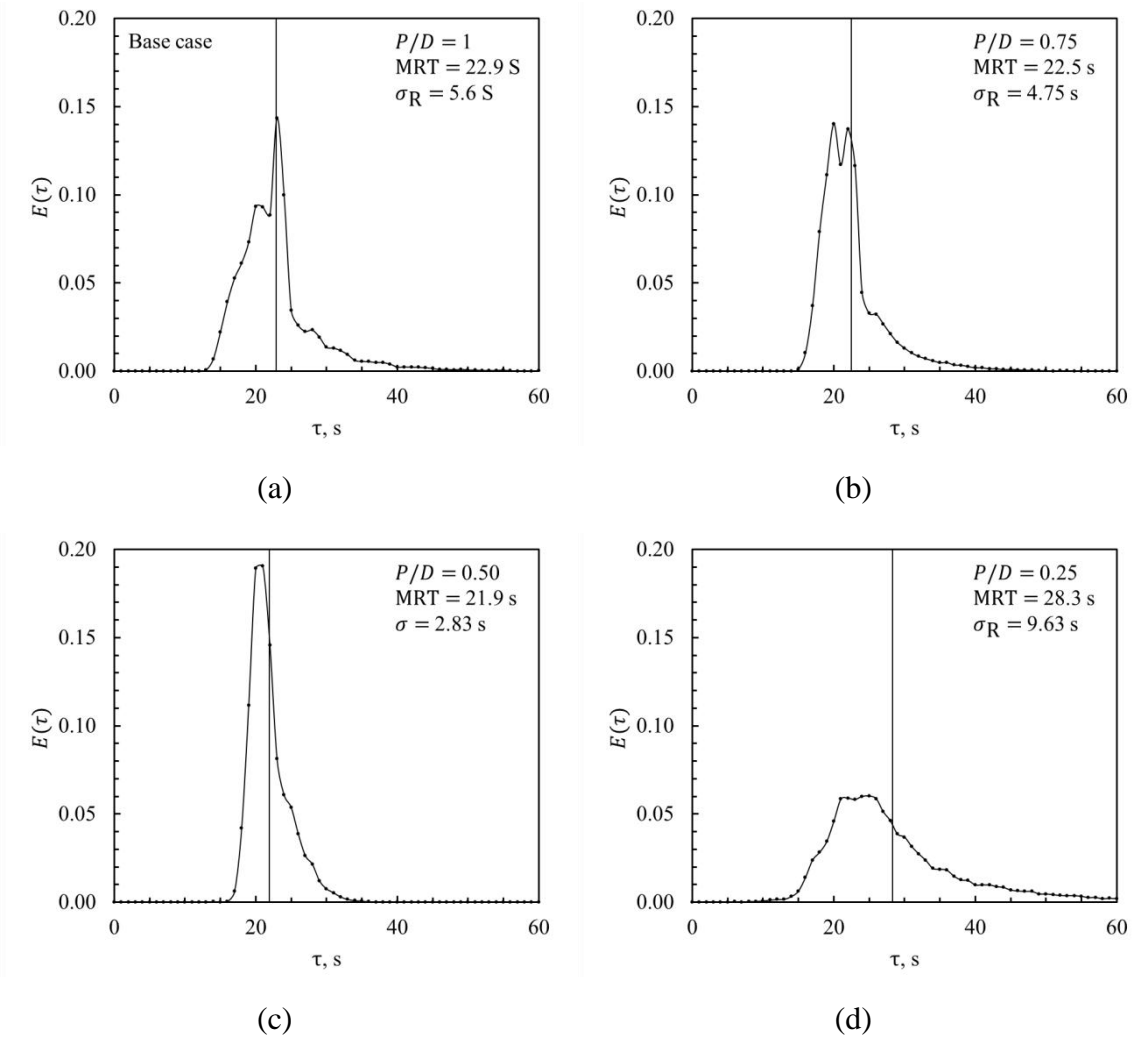


Fig. 4.13. Residence time distributions curves for various P/D .

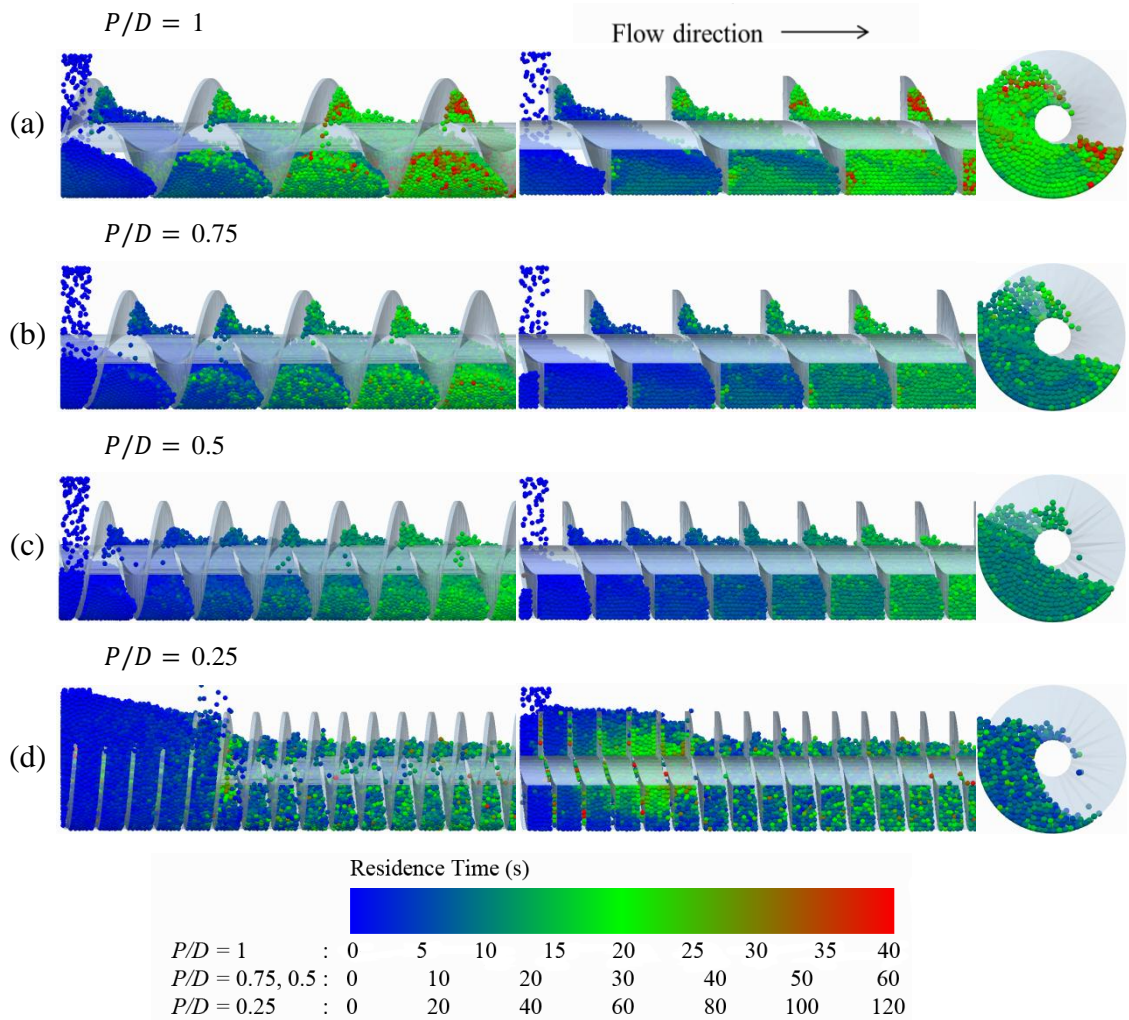


Fig. 4.14. Distribution of particle residence times for various P/D . Views from left to right: side view, longitudinal slice view, third quadrant cross-section view.

4.5 Hold-back and segregation

The degree of mixing in batch and continuous processors have been described using dispersion and Peclet numbers (Ai *et al.*, 2011). Some investigators have also used standard deviation as a measure of discharge uniformity (Deveswaran *et al.*, 2009). Hold-back H and segregation S provide another means of quantifying the degree of mixing. Holdback is a measure of departure from an idealized plug-flow condition of the continuous flow system, and is given by the area bounded by $F(\xi)$ and $F(\xi)_{\text{plug}}$, which is equivalent to area under $F(\xi)$ in the range $0 \leq \xi \leq 1$ (Danckwerts, 1958). Segregation is the departure from perfectly mixed-flow condition of the continuous flow system, and is given by the area bounded by $F(\xi)$ and $F(\xi)_{\text{mixed}}$ between $\xi = 0$ and $\xi(F(\xi) = F(\xi)_{\text{plug}})$ (Danckwerts, 1958). $F(\xi)$ is the non-dimensionalized cumulative distribution function where we have defined the non-dimensional parameter ξ in terms of mass; i.e. $\xi = M_G \tau / M_H$.

Results show that H increased from 0.048 to 0.151 when flow rate is increased from 15 kg h^{-1} to 175 kg h^{-1} , but declined with further increase in flow rate. Flow rates of 15 and 30 kg h^{-1} closely resemble plug flow with limited longitudinal mixing. The plug flow resemblance at low flow rate is attributed to low degree of fullness which inhibited the tumbling of particles over the shaft. For the range of screw speeds simulated, it was found that screw speed has no influence on H and S . For angle of inclinations θ between 0° and 10° , the effect on mixing characteristics of the screw conveyor heater is somewhat limited, but starts to get more obvious at 15° . As observed in Fig. 4.15c and Table 4.1, increasing inclination from 10° to 15° causes H to decrease by more than

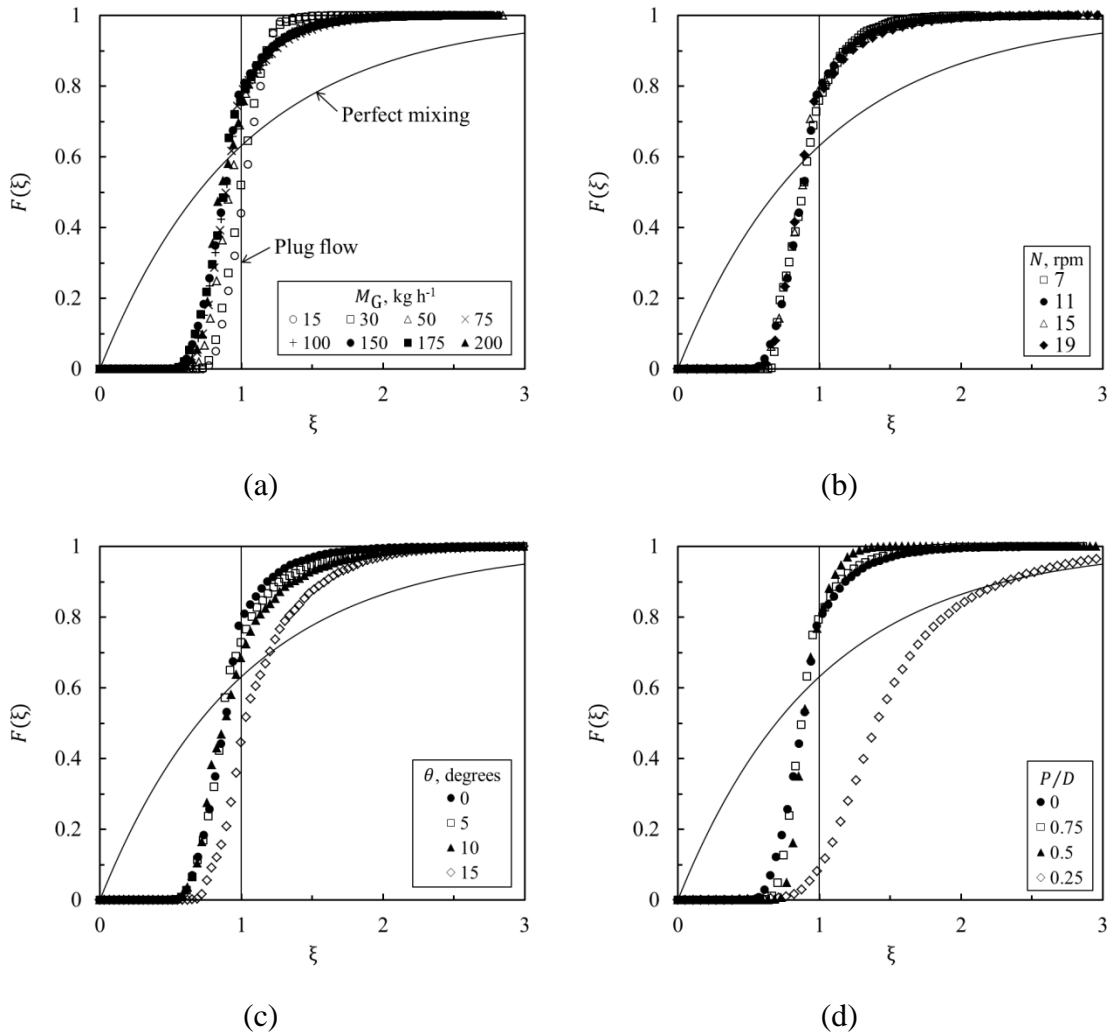


Fig. 4.15. Holdback and segregation of particles in a screw conveyor heat exchanger for various cases.

200%. However this does not mean that the flow is approaching plug-flow scenario. The decrease in H is primarily due to the shifting of the F-curve to the right, rather than a change of gradient. The F-curve shift indicates an increase in dead time due to particles falling back under the influence of gravity, which consequently result in overall increase in MRT. A similar situation is observed for $P/D = 0.25$ case where dramatic decrease in H is accompanied by dramatic increase in S when P/D is reduced from 0.5. For P/D between 0.5 and 1, it is observed that the flow approaches plug-flow as P/D

decreases, albeit a gradual change. Lowering the P/D further by a factor of two does not lead to a more plug-flow characteristics, but rather a large departure from it. As discussed earlier, this is due to the combination of increased frictional surface area and high screw speed which increases the tendency for particles flow in reverse, resulting in large particle build-up upstream. The dispersion effect of screw conveyor is illustrated in Fig. 4.16.

Table 4.1. Summary of granular flow characteristics for various cases.

Case	β	MRT	σ_R	H	S
Base	0.31	22.85	5.69	0.148	0.242
A1	0.03	22.96	2.85	0.048	0.337
A2	0.05	22.53	3.03	0.060	0.321
A3	0.10	23.63	4.66	0.104	0.276
A4	0.15	23.71	5.80	0.131	0.257
A5	0.20	23.19	5.76	0.137	0.250
A6	0.37	23.53	5.99	0.151	0.239
A7	0.46	25.91	6.93	0.139	0.242
B1	0.59	43.43	9.74	0.144	0.244
B2	0.23	17.12	4.44	0.150	0.238
B3	0.18	13.90	3.71	0.152	0.237
C1	0.33	25.00	7.56	0.149	0.236
C2	0.36	28.41	9.31	0.146	0.234
C3	0.42	33.32	9.76	0.056	0.338
D1	0.30	22.50	4.75	0.139	0.252
D2	0.30	21.94	2.83	0.112	0.277
D3	0.25	28.30	9.63	0.011	0.609

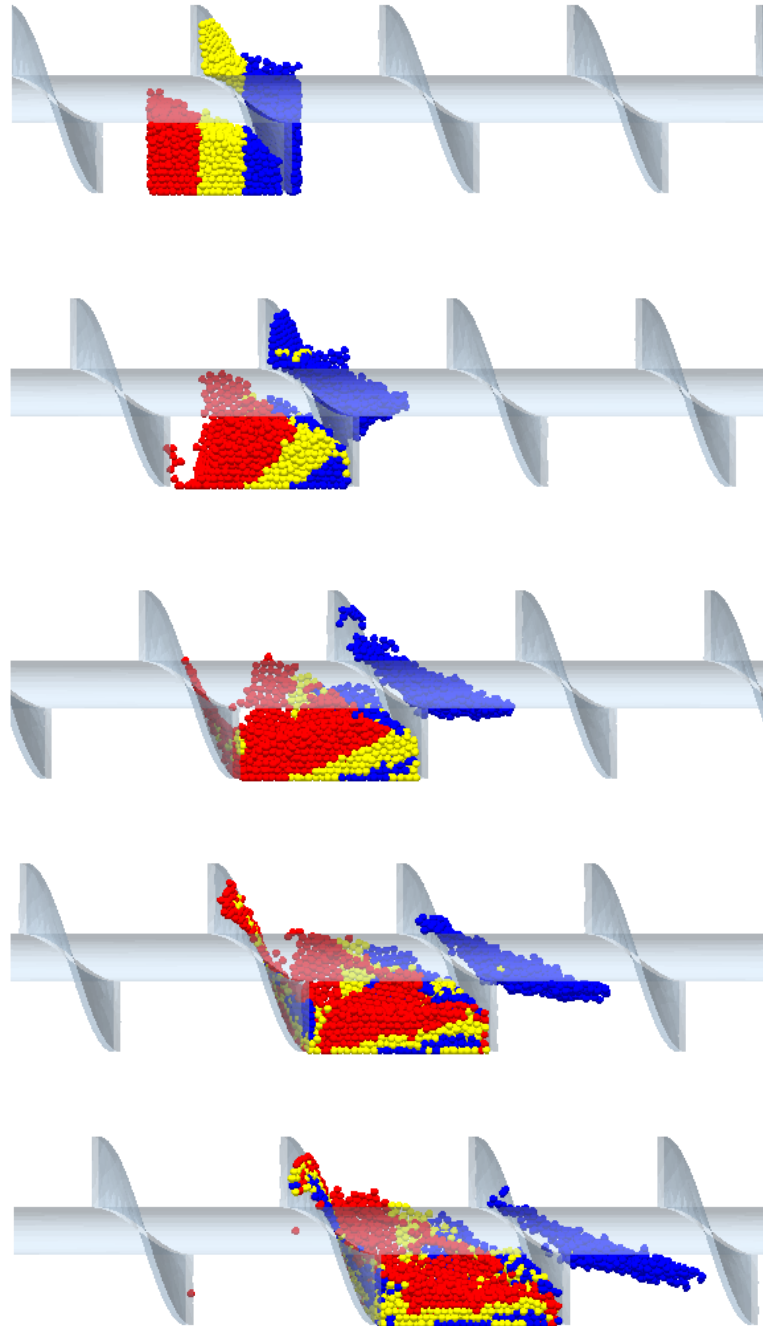


Fig. 4.16. Visualization of axial mixing of particle bed in screw conveyor heat exchanger
(Base case: $M_G = 150 \text{ kg h}^{-1}$, $N = 11 \text{ rpm}$, $P/D = 1.0$).

Chapter 5

Heat Transfer Characteristics

5.1 Introduction

This chapter focuses on the thermal effects of varying certain operational and geometrical parameters of a screw conveyor heater. As in the granular flow study, glass spheres with diameter 3.1 mm were used as simulated particles flowing through a 0.32 m long screw conveyor heater which take on the thermal properties of copper. As a simplification, the entire screw conveyor assembly is isothermal at 373 K to simulate jacket heating by continuous flow of steam. The screw blades and shaft are also assumed to be at a constant temperature of 373 K which in reality is achieved by hollow construction to allow steam to flow through. The DEM is programmed such that heat transfer occurs only within the screw conveyor heater domain. Upon exiting the domain through the discharge, the temperature of each particle is locked and no further thermal exchange take effect. In reality, particles collected at the end of the discharge will lose heat to the surrounding. However, since we are only concerned with the thermal effectiveness of the heater, the cooling effect due to exposure to atmosphere is neglected.

5.2 Evolution of T_{bed} and τ

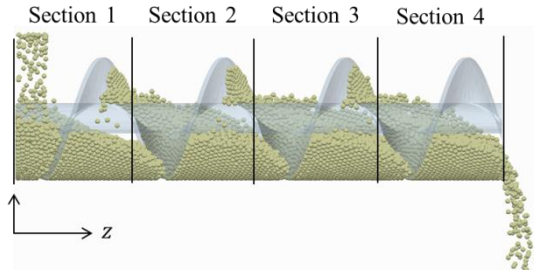


Fig. 5.1. Binning the screw conveyor domain for heat transfer analysis.

With reference to Fig. 5.1, a particle can fall within Section 1, 2, 3 or 4 at a particular time step, if its geometric centre lies within $0 \leq z < 0.08$, $0.08 \leq z < 0.16$, $0.16 \leq z < 0.24$, or $0.24 \leq z < 0.32$ m respectively. At steady state, bed temperature and residence time inside the screw conveyor domain is a function of distance, i.e. $T_{\text{bed}} = T_{\text{bed}}(z)$ and $\tau = \tau(z)$. By segmenting the screw conveyor domain into 4 equal sections, the bed temperature and mean residence time in each section can be calculated. Note that we use τ to denote evolving mean residence time as the bed flows through the screw conveyor, to distinguish from MRT which is understood as the mean residence time of the particles at the discharge of the screw conveyor.

Fig. 5.2 and Fig. 5.3 are produced to show that at steady state, T_{bed} and τ depend only on position along the axis of the screw. This is true for all the cases studied, with the exception of Case D3, hence evolution of T_{bed} and τ are shown only for six cases ($M_G = 15, 30, 50, 100, 150, 200 \text{ kg h}^{-1}$) are shown graphically, while results for others cases are summarized in Table 5.1.

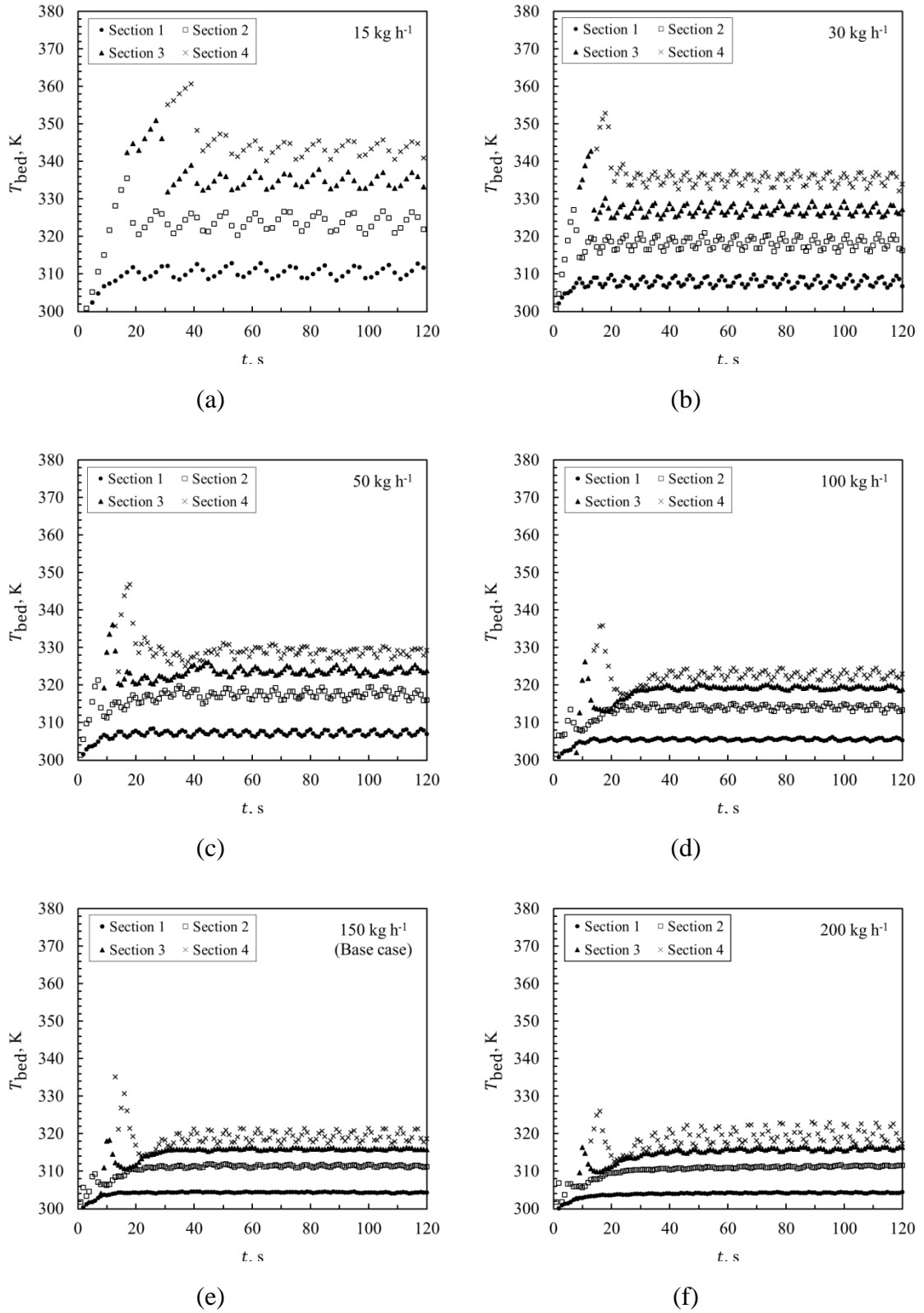


Fig. 5.2. T_{bed} along the length of screw conveyor heater for various M_G ($N = 11$ rpm, $\theta = 0^\circ$, $P/D = 1$).

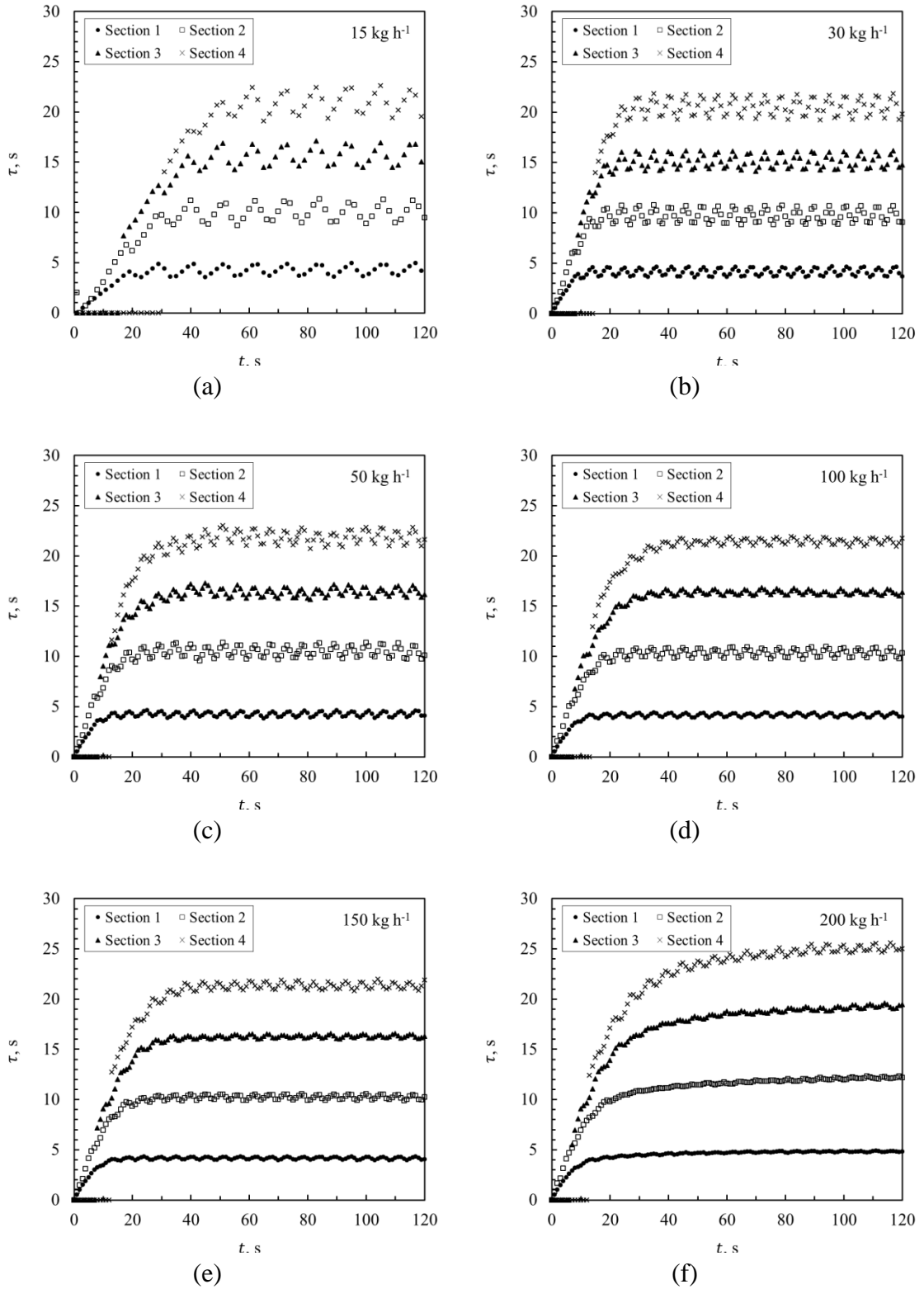


Fig. 5.3. τ along the length of screw conveyor heater for various M_G ($N = 11$ rpm, $\theta = 0^\circ$, $P/D = 1$).

Table 5.1. Summary of T_{bed} and τ for various cases.

Case	Section 1		Section 2		Section 3		Section 4	
	T_{bed} , K	τ_1 , s	T_{bed} , K	$\tau_2 - \tau_1$, s	T_{bed} , K	$\tau_3 - \tau_2$, s	T_{bed} , K	$\tau_4 - \tau_3$, s
Base	304	4.1	311	6.1	316	6.0	319	5.0
A1	311	4.2	304	5.8	335	5.6	343	5.4
A2	308	4.1	318	5.6	327	5.4	335	5.4
A3	307	4.3	317	6.3	323	5.9	329	5.5
A4	306	4.2	316	6.3	322	6.1	325	5.2
A5	305	4.2	314	6.2	319	6.0	323	5.1
A6	304	4.3	311	6.4	315	6.3	319	5.3
A7	304	4.8	311	7.3	316	7.1	320	5.9
B1	306	7.9	315	12.7	322	12.4	326	8.9
B2	304	3.1	311	4.6	315	4.5	318	3.7
B3	303	2.6	310	3.8	314	3.7	316	3.1
C1	305	4.7	313	7.2	318	6.6	321	5.2
C2	305	5.5	314	8.4	319	7.7	323	6.0
C3	306	6.3	314	9.7	320	8.9	324	7.3
D1	304	3.7	311	5.8	316	6.1	320	5.4
D2	303	3.1	310	5.6	316	6.0	321	5.4
D3	316	13.0	324	9.5	328	1.8	333	4.5

In Fig. 5.2, it is observed that increase in flow rate lowers the bed temperature. This shows that mixing is generally poor since only particle in contact with the heated surfaces are contributing to T_{bed} while the bulk are still relatively cool. With increased M_G , the ratio of hot particles to cool particles decreased, hence the lowered bed temperature. T_{bed} increases with angle of inclination θ due particles rolling against the direction of screw, under the influence of gravity. The effect of gravity is more obvious at high θ , and corresponds to longer residence time τ and consequently greater T_{bed} . As

shown in Table 5.1 P/D has little effect on T_{bed} , due to zero net increase in effective heat transfer surface area A_{ht} , which will be discussed in later section.

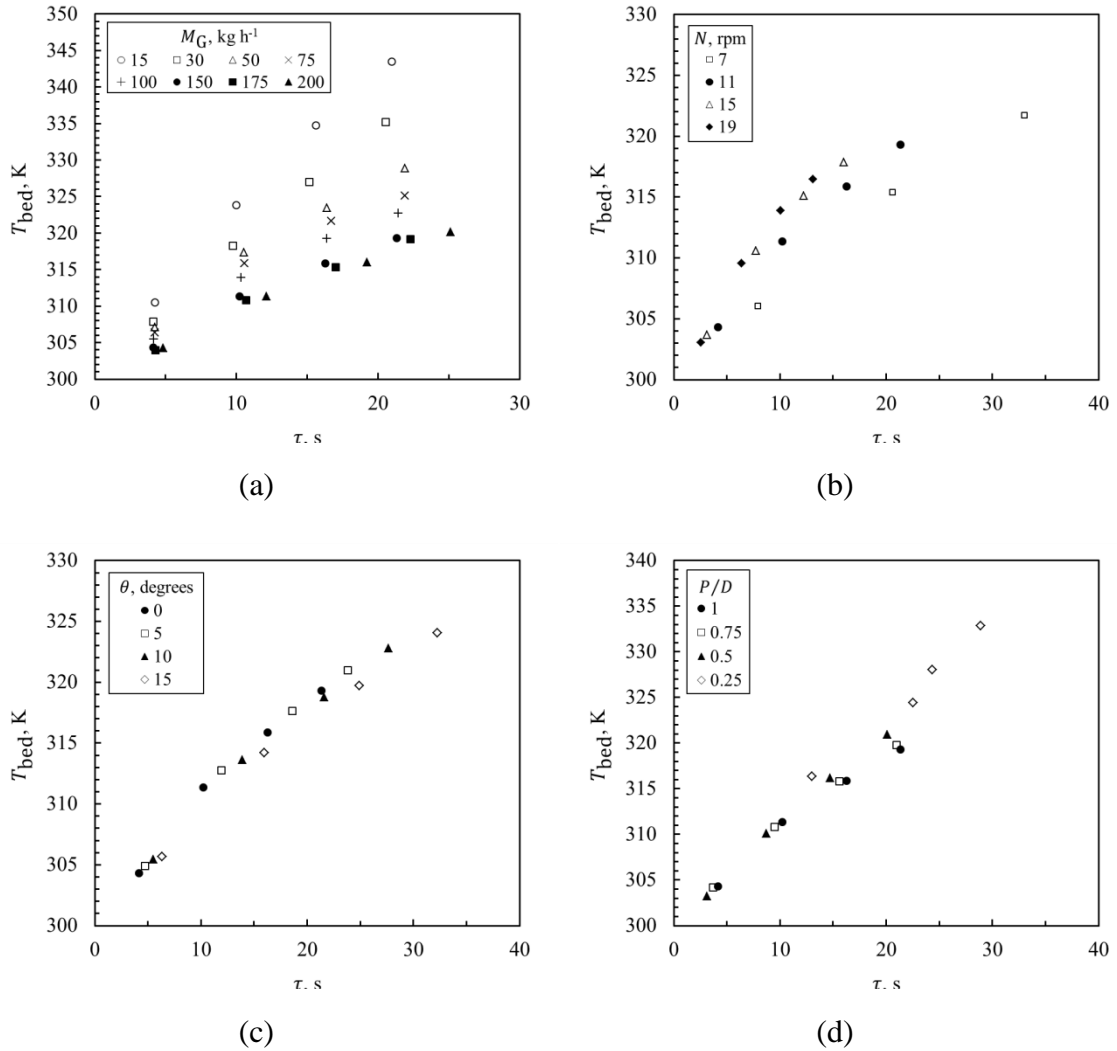


Fig. 5.4. T_{bed} vs τ for various cases.

As mentioned earlier, both T_{bed} and τ are functions of distance only once the flow has stabilized. A plot of T_{bed} against τ (see Fig. 5.4) shows that the effect of M_G on T_{bed} is quite apparent. It is observed that the heating rate is greatest for 15 kg h⁻¹ and lowest for 200 kg h⁻¹, with marginal difference in heating rate between 150 and 200 kg h⁻¹.

5.3 Temperature distribution in screw conveyor heater

5.3.1 Effect of solid flow rate

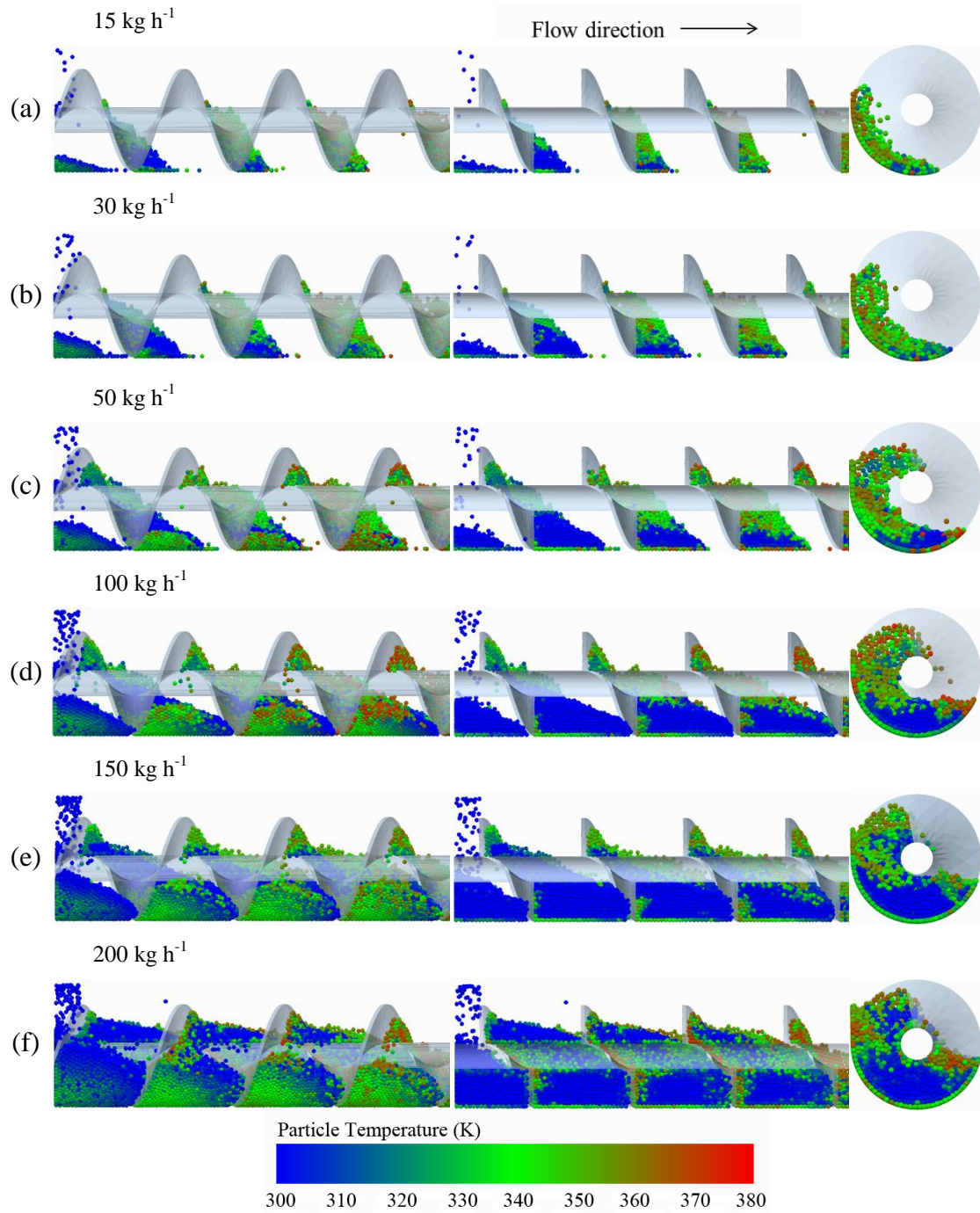


Fig. 5.5. Distribution of particle temperature for various M_G . Views from left to right: side view, longitudinal slice view, third quadrant cross-section view.

The cross section temperature distribution looking from the downstream end shows that particle at the core is elevated to less than 305 K from initial temperature of 298 K. The presence of a cool core (CC) is evidence for the lack of radial mixing (see Fig. 5.5). On the other hand, the progressive shrinking of CC the bed progresses towards the discharge shows that some mixing do occur, albeit on a limited scale due to the length of screw simulated. The size of CC increases with flow rate, to be consistent with the increasing degree of fullness.

5.3.2 Effect of screw speed

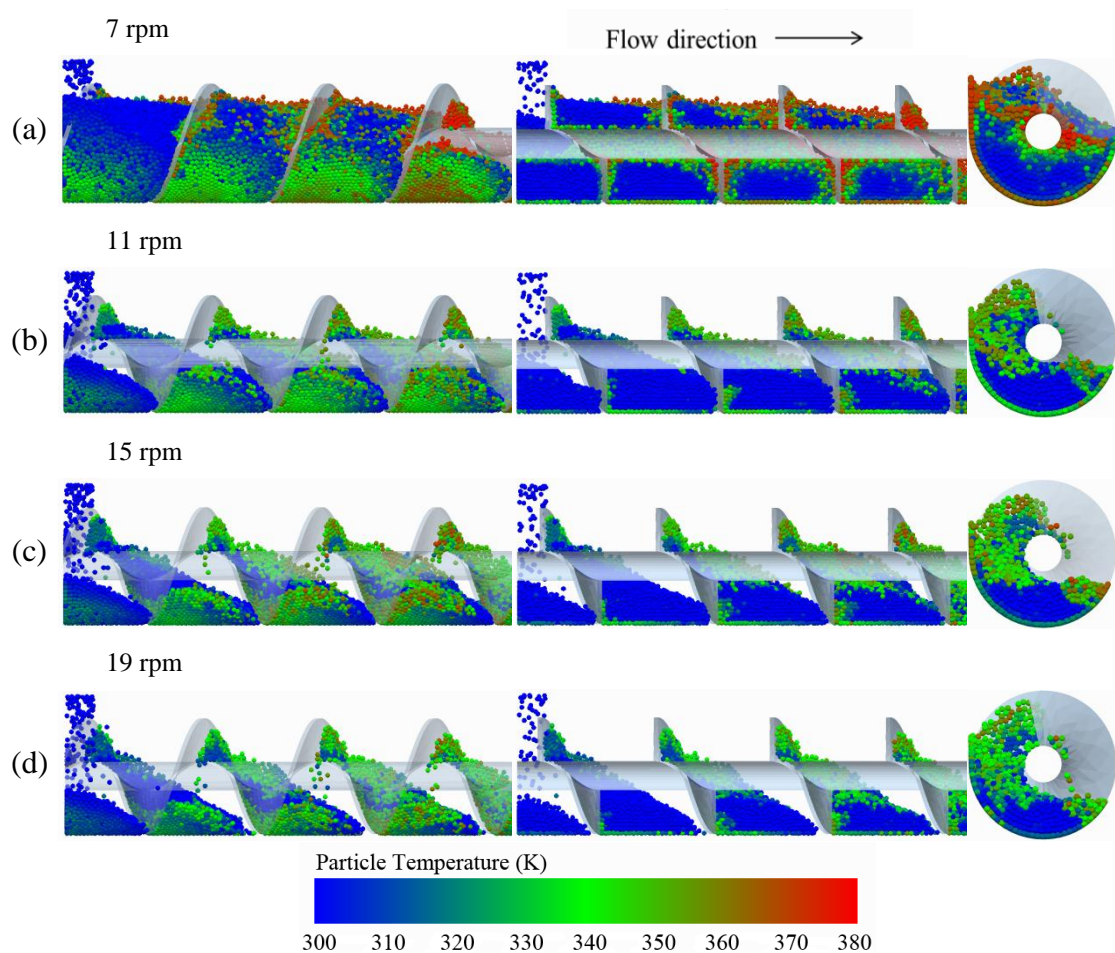


Fig. 5.6. Distribution of particle temperature for various N . Views from left to right: side view, longitudinal slice view, third quadrant cross-section view.

Compared to the base case ($N = 11$ rpm), screw speed of 7 rpm resulted in greater disparity in temperature between the cool core and the heated surface particles. As shown in Fig. 5.6a, particles in contact with the heated surfaces are close to 370 K while the core is still cool at around 310 K. This shows that there is little or no improvement in mixing since the elevated surface temperature is primarily due to longer wall-particle contact time. From this observation, it is deduced that the flow of particles, especially those in contact with the through surface, are mostly linear in the positive z direction with almost no radial motion or recirculation. As with the M_G cases, the core remain cool due to poor conductivity of the bed, and poor mixing of the heater.

5.3.3 Effect of inclination angle

In contrast with the M_G and N cases, the effect of inclination angle on mixing and heat transfer is more apparent. It is quite apparent that mixing becomes progressively more effective as θ is increased. As shown in Fig. 5.7, cool particles are more disposed from the core as heated surface (HS) particles fold into the bed under the influence of gravity and screw motion.

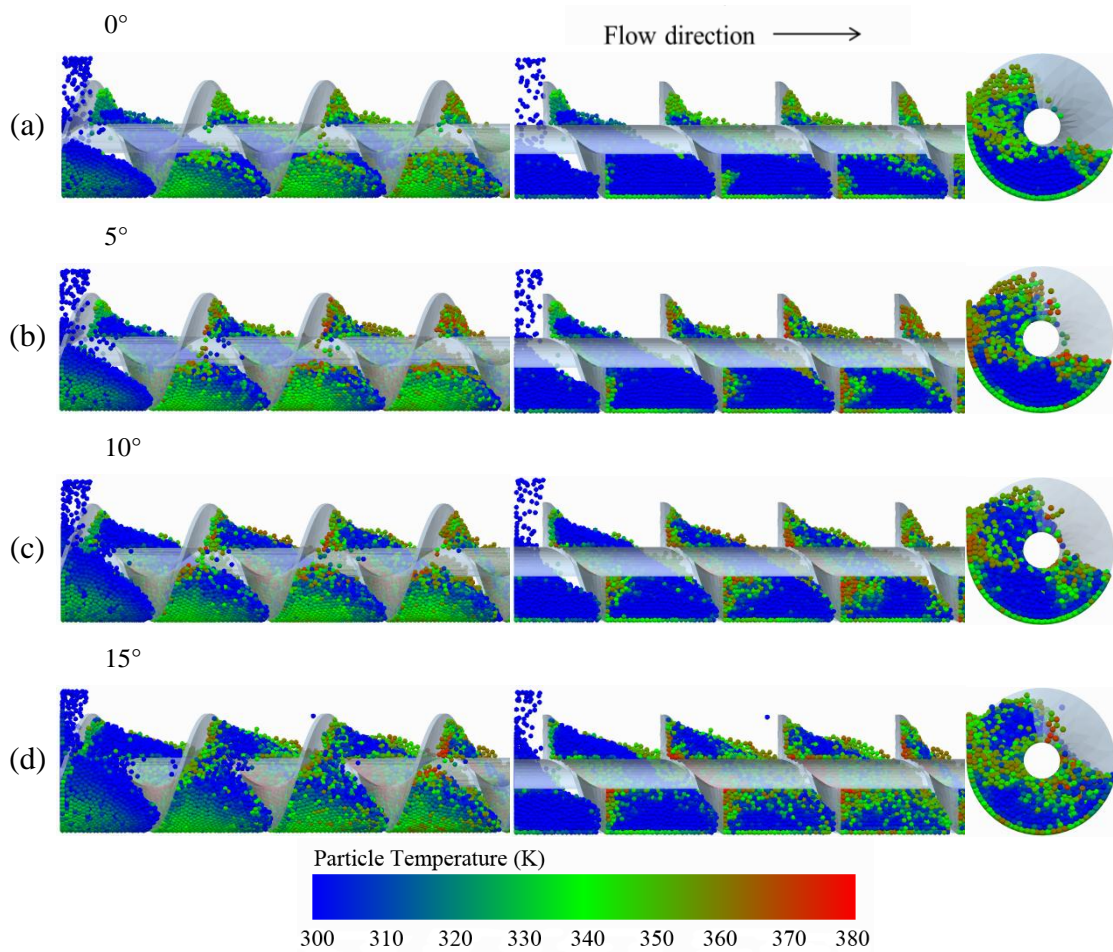


Fig. 5.7. Distribution of particle temperature for various θ . Views from left to right: side view, longitudinal slice view, third quadrant cross-section view.

5.3.4 Effect of pitch-to-diameter ratio

Decreasing the pitch-to-diameter ratio, hence increasing the number of flights per unit length of screw, clearly exposes more of the bed to the heated surfaces. As shown in Fig. 5.8, there is marked reduction in the size of the cool core as P/D is reduced from 1 to 0.5. For $P/D = 0.25$, all of the bed is heated with no sight of a cool core, effectively demonstrating dramatic improvement in heating uniformity. However, construction of a screw conveyor with such low P/D may require further analysis of the costs involved considering the amount of construction material required.

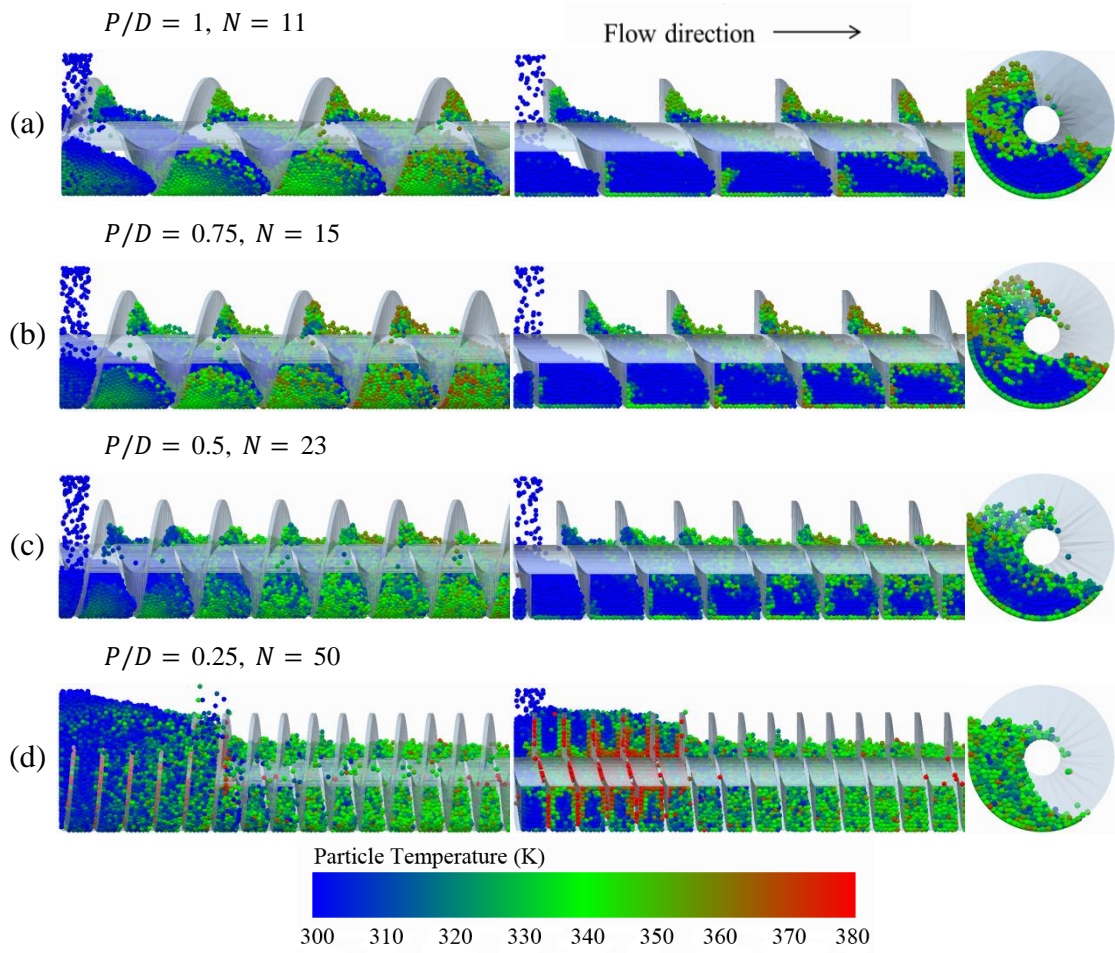


Fig. 5.8. Distribution of particle temperature for various P/D . Views from left to right: side view, longitudinal slice view, third quadrant cross-section view.

5.4 Discharge temperature

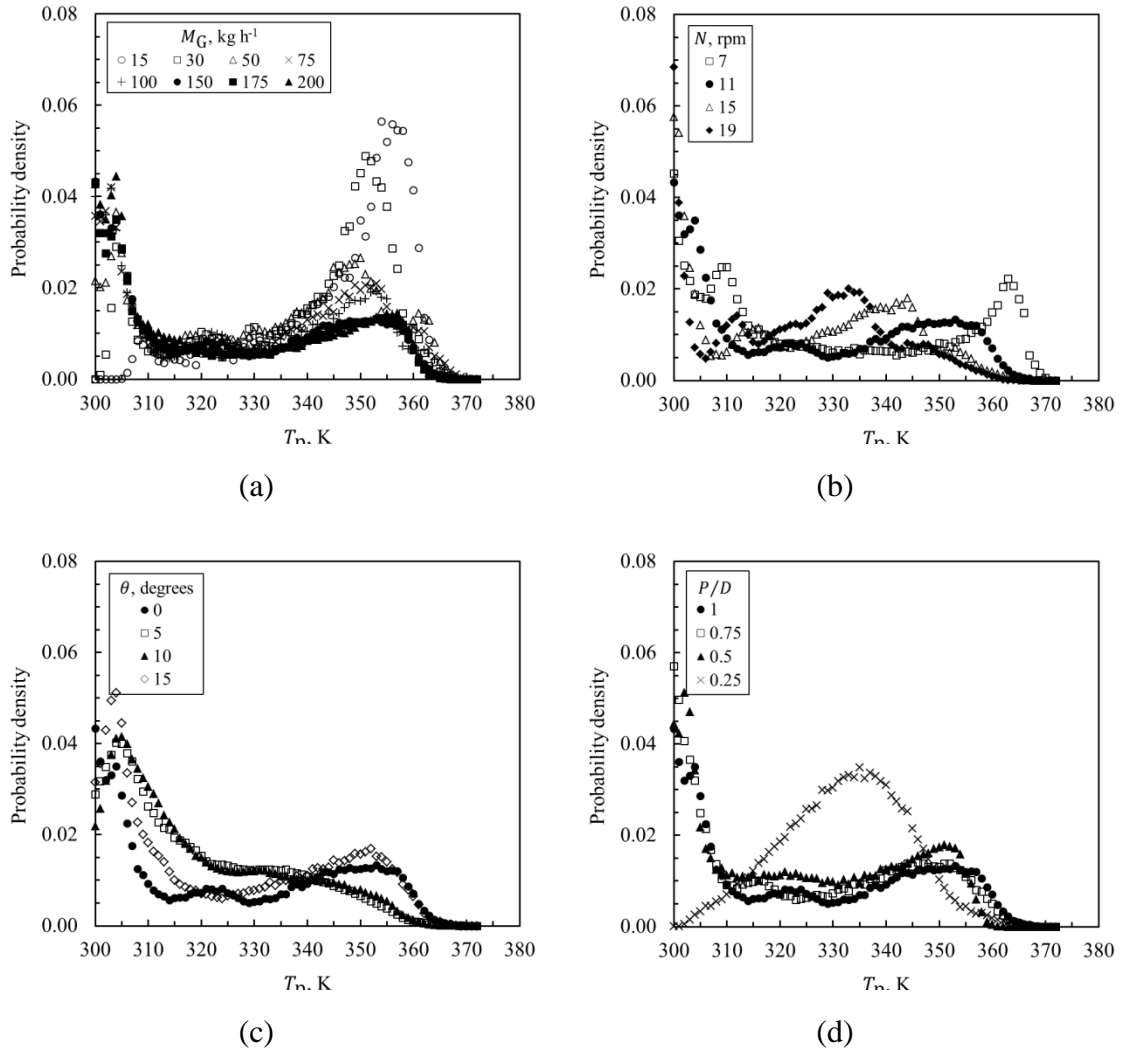


Fig. 5.9. Discharge temperature distribution for various cases: (a) solid flow rates ($N = 11$ rpm, $P/D = 1.0$), (b) screw speed ($M_G = 150$ kg h^{-1} , $P/D = 1.0$), (c) angle of inclination ($M_G = 150$ kg h^{-1} , $N = 11$ rpm), and (d) pitch-to-diameter ratio ($M_G = 150$ kg h^{-1} , $N = 11$ rpm).

The discharge temperature is obtained by collecting all particles exiting the screw conveyor domain via the outlet, from onset of steady state up to the end of the simulation run. This removes the initial transient from the analysis and enables the discharge temperature distributions and averages for the various cases to be presented more accurately. The discharge temperature distributions, which are presented as normalized

density functions (see Fig. 5.9), are non-Gaussian and have two peaks. For this reason, analysis of the discharge temperature distribution using mean values and standard deviations formulae meant for Gaussian distribution is not very meaningful. Closer inspection of Fig. 5.8 gives the impression that the left and right peaks somehow represent CC particles and HS particles respectively (see Fig. 5.10). Applying this hypothesis to all cases, and comparing earlier discussions with Fig. 5.8 lead to the conclusion that this interpretation is consistent for all cases studied. For instance, the ratio of surface particles to core particles decreases with increasing M_G (see Fig. 5.9a), which is consistent with our earlier observations. Even the only case giving a Gaussian discharge temperature distribution (Case D3: $P/D = 0.25$) is also consistent with the above hypothesis; i.e., a single peak (see Fig. 5.9d) represent the absence of CC and HS particles; In other words, configuration D3 gives the most uniformly heated bed compared to other configurations studied.

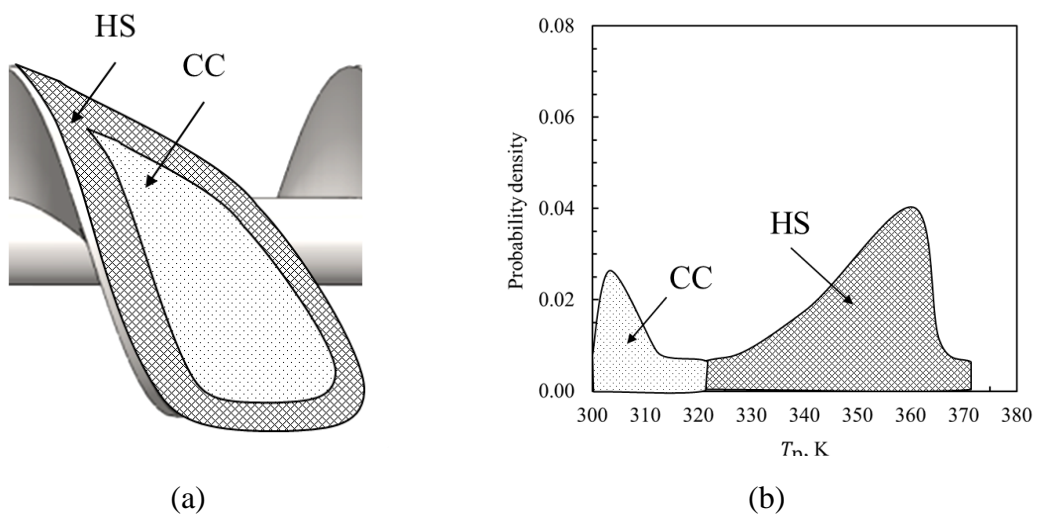


Fig. 5.10. Discharge temperature distribution mapping to cool core (CC) particles and heated surface (HS) particles.

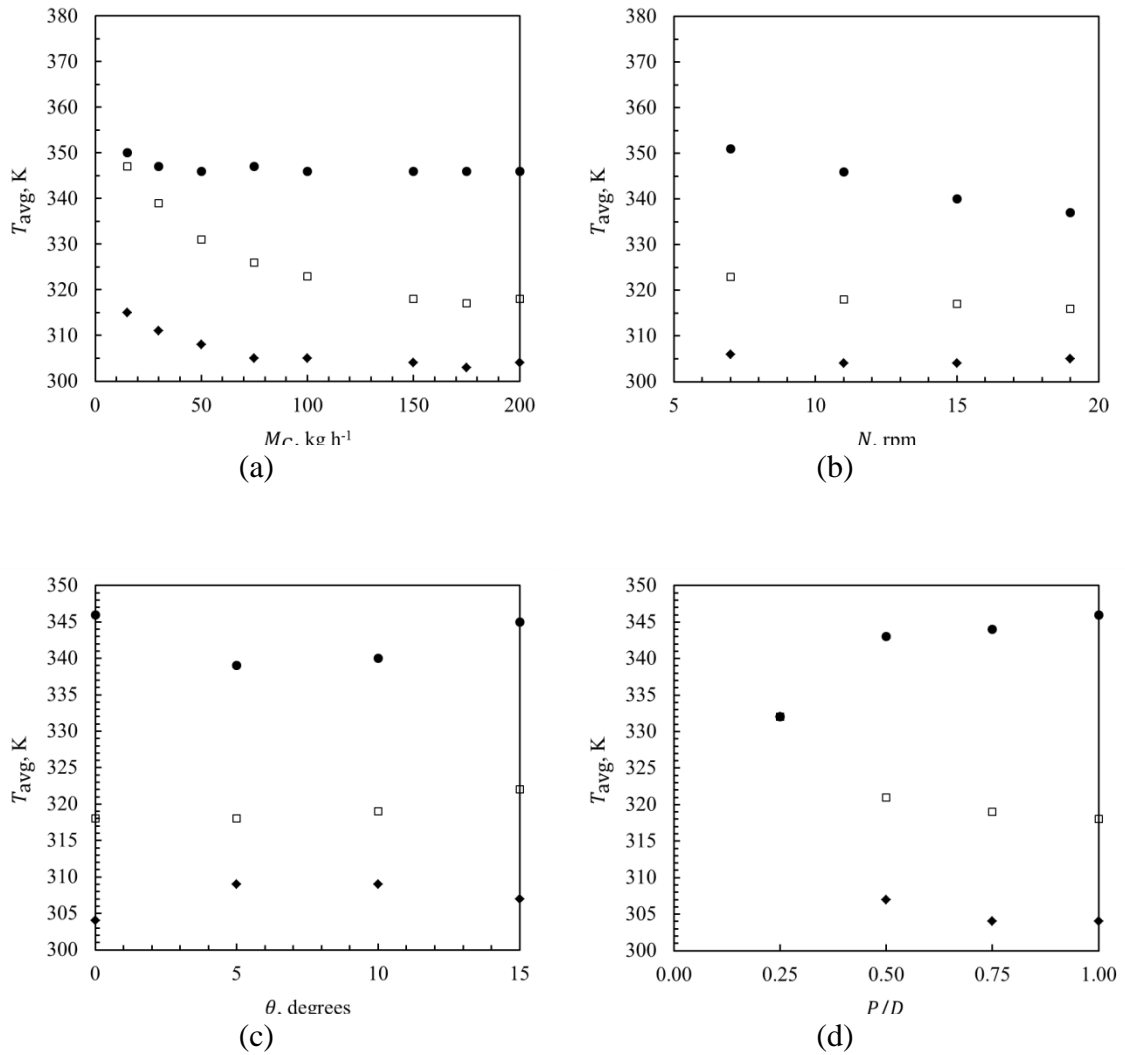


Fig. 5.11. Temperature averages for various cases: (a) solid flow rates ($N = 11$ rpm, $P/D = 1.0$), (b) screw speed ($M_G = 150$ kg h^{-1} , $P/D = 1.0$), (c) angle of inclination ($M_G = 150$ kg h^{-1} , $N = 11$ rpm), and (d) pitch-to-diameter ratio ($M_G = 150$ kg h^{-1} , $N = 11$ rpm). Legend: \square discharge average ($T_{b,f}$), \bullet heated surface average (T_{HS}), \blacklozenge cool core average (T_{CC}).

Average discharge temperature is calculated by collating the temperature of all particles exiting the screw conveyor domain after steady-state is achieved up to the end of the simulation run. This ensures that initial fluctuation in temperature is not included in the computation. In addition, the DEM program is written such that there is no further heat transfer once the particles exit the screw conveyor domain. The average discharge

temperature $T_{\text{bed},f}$ and the effective heat transfer surface area A_{ht} of the heater is used to calculate the overall heat transfer coefficient of the heating device. Data from Fig. 5.9 is processed into three average parameters namely $T_{\text{bed},f}$, T_{CC} , and T_{HS} for average discharge temperature, average cool core temperature, and average heated surface particles temperature respectively. Distinguishing CC from HS averages facilitates better understanding of the mixing and heating characteristics of the screw heater under various conditions. Fig. 5.11 shows the effect of M_G , N , θ , and P/D on the discharge averages $T_{\text{bed},f}$, T_{CC} , and T_{HS} . It is observed that $T_{\text{bed},f}$ decreases with increasing M_G , N , and P/D , but increases with θ . T_{CC} , and T_{HS} behave quite differently.

5.5 Calculation of overall heat transfer coefficient

5.5.1 Effective heat transfer area

The effective heat transfer area of the screw conveyor heater A_{ht} (m^2) is calculated by multiplying the projected area of one particle by the number of particles n_p in contact with the heated surfaces, and further multiplying the result with a correction factor of 1.27, i.e.,

$$A_{\text{ht}} = 1.27 \times \frac{1}{4} \pi d^2 n_p, \quad (5.1)$$

where d is the diameter of the particle. Experimentally, the surface coverage for irregular geometry such as the screw conveyor cannot be determined exactly and is approximated using a combination of degree of fullness and total available surface area (Waje *et al.*, 2006). The total effective heat transfer surface area (trough and screw

combined) of the 0.32 m screw conveyor heat exchanger is shown in Fig. 5.12. It is observed that A_{ht} increases with M_G and θ but decreases with N . The reason for this is quite obvious and relates to the degree of fullness under different operating conditions.

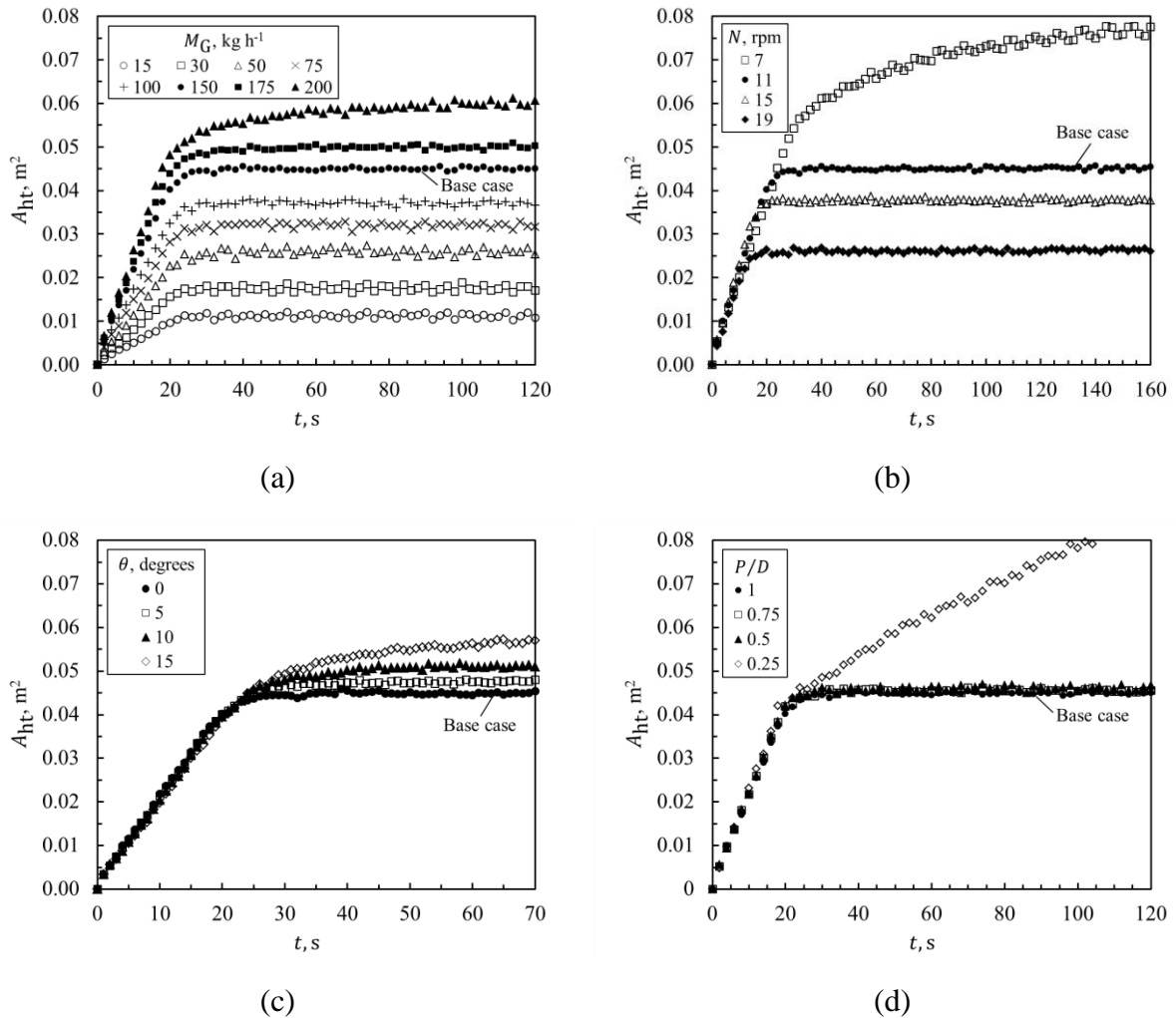


Fig. 5.12. Total effective heat transfer area for various cases: (a) solid flow rates ($N = 11$ rpm, $P/D = 1.0$), (b) screw speed ($M_G = 150\ kg\ h^{-1}$, $P/D = 1.0$), (c) angle of inclination ($M_G = 150\ kg\ h^{-1}$, $N = 11$ rpm), and (d) pitch-to-diameter ratio ($M_G = 150\ kg\ h^{-1}$, $N = 11$ rpm).

Interestingly, Fig. 5.12d shows that P/D has very little effect on A_{ht} . One would expect that the increasing the number of screw turns per unit length of the screw will

increase A_{ht} by virtue of the greater area of immersed surfaces. This, of course is not the case. Looking at the contributing effective heat transfer areas from the screw and trough separately (see Fig. 5.13), it is observed that reducing the screw pitch indeed increased the effective heat transfer area of the screw. On the other hand, the effective trough area decreases with increasing screw turns due to the inaccessibility of the trough area that is directly below the screw edge. Because the loss and gain in A_{ht} from the trough and screw is almost of equal magnitude, the overall effect of P/D on the total A_{ht} is negligible. It is also interesting to note that while $A_{ht} \sim 0.045 \text{ m}^2$ for $P/D = 1, 0.75$, and 0.5 , A_{ht} for $P/D = 0.25$ is much larger and continues to increase with time. This is due to relatively high rate of reversed particle flow which resulted in the build-up of particles in the feed region.

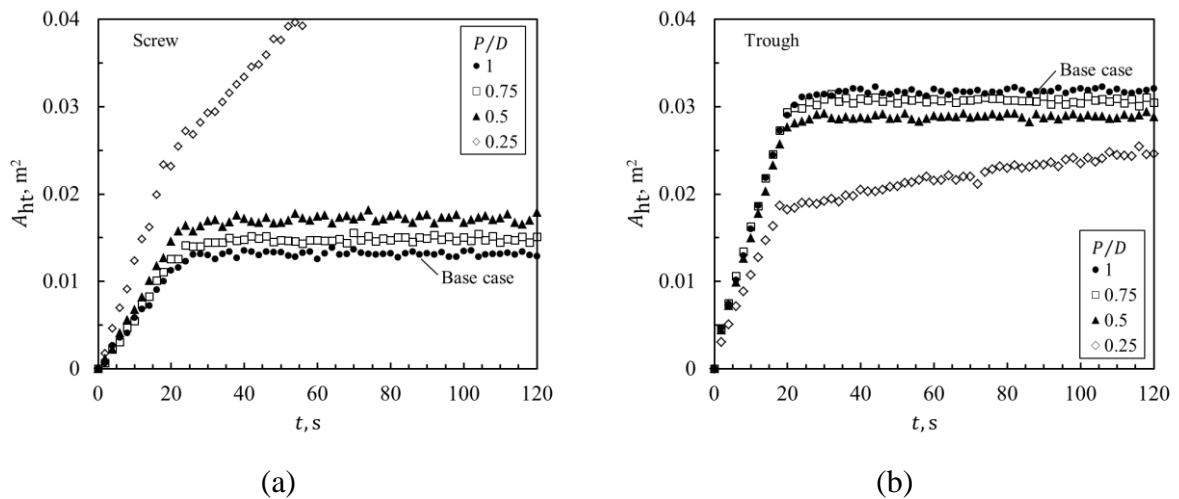


Fig. 5.13. Effective heat transfer area of screw and trough for different pitch-to-diameter ratios ($M_G = 150 \text{ kg h}^{-1}$, $N = 11 \text{ rpm}$).

5.5.2 Overall heat transfer coefficient

The overall heat transfer coefficient h is plotted against parameters M_G , N , θ , and P/D in Fig. 5.14. For the same screw speed, increasing the solid flow rate reduces h . Decrements in h is small for M_G between 50 kg h⁻¹ and 200 kg h⁻¹, but large between 15 kg h⁻¹ and 50 kg h⁻¹. h dropped by more than 20% when M_G is increased from 15 kg h⁻¹ to 50 kg h⁻¹, whereas increasing M_G from 50 kg h⁻¹ to 200 kg h⁻¹ resulted in a mere 6% drop in h .

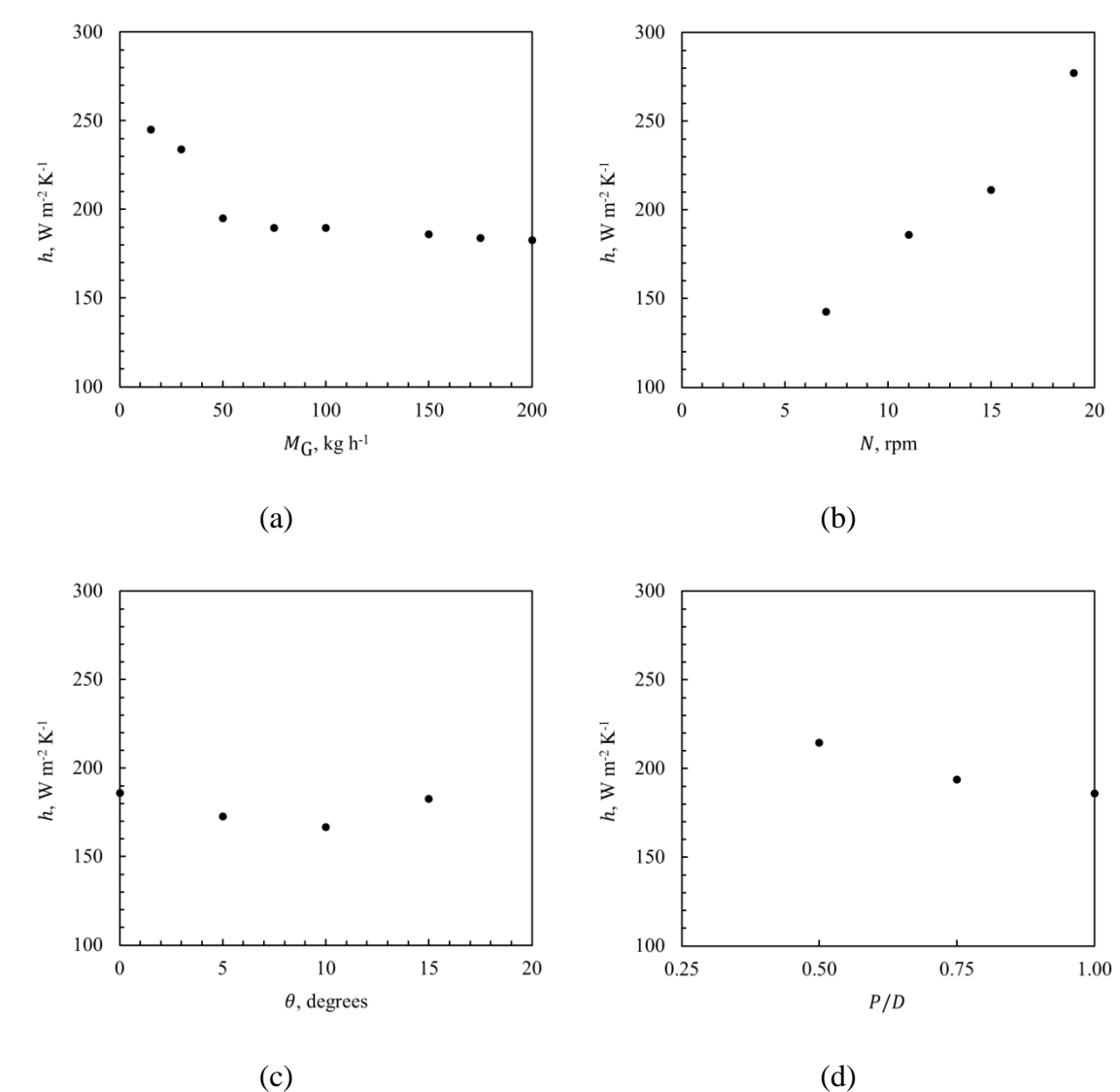


Fig. 5.14. Overall heat transfer coefficient h for various cases.

Table 5.2. Summary of heat transfer characteristics for various cases.

Case	M_G , kg h ⁻¹	A_{ht} , m ²	ΔT , K	T_{LMTD} , K	h , W m ⁻² K ⁻¹
Base	150	0.045	20.4	64.2	186
A1	15	0.011	48.6	46.5	245
A2	30	0.018	40.6	52.1	234
A3	50	0.026	32.8	57.0	195
A4	75	0.032	27.7	60.1	190
A5	100	0.037	24.7	61.8	190
A6	175	0.050	19.4	64.8	184
A7	200	0.060	20.1	64.4	183
B1	150	0.077	25.5	61.4	143
B2	150	0.038	19.5	64.8	211
B3	150	0.026	17.9	65.6	277
C1	150	0.047	20.0	64.5	173
C2	150	0.051	20.7	64.1	167
C3	150	0.057	24.3	62.1	183
D1	150	0.046	21.3	63.7	194
D2	150	0.046	23.4	62.5	214

For the same solid flow rate, the relation between h and N is linear. Results showed that h increased from 186 W m⁻² K⁻¹ to 277 W m⁻² K⁻¹ as N is increased from 11 rpm to 19 rpm, which present around 50% increase in h . The effect of θ on h appears to be parabolic for the range of angles studied. h was observed to decrease by 10% to 167 W m⁻² K⁻¹ when θ is increased to 10° from horizontal position, but increase to 183 W m⁻² K⁻¹ when the screw conveyor heater is inclined further to 15°. For a constant linear screw speed, it was observed that decreasing P/D result in big

improvements in h , i.e. h increase by more than 15% when the pitch-to-diameter ratio is halved. Summary result for the heat transfer simulation is listed in Fig. 5.14.

Chapter 6

Summary and Conclusions

A computational study of flow and heat transfer of granular media in a screw conveyor heater is carried out using discrete element method (DEM), where the granular bed is modeled as spherical particles having the same size, and interaction between those particles follow Hertz-Mindlin contact model. Penetration Model is used model heat transfer and is calibrated according to experimental data provided by Schlunder (1984).

The present study has focused on the effects of mass flow rate, screw speed, angle of inclination, and pitch-to-diameter ratio on granular flow dynamics and heat transfer, quantified by residence time, segregation and hold back, bed temperature distribution, and overall heat transfer coefficient. Thus, this study provides very useful insights to complex granular process that is expected to occur in a screw conveyor heater. However, the assumption of glass particles to approximate coal is an obvious limitation of the thesis. This is due to lack of consistent flow and heat transfer data for coal, whereas very reliable experimental data are available for glass spheres. Nevertheless, the study is not without merits and the author believes that he has contributed a very useful and relevant work when viewed from the quantitative sense and also from the angle of basic research.

The use of DEM coupled with heat transfer in the manner of this thesis is undoubtedly the first of its kind and it is hoped that future work using DEM can build upon the methodologies used in this thesis.

Proposed future work:

- Extend existing model to a full scale model;
- Model flow and heat transfer of coal particles in a screw conveyor heater;
- Develop DEM model to include species transport to simulate drying;
- Couple DEM with CFD to simulate drying vibrated bed dryer;

Bibliography

- Ai, J., Chen, J.-F., Rotter, M.J. & Ooi, J.Y., 2011. Assessment of rolling resistance models in discrete element simulations. *Powder Technology*, 206 (3), 269-282.
- Akira, N., Keiichi, K., Takeshi, W., Huminobu, O., Yoshiaki, H. & Katsuhisa, M., 1988. *Coal moisture control process*. EPO EP0370144.
- Al-Kassir, A., Ganan, J. & Tinaut, F.V., 2005. Theoretical and experimental study of a direct contact thermal screw dryer for biomass residues. *Applied Thermal Engineering*, 25 (17-18), 2816-2826.
- Amarasiri, A. & Kodikara, J., 2011. Use of material interfaces in DEM to simulate soil fracture propagation in mode I cracking. *International Journal of Geomechanics*, 11 (4), 314-322.
- Arratia, P.E., Duong, N.-H., Muzzio, F.J., Godbole, P. & Reynolds, S., 2006. A study of the mixing and segregation mechanisms in the bohle tote blender via DEM simulations. *Powder Technology*, 164 (1), 50-57.
- Azuma, K., 2001. *Screw conveyor system of drier for waste containing water*. JPO 2001165572.
- Balazs, T., Orvos, M. & Tomosy, L., 2007. Heat and mass transfer in an agitated contact-convective heated dryer. *Foods and Bioproducts Processing*, 85 (3), 291-297.
- Bauer, R., 1977. Effektive radiale wärmeleitfähigkeit gasdurchstromter schüttungen aus partikeln unterschiedlicher form und grossenverteilung. *VDI-Forschungsh*, (582).
- Benali, M. & Kudra, T., 2001. Performance characteristics of the multistage screw-in-trough dryer. *Industrial Heat Engineering*, 3 (3-4), 59-63.
- Benali, M. & Kudra, T., 2002. Thermal dewatering of diluted organic suspensions: Process mechanism and drying kinetics. *Drying Technology*, 20 (4-5), 935-951.
- Bertrand, F., Leclaire, L.A. & Levecque, G., 2005. DEM-based models for the mixing of granular materials. *Chemical Engineering Science*, 60 (8-9), 2517-2531.
- Bill, C.E., 1938. Rotary steam tube dryer. *Industrial and Engineering Chemistry*, 30 (9), 997-999.
- Bluhm-Drenhaus, T., Simsek, E., Wirtz, S. & Scherer, V., 2010. A coupled fluid dynamic-discrete element simulation of heat and mass transfer in a lime shaft kiln. *Chemical Engineering Science*, 65 (9), 2821-2834.
- Borodulya, V.A., Teplitsky, Y.S., Markevich, I.I., Hassan, A.F. & Yeryomenko, T.P., 1991. Heat transfer between a surface and a fluidized bed: Consideration of pressure and temperature effects. *International Journal of Heat and Mass Transfer*, 34 (1), 47-53.
- Brosh, T. & Levy, A., 2010. Modeling of heat transfer in pneumatic conveyor using a combined DEM-CFD numerical code. *Drying Technology*, 28 (2), 155-164.
- Bukareva, M.F., Chlenov, V.A. & Mikhailov, N.V., 1971. Investigation of heat transfer between heating surfaces and a vibrofluidized bed. *International Chemical Engineering*, 1 (1), 19-21.
- Burkhardt, G.J., 1967. Effect of pitch radial clearance, hopper exposure and head on performance of screw feeders. *Transactions of the ASAE 1967*, 10 (1), 685-690.
- Carleton, A., Miles, J. & Valentine, F., 1969. A study of factors affecting the performance of screw conveyors and feeders. *Transactions of the ASME 1969*, 91, 329-334.

- Cha, C.Y., Merriam, N.W. & Boysen, J.E., 1992. *Inclined fluidized bed system for drying fine coal*. USPTO 5087269.
- Chang, C.S. & Steele, J.L., 1997. Performance characteristics of the inlet section of a screw auger. *Applied Engineering in Agriculture*, 13 (5), 627-630.
- Chaudhuri, B., Muzzio, F.J. & Tomassone, M.S., 2006. Modeling of heat transfer in granular flow in rotating vessels. *Chemical Engineering Science*, 61 (2006), 6348-6360.
- Chaudhuri, B., Muzzio, F.J. & Tomassone, M.S., 2011. Experimentally validated numerical modeling of heat transfer in granular flow in rotating vessels. In Belmiloudi, A. ed. *Heat transfer - mathematical modeling, numerical methods and information technology*. InTech.
- Chen, J.C., 1999. Heat transfer in fluidized beds. In Yang, W.-C. ed. *Fluidization solids handling and processing*. Westwood, New Jersey: Noyes Publications, 153-208.
- Chu, K.W., Wang, B., Xu, D.L., Chen, Y.X. & Yu, A.B., 2011. CFD-DEM simulation of the gas-solid flow in a cyclone separator. *Chemical Engineering Science*, 66 (5), 834-847.
- Cleary, P.W., 2001. Modelling comminution devices using DEM. *International Journal for Numerical and Analytical Methods in Geomechanics*, 25 (1), 83-105.
- Cleary, P.W., 2004. Large scale industrial DEM modelling. *Engineering Computations*, 21 (2-4), 169-204.
- Cleary, P.W., 2007. Granular flows: Fundamentals and applications. In Aste, T., Matteo, T.D. & Tordesillas, A. eds. *Granular and complex materials*. Singapore: World Scientific Publishing, 141-168.
- Cleary, P.W. & Sawley, M.L., 2002. DEM modelling of industrial granular flows: 3d case studies and the effect of particle chae on hopper discharge. *Applied Mathematical Modelling*, 26 (2), 89-111.
- Comolli, A.G., 1979. *Drying and passivating wet coals and lignite*. USPTO 4249909.
- Costarelli, E., 1985. USPTO 4520724.
- Cundall, P.A. & Strack, O.D., 1979. A discrete numerical model for granular assemblies. *Geotechnique*, 29 (1), 47-65.
- Dai, J. & Grace, J.R., 2011. Biomass granular screw feeding: An experimental investigation. *Biomass and Bioenergy*, 35 (2), 942-955.
- Danckwerts, P.V., 1958. Continuous flow systems. *Chemical Engineering Science*, 2 (1), 1-18.
- Delaney, G.W., Cleary, P.W., Hilden, M. & Morrison, R.D., 2009. Validation of DEM predictions of granular flow and separation efficiency for horizontal laboratory scale wire mesh screen. *Seventh International Conference on CFD in the Minerals and Process Industries*. Melbourne, Australia.
- Deng, S., Podgorney, R. & Huang, H., Year. Discrete element modeling of rock deformation, fracture network development and permeability evolution under hydraulic simulationed.^eds. *Proceedings of the Thirty-sixth workshop on geothermal reservoir engineering*, Standford, California.
- Derjaguin, B.V., Muller, V.M. & Toporov, Y.P., 1975. Effect of contact deformations on the adhesion of particles. *Journal of Colloid and Interface Science*, 53 (2), 314-326.
- Dubey, A., Sarkar, A., Ierapetritou, M., Wassgren, C.R. & Muzzio, F.J., 2011. Computational approaches for studying the granular dynamics of continuous belnding processes, 1 - DEM based methods. *Macromolecular Materials and Engineering*, 296 (3-4), 290-307.

- Dunlop, D.D. & Kenyon, L.C., 2009. *Process for drying coal*. USPTO 7537622.
- Elata, D. & Berryman, J., 1996. Contact force-displacement laws and the mechanical behavior of random packs of identical spheres. *Mechanics of Materials*, 24 (3), 229-240.
- Ergun, S., 1952. Fluid flow through packed columns. *Chemical Engineering Progress*, 48, 89-94.
- Erisman, J.L., 1938. Roto-louvre dryer. *Industrial and Engineering Chemistry*, 30 (9), 996-997.
- Feng, Y.T., Han, K. & Owen, D.R.J., 2009. Discrete thermal element modelling of heat conduction in particle systems: Pipe-network model and transient analysis. *Powder Technology*, 193 (3), 248-256.
- Fernandez, J.W., Cleary, P.W. & McBride, W., 2009. Effect of screw design on hopper draw down by a horizontal screw feeder. *Seventh International Conference on CFD in the Minerals and Process Industries*. Melbourne, Australia.
- Geng, Y. & Che, D., 2011. An extended DEM-CFD model for char combustion in a bubbling fluidized bed combustor of inert sand. *Chemical Engineering Science*, 66 (2), 207-219.
- Gopalkrishna, S. & Jaluria, Y., 1992. Heat and mass transfer in a single screw extruder for non-newtonian materials. *International Journal of Heat and Mass Transfer*, 35 (1), 221-237.
- Grima, A.P. & Wypych, P.W., 2011a. Discrete element simulations of granular pile formation. *Engineering Computations*, 28 (3), 314-339.
- Grima, A.P. & Wypych, P.W., 2011b. Investigation into calibration of discrete element model parameters for scale-up and validation of particle-structure interactions under impact conditions. *Powder Technology*, 212 (1), 198-209.
- Hare, C.L., Ghadiri, M. & Dennehy, R., 2011. Prediction of attrition in agitated particle beds. *Chemical Engineering Science*, 66 (20), 4757-4770.
- Hassanpour, A., Tan, H., Bayly, A., Gopalkrishnan, P., Ng, B. & Ghadiri, M., 2011. Analysis of particle motion in a paddle mixer using discrete element method (DEM). *Powder Technology*, 206 (1-2), 189-194.
- He, K. & Dong, S., 2007. Multigrid contact detection method. *Physical Review E*, 75 (3), 036710.
- Hertz, H., 1882. On the contact of elastic solids. *J. reine und angewandte Mathematik*, 92, 156-171.
- Hobbs, A., 2009. Simulation of an aggregate dryer using coupled CFD and DEM methods. *International Journal of Computational Fluid Dynamics*, 23 (2), 199-207.
- Hu, G., Chen, J., Jian, B., Wan, H. & Liu, L., 2010. Modeling and simulation of transportation system of screw conveyors by the discrete element method. *2010 International Conference on Mechanic Automation and Control Engineering (MACE)*. Wuhan, China.
- Jangam, S.V., Karthikeyan, M. & Mujumdar, A.S., 2011. A critical assessment of industrial coal drying technologies: Role of energy, emissions, risk and sustainability. *Drying Technology*, 29 (4), 395-407.
- Jin, F., Xin, H., Zhang, C. & Sun, Q., 2011. Probability-based contact algorithm for non-spherical particles in DEM. *Powder Technology*, 212 (1), 134-144.
- Johnson, K.L., Kendall, K. & Roberts, A.D., Year. Surface energy and the contact of elastic solids. *Proceedings of the Royal Society of London A* The Royal Society, 301-313.

- Kaneko, Y., Shiojima, T. & Horio, M., 2000. Numerical analysis of particle mixing characteristics in a single helical ribbon agitator using DEM simulation. *Powder Technology*, 108 (1), 55-64.
- Karthikeyan, M., 2008. Minimization of moisture readsorption in dried coal samples. *Drying Technology*, 26 (7), 948-955.
- Katterhagen, W.R., Am Ende, M.T. & Hancock, B.C., 2009. Process modeling in the pharmaceutical industry using the discrete element method. *Journal of Pharmaceutical Sciences*, 98 (2), 442-470.
- Katterhagen, W.R., Curtis, J.S., Wassgren, C.R., Kong, A., Narayan, P.J. & Hancock, B.C., 2007. Granular segregation in discharging cylindrical hoppers: A discrete element and experimental study. *Chemical Engineering Science*, 62 (22), 6423-6439.
- Kim, H.-S., Shin, M.-S., Jang, D.-S. & Na, E.-S., 2005. A study for the thermal treatment of dehydrated sewage sludge with gas-agitated double screw type dryer. *Journal of Environmental Science and Health Part A*, 40 (1), 203-213.
- Krugger-Emden, H., Wirtz, S., Simsek, E. & Scherer, V., 2006. Modeling of granular flow and combined heat transfer in hoppers by the discrete element method (DEM). *Journal of Pressure Vessel Technology*, 128 (3), 439-444.
- Kwan, C.C., Mio, H., Chen, Y.Q., Ding, Y.L., Saito, F., Papadopoulos, D.G., Bentham, A.C. & Ghadiri, M., 2005. Analysis of the milling rate of pharmaceutical powders using the distinct element method (DEM). *Chemical Engineering Science*, 60 (5), 1441-1448.
- Kwapinska, M., Saage, G. & Tsotsas, E., 2008. Continuous versus discrete modelling of heat transfer to agitated beds. *Powder Technology*, 181 (3), 331-342.
- Ladt, M.A., 1984. *Method of drying fine coal particles*. USPTO 4444129.
- Langston, P.A., Tuzun, U. & Heyes, D.M., 1994. Continuous potential discrete particle simulations of stress and velocity fields in hoppers: Transition from fluid to granular flow. *Chemical Engineering Science*, 49 (8), 1259-1275.
- Langston, P.A., Tuzun, U. & Heyes, D.M., 1995. Discrete element simulation of granular flow in 2d and 3d hoppers: Dependence of discharge rate and wall stress on particle interactions. *Chemical Engineering Science*, 50 (6), 967-987.
- Lehmborg, J., Hehl, M. & Schugerl, K., 1977. Transverse mixing and heat transfer in horizontal rotary drum reactors. *Powder Technology*, 18 (2), 149-163.
- Lemieux, M., Leonard, G., Doucet, J., Leclaire, L.A., Viens, F., Chaouki, J. & Bertrand, F., 2008. Large-scale numerical investigation of solids mixing in a v-blender using the discrete element method. *Powder Technology*, 181 (2), 205-216.
- Li, C.-Z. ed. 2004. *Advances in the science of victorian brown coal*, Oxford, UK: Elsevier.
- Li, J. & Mason, D.J., 2002. Application of the discrete element modelling in air drying of particulate solids. *Drying Technology*, 20 (2), 255-282.
- Lucarelli, B., Year. Benefits of drying indonesian low rank coals. [^]eds. *Proceedings of the US AID Cleaner Coal Workshop*, Ha Long City, Vietnam.
- Mabrouk, S.B., Khiari, B. & Sassi, M., 2006. Modelling of heat and mass transfer in a tunnel dryer. *Applied Thermal Engineering*, 26 (17-18), 2110-2118.
- Makse, H.A., Gland, N., Johnson, D.L. & Schwartz, L., 2004. Granular packings: Nonlinear elasticity, sound propagation, and collective relaxation dynamics. *Physics Review E*, 70 (6), 061302.

- Malhotra, K. & Mujumdar, A.S., 1987. Immersed surface heat transfer in a vibrated fluidized bed. *Industrial and Engineering Chemistry Research*, 26 (10), 1983-1992.
- Malhotra, K. & Mujumdar, A.S., 1991a. Model for contact heat transfer in mechanically stirred granular beds. *International Journal of Heat and Mass Transfer*, 34 (2), 415-425.
- Malhotra, K. & Mujumdar, A.S., 1991b. Wall-to-bed contact heat transfer rates in mechanically stirred granular beds. *International Journal of Heat and Mass Transfer*, 34 (2), 427-435.
- Manickam, S.S., Shah, R., Tomei, J., Bergman, T.L. & Chaudhuri, B., 2010. Investigating mixing in a multi-dimensional rotary mixer: Experiments and simulations. *Powder Technology*, 201 (1), 83-92.
- Martin, H., 1984. Heat transfer between gas fluidized beds of solid particles and the surfaces of immersed heat exchanger elements, part ii. *Chemical Engineering and Processing: Process Intensification*, 18 (4), 199-223.
- Masson, S. & Martinez, J., 2000. Effect of particle mechanical properties on silo flow and stresses from distinct element simulations. *Powder Technology*, 109 (1-3), 164-178.
- Mcbride, W. & Cleary, P.W., 2009. An investigation and optimization of the 'olds' elevator using discrete element modeling. *Powder Technology*, 193 (3), 216-234.
- Mccabe, M.M., 1991. *System and method for removing a volatile component from a matrix*. USPTO 5216821.
- Mentz, J.W., 1995. USPTO 5531034.
- Merritt, R.D., 1987. Alaska's low-sulfur coal resources may be world's largest. *Journal of Coal Quality*, 104-108.
- Mezhericher, M., Brosh, T. & Levy, A., 2011. Modeling of particle pneumatic conveying using DEM and dpm methods. *Particulate Science and Technology*, 29 (2), 197-208.
- Mezhericher, M., Levy, A. & Borde, I., 2010. Three-dimensional modelling of pneumatic drying process. *Powder Technology*, 203 (2), 371-383.
- Mindlin, R.D. & Deresiewicz, H., 1953. Elastic spheres in contact under varying oblique forces. *Journal of Applied Mechanics*, 20 (5), 327-344.
- Mio, H., Shimosaka, A., Shirakawa, Y. & Hidaka, J., 2007. Cell optimization for fast contact detection in the discrete element method algorithm. *Advanced Powder Technology*, 18 (4), 441-453.
- Mishra, B.K., Thornton, C. & Bhimji, D., 2002. A preliminary numerical investigation of agglomeration in a rotary drum. *Minerals Engineering*, 15 (1), 27-33.
- Montellano-Gonzalez, C., Ramirez, A., Gallego, E. & Ayuga, F., 2011. Validation and experimental calibration of 3d discrete element models for the simulation of the discharge flow in silos. *Chemical Engineering Science*, 66 (21), 5116-5126.
- Moysey, P.A. & Thompson, M.R., 2005. Modelling the solids inflow and solids conveying of single-screw extruders using the discrete element method. *Powder Technology*, 153 (2), 95-107.
- Ning, Z., 1995. *Elasto-plastic impact of fine particles and fragmentation of small agglomerates*. Aston University.
- Ning, Z. & Ghadiri, M., 2006. Distinct element analysis of attrition of granular solids under shear deformation. *Chemical Engineering Science*, 61 (18), 5991-6001.
- O'callaghan, J.R., 1962. Some experiments on the intake process in a vertical screw conveyor. *Journal of Agricultural Engineering Research*, 7 (4), 282-287.

- Ohmori, T., Miyahara, M. & Okazaki, M., 1994. Heat transfer in a conductive-heating agitated dryer. *Drying Technology*, 12 (1-2), 299-328.
- Okada, K., 2004. *Resin pellet dryer*. USPTO 10/887995.
- Osman, H., Jangam, S.V., Lease, J.D. & Mujumdar, A.S., 2011. Drying of low-rank coal (lrc) - a review of recent patents and innovations. *Drying Technology*, 29 (15), 1763-1783.
- Owen, P.J. & Cleary, P.W., 2009a. Prediction of screw conveyor performance using the discrete element method (DEM). *Powder Technology*, 193 (3), 274-288.
- Owen, P.J. & Cleary, P.W., 2009b. Screw conveyor performance: Comparison of discrete element modelling with laboratory experiments. *Seventh International Conference on CFD in the Minerals and Process Industries*. Melbourne, Australia.
- Polesek-Karczewska, S., 2003. Effective thermal conductivity of packed beds of spheres in transient heat transfer. *Heat and Mass Transfer*, 39 (8), 375-380.
- Potapov, A.V. & Campbell, C.S., 1997. Computer simulation of shear-induced particle attrition. *Powder Technology*, 94 (2), 109-122.
- Potyondy, D.O. & Cundall, P.A., 2004. A bonded-particle model for rock. *International Journal of Rock Mechanics and Mining Sciences*, 41 (8), 1329-1364.
- Pournin, L. & Liebling, T.M., 2008. From spheres to spheropolyhedra: Generalized distinct element methodology and algorithm analysis. In Cook, W.J., Lovasz, L. & Vygen, J. eds. *Research trends in combinatorial optimization*. Berlin, Germany: Springer.
- Rademacher, F.J.C., 1974. Some aspects of the characteristics of vertical screw conveyors for granular material. *Powder Technology*, 9 (2-3), 71-89.
- Radl, S., Kalvoda, E., Glasser, B.J. & Khinast, J.G., 2010. Mixing characteristics of wet granular matter in a bladed mixer. *Powder Technology*, 200 (3), 171-189.
- Rajamani, R.K., Mishra, B.K., Venugopal, R. & Datta, A., 2000. Discrete element analysis of tumbling mills. *Powder Technology*, 109 (1-3), 105-112.
- Rehkgugler, G.E., 1958. *Practical and theoretical performance characteristics of auger conveyors*. Cornell University.
- Reuters & Bloomberg. 2010. India poised to take top spot for Indonesian coal exports *The Jakarta Globe*.
- Rhodes, M.J., Wang, X.S., Nguyen, M., Stewart, P. & Liffman, K., 2001. Study of mixing in gas-fluidized beds using DEM model. *Chemical Engineering Science*, 56 (8), 5101-5107.
- Ristow, G.H., 1997. Outflow rate and wall stress for two-dimensional hoppers. *Physica A: Statistical Mechanics and its Applications*, 213 (3-4), 474-481.
- Ristow, G.H. & Herrmann, H.J., 1995. Forces on the walls and stagnation zones in a hopper filled with granular material. *Physica A: Statistical Mechanics and its Applications*, 213 (4), 474-481.
- Roberts, A.W., 1999. The influence of granular vortex motion on the volumetric performance of enclosed screw conveyors. *Powder Technology*, 104 (1), 56-67.
- Rojek, J., Oñate, E., Labra, C. & Kargl, H., 2011. Discrete element modelling of rock cutting. In Oñate, E. & Owen, R. eds. *Particle -based methods*. The Netherlands: Springer, 247-267.

- Romanski, F.S., Dubey, A., Chester, A.W. & Tomassone, M.S., 2011. Dry catalyst impregnation in a double cone blender: A computational and experimental analysis. *Powder Technology*.
- Rong, D. & Horio, M., Year. DEM simulation of char combustion in a fluidized bed. [^]eds. *Proceedings of the Second International Conference on CFD in the Minerals and Process Industries*, Melbourne, Australia: CSIRO, 65-70.
- Sabarez, H.T. & Athapol, N., 1993. Performance testing of an experimental screw conveyor dryer for roasting cashew nuts. *Postharvest Biology and Technology*, 2 (3), 171-178.
- Saluja, J., 1987. *Research needs and data acquisition to apply us technology to foreign coals*.
- Santos, K.G., Murata, V.V. & Barrozo, M.a.S., 2009. Three-dimensional computational fluid dynamics modelling of spouted bed. *The Canadian Journal of Chemical Engineering*, 87 (2), 211-219.
- Schafer, J., Dippel, S. & Wolf, D.E., 1996. Force scheme in simulations of granular materials. *Journal de Physique I France*, 6 (1), 5-20.
- Schlunder, E.U., 1984. Heat transfer to packed and stirrer beds from the surface of immersed bodies. *Chemical Engineering and Processing: Process Intensification*, 18 (1), 31-53.
- Schlunder, E.U. & Mollekopf, N., 1984. Vacuum contact drying of free flowing mechanically agitated particulate material. *Chemical Engineering and Processing: Process Intensification*, 18 (2), 93-111.
- Schotte, W., 1960. Thermal conductivity in packed beds. *A.I.Ch.E Journal*, 6 (1), 63-67.
- Sebarez, H.T. & Noomhorm, A., 1993. Performance testing of an experimental screw conveyor dryer for roasting cashew nuts. *Postharvest Biology and Technology*, (2), 171-178.
- Seidel, H.P., 1965. Untersuchungen zum wärmetransport in füllkörpersäulen. *Chemie Ingenieur Technik*, 37 (11), 1125-1132.
- Shimizu, Y., 2006. Three-dimensional simulation using fixed coarse-grid thermal-fluid scheme and conduction heat transfer scheme in distinct element method. *Powder Technology*, 165 (3), 140-152.
- Shimizu, Y. & Cundall, P.A., 2001. Three-dimensional DEM simulation of bulk handling by screw conveyors. *Journal of Engineering Mechanics*, 127 (9), 864-872.
- Sinnott, M.D., Cleary, P.W. & Morrison, R.D., 2011a. Is media shape important for grinding performance in stirred mills? *Minerals Engineering*, 24 (2), 138-151.
- Sinnott, M.D., Cleary, P.W. & Morrison, R.D., 2011b. Slurry flow in a tower mill. *Minerals Engineering*, 24 (2), 152-159.
- Smolders, K. & Baeyens, J., 2001. Gas fluidized beds operating at high velocities: A critical review of occurring regimes. *Powder Technology*, 119 (2-3), 269-291.
- Solutions, D., 2011. *Edem 2.4 theory reference guide*. Edinburgh, UK: DEM Solutions.
- Song, C., Wang, P. & Makse, H.A., 2008. A phase diagram for jammed matter. *Nature*, 453, 629-632.
- Spelt, J.K., Brennen, C.E. & Sabersky, R.H., 1982. Heat transfer to flowing granular material. *International Journal of Heat and Mass Transfer*, 25 (6), 791-796.
- Stevens, G.N., 1966. Aspects of the performance of small auger grain conveyor. *Journal of Agricultural Engineering Research*, 11 (1), 11-18.

- Sturm, M., Wirtz, S., Scherer, V. & Denecke, J., 2010. Coupled DEM-CFD simulation of pneumatically conveyed granular media. *Chemical Engineering & Technology*, 33 (7), 1184-1192.
- Sullivan, W.N. & Sabersky, R.H., 1975. Heat transfer to flowing granular media. *International Journal of Heat and Mass Transfer*, 18 (1), 97-107.
- Takeuchi, S., Wang, S. & Rhodes, M., 2004. Discrete element simulation of a flat-bottomed spouted bed in the 3-d cylindrical coordinate system. *Chemical Engineering Science*, 59 (17), 3495-3504.
- Tang, Z., 2001. Three-dimensional DEM theory and its application to impact mechanics. *Science in China E*, 44 (6), 561-571.
- Toei, R., Ohmori, T., Furuta, T. & Okazaki, M., 1984. Heat transfer in an indirect-heat agitated dryer. *Chemical Engineering and Processing: Process Intensification*, 18 (3), 149-155.
- Tsai, W.-R. & Lin, C.-I., 1994. On the mixing of granular materials in a screw feeder. *Powder Technology*, 80 (2), 119-126.
- Tsotsas, E. & Schlunder, E.U., 1987. Vacuum contact drying of mechanically agitated beds: The influence of hygroscopic behaviour on the drying rate curve. *Chemical Engineering and Processing: Process Intensification*, 21 (4), 199-208.
- Tsuji, Y., Kawaguchi, T. & Tanaka, T., 1993. Discrete particle simulation of two-dimensional fluidized bed. *Powder Technology*, 77 (1), 79-87.
- Tsuji, Y., Tanaka, T. & Ishida, T., 1999. Lagrangian numerical simulation of plug flow of cohesionless particles in a horizontal pipe. *Powder Technology*, 71 (3), 239-250.
- Vreedenberg, H.A., 1958. Heat transfer between fluidized bed and a horizontal tube. *Chemical Engineering Science*, 9 (1), 52-60.
- Waje, S.S., Patel, A.K., Thorat, B.N. & Mujumdar, A.S., 2007a. Study of residence time distribution in a pilot-scale screw conveyor dryer. *Drying Technology*, 25 (1), 249-259.
- Waje, S.S., Thorat, B.N. & Mujumdar, A.S., 2006. An experimental study of the thermal performance of a screw conveyor dryer. *Drying Technology*, 24 (3), 293-301.
- Waje, S.S., Thorat, B.N. & Mujumdar, A.S., 2007b. Hydrodynamic characteristics of a pilot-scale screw conveyor dryer. *Drying Technology*, 25 (4), 609-616.
- Walizer, L.E. & Peters, J.F., 2011. A bounding box search algorithm for DEM simulation. *Computer Physics Communications*, 182 (2), 281-288.
- Walton, O.R., 1993. Numerical simulations of inelastic frictional particle-particle interaction. In Roco, M.C. ed. *Particulate two-phase flows*. Oxford, UK: Butterworth-Heinemann, 884-911.
- Whitaker, S., 1975. Forced convection heat transfer correlations for flow in pipes, past flat plates, single cylinders, single spheres, and for flow in packed beds and tube bundles. *American Institute of Chemical Engineers Journal*, 18 (2), 361-371.
- Williams, J.R. & Connor, R.O., 1999. Discrete element simulation and the contact problem. *Archives of Computational Methods in Engineering*, 6 (4), 279-304.
- Willson, W.G., Walsh, D. & Irwin, W.B., 1997. Overview of low-rank coal (lrc) drying. *Coal Preparation*, 18 (1-2), 1-15.
- Wu, C. & Tian, D., Year. CFD-DEM simulation of syngas-to-methane process in a fluidized-bed reactor. In: Kim, D., Kang, Y., Lee, J.K. & Seo, Y.C., ed. *Proceedings of the The*

13th International Conference on Fluidization - New Paradigm in Fluidization Engineering, Gyeong-ju, Korea: Bepress.

- Wunschmann, J. & Schlunder, E.U., Year. Heat transfer from heated plates to stagnant and agitated beds of spherical shaped granules under normal pressure and vacuumed. *Proceedings of the Proceedings of the 5th International Heat Transfer Conference*, Tokyo, Japan, 49-53.
- Xiang, J., Munjiza, A., Latham, J.-P. & Guises, R., 2009. On the validation of DEM and FEM/DEM models in 2d and 3d. *Engineering Computations*, 26 (6), 673-687.
- Xu, B.H. & Yu, A.B., 1997. Numerical simulation of the gas-solid flow in a fluidized bed by combining discrete particle method with computational fluid dynamics. *Chemical Engineering Sciences*, 52 (16), 2785-2809.
- Yamato, Y., Year. A novel rotary dryer with through air combination. In: Strumillo, C., Pakowski, Z. & Mujumdar, A.S., ed. *Proceedings of the Tenth International Drying Symposium*, Lodz, Poland, 624-630.
- Yang, J., Malendoma, C. & Roy, C., 2000. Determination of the overall heat transfer coefficient in a vacuum pyrolysis moving and stirred bed reactor. *Chemical Engineering Research and Design*, 78 (4), 633-642.
- Yu, Y. & Arnold, P.C., 1997. Theoretical modelling of torque requirements for single screw feeders. *Powder Technology*, 93 (1), 151-162.
- Zareiforoush, H., Komarizadeh, M.H. & Alizadeh, M.R., 2010a. Performance evaluation of a 15.5. Cm screw conveyor during handling process of rough rice (*oriza sativa* l.) grains. *Nature and Science*, 8 (6), 66-74.
- Zareiforoush, H., Komarizadeh, M.H., Alizadeh, M.R. & Masoomi, M., 2010b. Screw conveyors power and throughput analysis during horizontal handling of paddy grains. *Journal of Agricultural Science*, 2 (2), 147-157.
- Zehner, P., 1973. Experimentelle und theoretische bestimmung der effektiven wärmeleitfähigkeit durchstromter kugelschüttungen bei massingen und hohen temperaturen. *VDI-Forschungsh*, (558).
- Zeigler, E.N. & Agarwal, S., 1969. On the optimum heat transfer coefficient at an exchange surface in a gas fluidized bed. *Chemical Engineering Science*, 24 (8), 1235-1240.
- Zhang, D. & Whiten, W.J., 1996. The calculation of contact forces between particles using spring and damping models. *Powder Technology*, 88 (1), 59-64.
- Zhao, X.L., Li, S.Q., Liu, G.Q., Yao, Q. & Marshall, J.S., 2008. DEM simulation of the particle dynamics in two-dimensional spouted beds. *Powder Technology*, 184 (2), 205-213.
- Zhou, H., Flamant, G. & Gauthier, D., 2004. DEM-LES simulation of coal combustion in a bubbling fluidized bed part ii: Coal combustion at the particle level. *Chemical Engineering Science*, 59 (20), 4205-4215.
- Zhou, Y.C., Wright, B.D., Yang, R.Y., Xu, B.H. & Yu, A.B., 1999. Rolling friction in the dynamic simulation of sandpile formation. *Physica A: Statistical Mechanics and its Applications*, 269 (2-4), 536-553.
- Zhu, H.P. & Yu, A.B., 2004. Steady-state granular flow in a three-dimensional hoppper with flat bottom: Microscopic analysis. *Journal of Physics D*, 37 (10), 1497-1508.

Zhu, X., Ye, S. & Pan, X., 2008. The local heat transfer mathematical model between vibrated fluidized beds and horizontal tubes. *Experimental Thermal and Fluid Science*, 32 (6), 1279-1286.

Appendix A

```

/*****
/* Heat Conduction Model      */
*****/

// For particle-particle contact elem2IsSurf = 1. For particle-geometry
contact elem2IsSurf = 0

if (elem2IsSurf !=0) {

// Obtain property values listed in preference file
double htcoeff;
double heatCap_P1;
double heatCap_P2;

m_conductionProperties.getConductionProperties(elem1Type, htcoeff,
heatCap_P1);

m_conductionProperties.getConductionProperties(elem2Type, htcoeff,
heatCap_P2);

// Particle-particle contact area
double nEquivRadius = elem1PhysicalCurvature *
elem2PhysicalCurvature/(elem1PhysicalCurvature + elem2PhysicalCurvature);

double area_pp = 2 * 3.142 * nEquivRadius * nEquivRadius;

// Get current temps
const double* elem1Temp = elem1PropData-> getValue(P_TEMPERATURE.c_str());

const double* elem2Temp = elem2PropData-> getValue(P_TEMPERATURE.c_str());

// Set changes. Have to make sure whether this is sink or source
double deltaT = *elem2Temp - *elem1Temp;
double HeatFlux1 = htcoeff * deltaT;
double HeatFlux2 = htcoeff * deltaT;

// Calculate the temperature change
double tempChange1= (HeatFlux1 * area_pp * timestep)/
(elem1Mass*heatCap_P1);
double tempChange2= (HeatFlux2 * area_pp * timestep)/
(elem2Mass*heatCap_P2);

// Set changes to the temperature
double* tempDelta1 = elem1PropData-> getDelta(P_TEMPERATURE.c_str());

double* tempDelta2 = elem2PropData-> getDelta(P_TEMPERATURE.c_str());

*tempDelta1 += tempChange1;
*tempDelta2 -= tempChange2;

}
// conduction between surface and particle goes here
else {
```

```

double htcoeff_P;
double htcoeff_G;
double heatCap_P;
double heatCap_G;

m_conductionProperties.getConductionProperties(elem1Type, htcoeff_P,
heatCap_P);

m_conductionProperties.getConductionProperties(elem2Type, htcoeff_G,
heatCap_G);

// Particle geometry contact area
double area_pg = 2 * 3.142 * elem1PhysicalCurvature *
elem1PhysicalCurvature;

// Set geometry section temperature to a constant value of 100 deg C or 373
K
const double* elem2Temp = elem2PropData-> getValue(G_TEMPERATURE.c_str());

// Get current temp of particle
const double* elem1Temp = elem1PropData-> getValue(P_TEMPERATURE.c_str());

// Set changes. Have to make sure whether this is sink or source
double deltaT = *elem2Temp - *elem1Temp;
double HeatFlux1 = htcoeff_G * deltaT;

// Calculate the temperature change. Geometry is isothermal.
double tempChange1= (HeatFlux1 * area_pg * timestep)/ (elem1Mass*heatCap_P);

// Set changes to the temperature
double* tempDelta1 = elem1PropData-> getDelta(P_TEMPERATURE.c_str());

*tempDelta1 += tempChange1;
}

return eSuccess;

}

```

Appendix B

```
/* *****  
/* Residence Time custom property */  
/* *****  
  
#include "CResidenceTime.h"  
  
using namespace std;  
using namespace NApi;  
using namespace NApiCore;  
using namespace NApiPbf;  
  
const string CResidenceTime::RESIDENCE_TIME_PROPERTY = "Residence Time";  
  
CResidenceTime::CResidenceTime()  
{  
    ;  
}  
  
CResidenceTime::~~CResidenceTime()  
{  
    ;  
}  
  
bool CResidenceTime::isThreadSafe()  
{  
    // thread safe  
    return true;  
}  
  
bool CResidenceTime::usesCustomProperties()  
{  
    // Uses custom properties  
    return true;  
}  
  
ECalculateResult CResidenceTime::externalForce(double time,  
                                                Double timestep,  
                                                Int id,  
                                                const char type[],  
                                                double mass,  
                                                double volume,  
                                                double posX,  
                                                double posY,  
                                                double posZ,  
                                                double velX,  
                                                double velY,  
                                                double velZ,  
                                                double angVelX,  
                                                double angVelY,  
                                                double angVelZ,  
                                                double charge,  
                                                const double orientation[9],  
NApiCore::ICustomPropertyDataApi_1_0* particlePropData,  
NApiCore::ICustomPropertyDataApi_1_0* simulationPropData,  
                                                double& calculatedForceX,
```

```

double& calculatedForceY,
double& calculatedForceZ,
double& calculatedTorqueX,
double& calculatedTorqueY,
double& calculatedTorqueZ)
{
// Cache pointers to the custom properties we wish to use
double* residenceTimeDelta = particlePropData->
getDelta(RESIDENCE_TIME_PROPERTY.c_str());

// Update the residence time for this particle by adding the time step to
the current value. STOP UPDATING when particle exits screw

if (posZ < 0.32)
*residenceTimeDelta += timestep;
else
*residenceTimeDelta += 0.00;

return eSuccess;
}

unsigned int CResidenceTime::getNumberOfRequiredProperties(
const NApi::EPluginPropertyCategory category)
{
// This plug-in registers 1 custom particle property
if (eParticle == category){
return 1;
}

else {
return 0;
}
}

bool CResidenceTime::getDetailsForProperty(
unsigned int propertyIndex,
NApi::EPluginPropertyCategory category,
Char name[NApi::CUSTOM_PROP_MAX_NAME_LENGTH],
NApi::EPluginPropertyDataTypes& dataType,
unsigned int& numberOfElements,
NApi::EPluginPropertyUnitTypes& unitType)
{
if (eParticle == category && 0 == propertyIndex)
{
strcpy(name, RESIDENCE_TIME_PROPERTY.c_str());
dataType eDouble;
numberOfElements = 1;
unitType = eTime;
return true;
}

else {
return false;
}
}

```